



United States Department of Commerce  
Technology Administration  
National Institute of Standards and Technology

**NISTIR 3997**

## **TRANSFER FUNCTIONS FOR CHARACTERIZING MULTIMODE OPTICAL FIBER COMPONENTS**

---

---

Shao Yang



# **TRANSFER FUNCTIONS FOR CHARACTERIZING MULTIMODE OPTICAL FIBER COMPONENTS**

---

---

**Shao Yang\***

Electromagnetic Technology Division  
Electronics and Electrical Engineering Laboratory  
National Institute of Standards and Technology  
Boulder, Colorado 80303-3328

\*Prepared at the University of Colorado under contract  
with the Optical Electronic Metrology Group

January 1993



---

**U.S. DEPARTMENT OF COMMERCE**, Barbara Hackman Franklin, Secretary  
**TECHNOLOGY ADMINISTRATION**, Robert M. White, Under Secretary for Technology  
**NATIONAL INSTITUTE OF STANDARDS AND TECHNOLOGY**, John W. Lyons, Director

## ABSTRACT

A mode transfer function approach is proposed to characterize optical fiber devices. The transfer function is used to analyze the accuracy of the mode transfer matrix, which is currently being used to characterize optical fiber devices. The analysis shows that the mode transfer matrix depends on launch condition. Based on the study of the physical process of two basic mode coupling mechanisms, that is, the scattering coupling and the overlap coupling. two basic transfer functions are derived. Mode transfer functions for fibers/cables, connectors/splices, and power splitters are formed using these two basic transfer functions. Results of a round-robin test and a concatenation experiment show that the transfer function is better than the transfer matrix in that it is independent of launch conditions, and thus can improve both the repeatability of measurements made by different laboratories and the prediction of concatenated results. The transfer function can also be used to analyze the structure of a device.

keywords: fiber optics; mode coupling; multimode fibers; optical fiber devices; transfer function; transfer matrix

## CONTENTS

### CHAPTER

1	INTRODUCTION . . . . .	1
2	THEORETICAL BACKGROUND . . . . .	5
2.1	Introduction . . . . .	5
2.2	Modes in an Optical Fiber . . . . .	6
2.3	Mode Parameter . . . . .	14
2.4	Mode Continuum . . . . .	17
2.5	Phase Space . . . . .	22
3	MODE TRANSFER MATRIX (MTM) AND MODE TRANSFER FUNCTION (MTF) . . . . .	28
3.1	Introduction . . . . .	28
3.2	MTM Technique . . . . .	28
3.3	Definition of MTF . . . . .	31
3.4	MTM as a Truncation of MTF . . . . .	32
3.5	Dependence on Launch Conditions of the Measured Matrix . .	35
3.6	Experimental Setup . . . . .	41
3.7	Round-Robin Test and Experimental Results . . . . .	51
4	COUPLING MECHANISMS AND TRANSFER FUNCTIONS . . .	63
4.1	Introduction . . . . .	63
4.2	Transfer Function for Scattering Coupling . . . . .	65
4.3	Transfer Function for Overlap Coupling . . . . .	70
5	FIBER-OPTIC DEVICES AND THEIR TRANSFER FUNCTIONS	78

5.1	Introduction . . . . .	78
5.2	Fibers and Cables . . . . .	80
5.2.1	Transfer function . . . . .	80
5.2.2	Experimental results . . . . .	82
5.3	Connectors and Splices . . . . .	88
5.3.1	Experimental results of connectors . . . . .	89
5.3.2	Experimental results of splices and their concatenation	96
5.4	Power Splitters . . . . .	104
5.4.1	A model of 3-port fused biconical taper power splitters	107
5.4.2	Experimental results . . . . .	111
5.5	Conclusions . . . . .	121
	BIBLIOGRAPHY . . . . .	126

## CHAPTER 1

### INTRODUCTION

The invention of the laser in 1960 created great interest in communication at optical frequencies, and the search for a suitable transmission medium was promptly launched. Dielectric waveguides including optical fibers were studied theoretically but were not useful because of their high loss – of the order of 100 dB/km. In 1966, however, Kao and Hockman [1] pointed out that the high loss was a result of impurities in the fiber material and that the losses could be reduced to less than 20 dB/km, a point where optical waveguides would be a viable transmission medium. They also asserted that it would be further reduced below several decibels per kilometer if the purity of the material was further improved, making scattering loss the limiting factor. This was realized in 1970 when Kapron, Keck, and Maurer [2] fabricated a silica fiber that had a 20 dB/km attenuation. This success triggered explosive research in the following years toward the development of practical optical fibers. In 1974, the fiber loss was reduced to less than 2 dB/km [3]. Since scattering loss is lower at higher wavelengths, optical fibers for longer wavelengths were also developed and the loss has already reached to 0.16 dB/km at a 1550 nm wavelength, which is close to its theoretical value of 0.14 dB/km. Some of the initial field trials of optical fiber telephone systems were carried out in 1977 in Los Angeles [4] and in Chicago [5].

The first generation of optical fiber links used multimode fibers. Due

to the elimination of modal dispersion, single-mode fibers have a much larger bandwidth than multimode fibers, and since 1984, single-mode fibers have been used exclusively for long-haul telephone trunks. However, multimode fibers continued to be used in short-distance communications systems such as the local area networks (LANs) [6] and premise wiring. Applications of optical fibers in these areas is increasing and the multimode fiber market is still growing.

Optical fiber characterization and measurement developed along with the development of optical fibers and their applications. A single loss value was originally used for characterizing a multimode fiber. Because different modes have different loss [7, 8], the measured loss for a multimode fiber is not unique. It depends on how much power is launched into different modes. After propagating a certain distance in the fiber, however, the modal power will reach the steady-state or equilibrium distribution and the loss per unit length of the fiber will then remain constant [9]. This steady-state loss represents the loss of a multimode fiber for long-distance application and was defined as the loss value for a multimode fiber. Techniques for the steady-state modal power distribution launch were devised in order to measure the steady-state loss [10, 11, 12]. Good results in the prediction of concatenation for long lengths of fiber were obtained using the steady-state loss [13, 14]. An interlaboratory comparison of attenuation measurement using two launch techniques, the limited phase space launch and the mode filter launch [15], were carried out by the National Bureau of Standards (now the National Institute of Standards and Technology, NIST) in cooperation with the Electronic Industries Association (EIA) in 1981 [16].

Multimode optical fibers are not used in long-haul communications systems any more but are being used more and more in short-haul applications where the modal power distribution will never reach the steady state. In addition, components other than the fiber such as connectors and power splitters are intensively used and can alter modal power distribution. Consequently, the steady-state loss for multimode fiber characterization has lost its usefulness. A new method, the mode transfer matrix (MTM) method [17], has been adopted by the industries to characterize multimode optical fibers and other fiber optic devices. Mode coupling has been included in the mode transfer matrix and good experimental results have been obtained. The Telecommunications Industry Association (TIA) is considering using MTM as the standard method for the characterization of multimode optical fibers and devices and an interlaboratory comparison round-robin test similar to that for the loss measurement mentioned above is being conducted by TIA, NIST and the guided-wave optics group of the University of Colorado.

Although MTM is an improvement over simple loss measurement, it has long been realized that MTM is still launch dependent [18, 19]. But no theoretical analysis and experimental tests have been carried out regarding this problem. One of the purposes of this technical note is to give a theoretical analysis of the dependence on input modal power distribution of MTM and to use the round-robin test results to verify the conclusions of this analysis. The second purpose of this technical note is to introduce the mode transfer function (MTF) method as an alternative method for the characterization of multimode optical fibers and devices. The MTF is, in principle, independent of launch conditions. MTFs for various multimode fiber devices have been derived from

the basic mode coupling mechanisms in optical fibers and devices. The round-robin data were also treated by the MTF method and the results compared with those by the MTM method. Significant improvements over the MTM method has been obtained by the MTF method.

The technical note is organized as follows. Chapter 2 describes the basic theoretical concepts which are used in the rest of the technical note. Chapter 3 gives a theoretical analysis of the MTM by means of the MTF and presents round-robin results of the MTM, which verifies the theoretical analysis. Chapter 4 derives the transfer functions for the two basic coupling mechanisms in optical fiber devices: the scattering coupling and the overlap coupling. In Chapter 5, the two basic transfer functions are applied to different devices, and the round-robin results treated by the MTF are presented and compared to those in Chapter 3. The result of a concatenation experiment of four splices is also presented. Conclusions are given in the last section of Chapter 5.

## CHAPTER 2

### THEORETICAL BACKGROUND

#### 2.1 Introduction

In this chapter, we will discuss the basic theory of wave propagation in optical fibers. This is the theoretical basis for the approach presented in this technical note. The theory of wave propagation in an optical fiber has long been established and detailed discussions can be found in many books [20, 21, 22]. We will present only those results that are relevant to this technical note.

The most important concept in optical fiber theory is the “mode,” and the major part of this technical note is about power coupling between different modes. Section 2.2 is about the basic theory of modes. A mode is a wave theory concept. However, light propagation in a fiber can also be described by ray theory. Section 2.3 introduces a parameter  $R$  which represents different modes and bridges the wave theory and ray theory. This mode parameter is used throughout this technical note. Mode is originally a discrete concept. However, in practical cases, modes in a fiber could form a continuum, which makes it possible to use a function to describe the power coupling between modes. Section 2.4 discusses the mode continuum problem. Due to the introduction of mode parameter  $R$ , it is possible to represent modes in terms of rays. A ray that represents a mode moves along a certain trajectory which can be described by its radial position and its propagation direction. These two parameters form the coordinates of the modes in phase space. The phase space concept is

introduced in Section 2.5.

## 2.2 Modes in an Optical Fiber

An optical fiber is a dielectric cylindrical waveguide, and a mode is a basic concept in the wave theory of optical fibers. The electromagnetic wave theory always starts from Maxwell's equations:

$$\begin{aligned}\nabla \times \mathbf{E}(\mathbf{r}, t) &= -\frac{\partial \mathbf{B}(\mathbf{r}, t)}{\partial t}, \\ \nabla \times \mathbf{H}(\mathbf{r}, t) &= \mathbf{J}(\mathbf{r}, t) + \frac{\partial \mathbf{D}(\mathbf{r}, t)}{\partial t}, \\ \nabla \cdot \mathbf{D}(\mathbf{r}, t) &= \rho(\mathbf{r}, t), \\ \nabla \cdot \mathbf{B} &= 0.\end{aligned}\tag{2.1}$$

The optical fiber is a dielectric medium, so

$$\mathbf{J}(\mathbf{r}, t) = 0.\tag{2.2}$$

We can also reasonably assume that

$$\rho(\mathbf{r}, t) = 0.\tag{2.3}$$

The constitutive relations for a nonmagnetic material are

$$\mathbf{D} = \epsilon \mathbf{E},\tag{2.4}$$

$$\mathbf{B} = \mu_0 \mathbf{H}.\tag{2.5}$$

The refractive index is  $n = c\sqrt{\epsilon\mu_0}$ . The index profile of a fiber takes the form

$$c^2 \epsilon(r) \mu_0 = n^2(r) = n_1^2 \begin{cases} 1 - 2\Delta f\left(\frac{r}{a}\right), & r < a, \\ 1 - 2\Delta, & r > a, \end{cases}\tag{2.6}$$

where  $f(r/a)$  is bounded between 0 and 1 with value 1 at the fiber cladding and 0 at the center of the core.  $c$  is the speed of light and  $\Delta$  is the maximum index difference

$$\Delta \equiv (n_1^2 - n_2^2)/2n_1^2 \simeq (n_1 - n_2)/n_1,\tag{2.7}$$

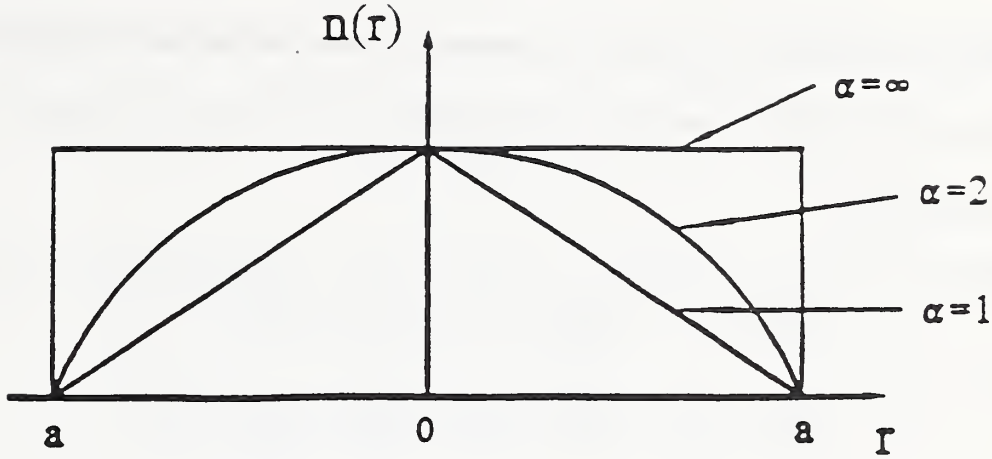


Figure 2.1: Sketches of the  $\alpha$  profile function for several  $\alpha$  values.

where  $n_1 = n(0)$  is the refractive index at the center of the core and  $n_2 = n(r \geq a)$  is the refractive index of the cladding. For a practical fiber,  $\Delta \simeq 0.01 - 0.02$ , which is small. The fiber's numerical aperture  $NA$  is determined by the index difference  $\Delta$ :

$$NA = \sqrt{n_1^2 - n_2^2} = n_1 \sqrt{2\Delta}. \quad (2.8)$$

Fibers with a small index difference are called weakly guiding fibers [23]. The weakly guiding condition also dictates that  $\nabla\epsilon/\epsilon$  is small. Practical fibers display an  $\alpha$  profile,  $f(\frac{r}{a}) = (\frac{r}{a})^\alpha$ . The value of  $\alpha$  ranges from 1 to  $\infty$ . The parabolic index profile, for which  $\alpha = 2$ , is the most commonly used in telecommunications because it has the least modal dispersion [21, 24].  $\alpha = \infty$  is the step index profile, which is the most easily fabricated.

Since practical multimode fibers are almost always nearly parabolic, we will in the following always assume that the fiber has parabolic index profile. The  $\alpha$  index profile is sketched in Figure 2.1 for several values of  $\alpha$ .

A mode is an electromagnetic disturbance which retains a certain shape when propagated forward along the fiber; that is, the transverse dependence of its field does not change. It is thus convenient to express the electric

and magnetic fields in the fiber in terms of their axial and transverse components separately. Since the fiber is a circular waveguide, cylindrical coordinates  $(r, \theta, z)$  are used:

$$\mathbf{E}(\mathbf{r}, t) = [\mathbf{E}_t(r, \theta) + \hat{e}_z E_z(r, \theta)] e^{j(\omega t - \beta z)}, \quad (2.9)$$

$$\mathbf{H}(\mathbf{r}, t) = [\mathbf{H}_t(r, \theta) + \hat{e}_z H_z(r, \theta)] e^{j(\omega t - \beta z)}, \quad (2.10)$$

where  $\mathbf{E}_t$  and  $\mathbf{H}_t$  are the transverse components in the  $r, \theta$  plane,  $E_z$  and  $H_z$  are scalar quantities of the axial components,  $\omega$  is the angular frequency of light, and  $\beta$  is the propagation constant in the axial direction. Substituting Equations (2.6) and (2.7) into Maxwell's equations and using the weakly guiding assumption, we can obtain the following vectorial wave equation for the transverse components:

$$\begin{aligned} \nabla^2 \mathbf{E}_t + [\omega^2 \epsilon(r) \mu_0 - \beta^2] \mathbf{E}_t &= 0, \\ \nabla^2 \mathbf{H}_t + [\omega^2 \epsilon(r) \mu_0 - \beta^2] \mathbf{H}_t &= 0. \end{aligned} \quad (2.11)$$

Because  $\mathbf{E}$  and  $\mathbf{H}$  are linked by Maxwell's equations, we will consider only the electric field in the following. The weakly guiding assumption dictates that the fiber modes are linearly polarized (LP) [23] and that the transverse field can be expressed in the form

$$\mathbf{E}_t(r, \theta) = a_x E_x(r, \theta) \hat{e}_x + a_y E_y(r, \theta) \hat{e}_y. \quad (2.12)$$

The wave equation for the electric field in Equation (2.11) can thus be separated into wave equations of the  $x$  and  $y$  components:

$$\nabla^2 E_a + [\omega^2 \epsilon(r) \mu_0 - \beta^2] E_a = 0 \quad (E_a = E_x, E_y). \quad (2.13)$$

These equations are called scalar wave equations.

To solve the scalar wave equation, we can try separation of variables

$$E_a = F(r)e^{-j\nu\theta}. \quad (2.14)$$

Inserting this expression into the scalar wave equation (2.13), we obtain for  $F(r)$

$$\frac{1}{r} \frac{d}{dr} \left( r \frac{dF}{dr} \right) + [\omega^2 \epsilon(r) \mu_0 - \beta^2 - \frac{\nu^2}{r^2}] F = 0. \quad (2.15)$$

With  $k^2 = \omega^2 \epsilon \mu$ , Equation (2.15) becomes

$$\frac{d^2 F}{dr^2} + \frac{1}{r} \frac{dF}{dr} + (k^2(r) - \beta^2 - \frac{\nu^2}{r^2}) F = 0, \quad (2.16)$$

where  $k^2(r)$  is given, for the parabolic index profile, by

$$k^2(r) = k_1^2 [1 - 2\Delta(\frac{r}{a})^2] = k_0^2 n_1^2 [1 - 2\Delta(\frac{r}{a})^2]. \quad (2.17)$$

Confinement of the light field in the fiber characterizes a propagating mode. Because of this property, the core-cladding boundary of the fiber has little effect on many lower-order modes. This makes it possible to use the infinite parabolic index approximation [22]. A steady and confined transverse field is the condition for the existence of a mode, which leads to the solution of Equation (2.16) and the determination of the propagation constant  $\beta$  of a mode. The solution of  $F(R)$  for a propagating mode is then

$$F_{\mu\nu}(r) = N_{\mu\nu} r^\nu e^{-\frac{\nu r^2}{2a^2}} L_\mu^\nu \left( \frac{Vr^2}{a^2} \right), \quad (2.18)$$

and the corresponding propagation constant is

$$\beta_{\mu\nu} = k_1 [1 - 2 \frac{\sqrt{2\Delta}}{k_1 a} (2\mu + \nu + 1)]^{1/2} \simeq k_1 [1 - \frac{\sqrt{2\Delta}}{k_1 a} (2\mu + \nu + 1)], \quad (2.19)$$

where  $\nu$  is an integer called the azimuthal mode number and is defined in Equation (2.14);  $\mu$  is an integer called the radial mode number and determines

the number of peaks of the radial distribution of the field;  $V$  is called the normalized frequency [21] of the fiber and is defined as

$$V = \sqrt{2\Delta}k_1a. \quad (2.20)$$

$L_\mu^\nu(x)$  is the Laguerre polynomial which is given by [25]

$$L_\mu^\nu(x) = \sum_{m=0}^{\mu} (-1)^m \frac{(\mu + \nu)!}{(\mu - m)!(\nu + m)!m!} x^m. \quad (2.21)$$

Equation (2.18) shows that the lowest-order mode has a Gaussian radial distribution:

$$F_{00} = N_{00}e^{-\frac{v_r^2}{2a^2}}. \quad (2.22)$$

$N_{\mu\nu}$  in Equation (2.18) is a normalization factor. Figure 2.2 shows the shape of some of the lowest-order  $\mu\nu$  modes.

The principal mode number  $m$  is defined as

$$m = 2\mu + \nu + 1. \quad (2.23)$$

Since all the  $\mu\nu$  modes with the same principal mode number have the same propagation constant, they are called degenerate modes [26] and form a group designated by mode number  $m$ . Because weakly guiding modes are linearly polarized, they can have two orthogonal polarization directions; that is, they can be  $x$ -polarized or  $y$ -polarized. Also, each mode can have two azimuthal orientations, except for modes with  $\nu = 0$ , which have no azimuthal variation. Thus each  $\mu\nu$  mode with  $\nu \neq 0$  is four fold degenerate, and it is two fold degenerate if  $\nu = 0$ . By counting all the possible  $\mu\nu$  combinations for a principal mode number  $m$ , we can show that there are  $2m$  degenerate modes in mode group  $m$ . It is more common to ignore the common factor of two and say that there are  $m$  degenerate modes in mode group  $m$ .

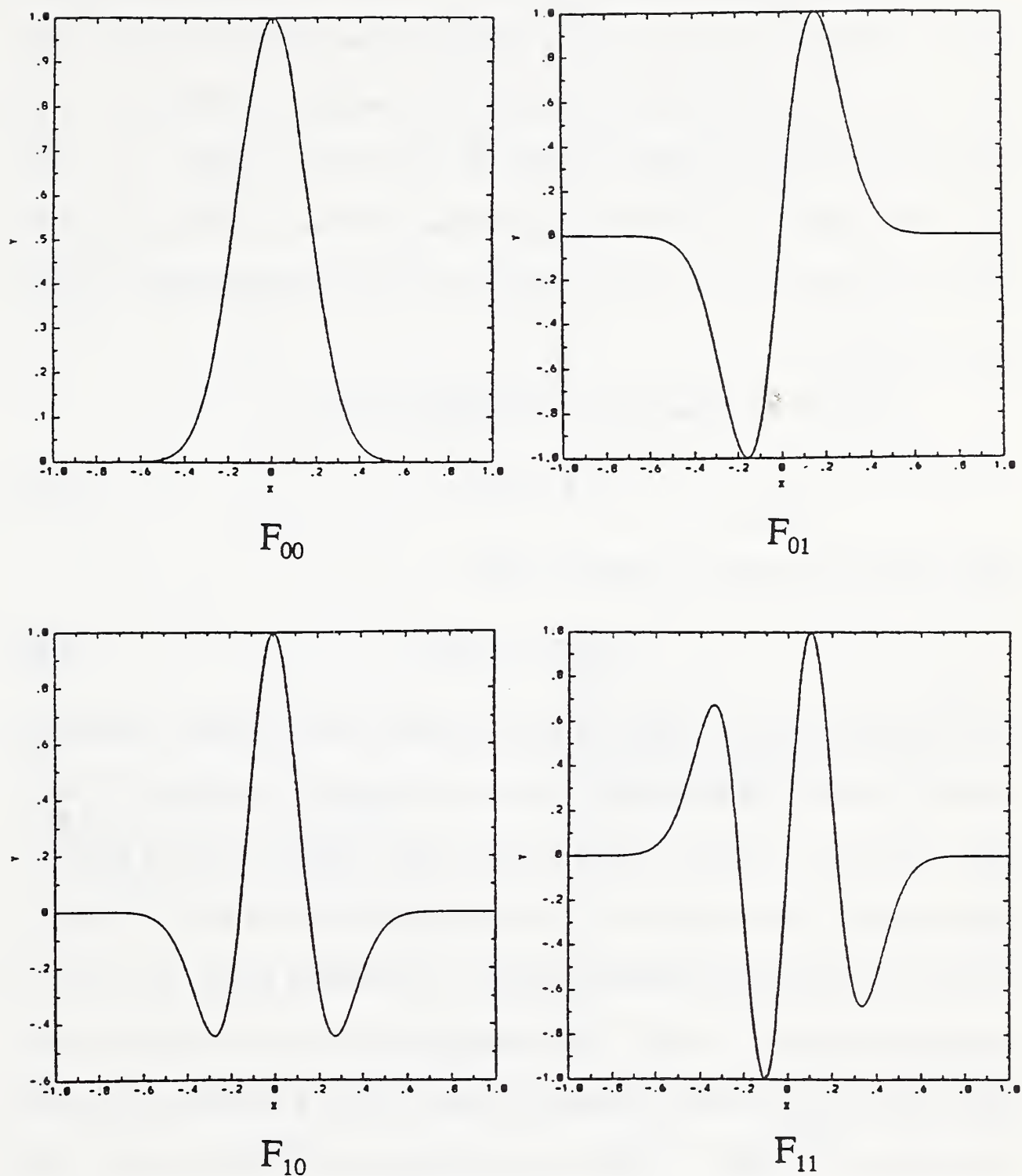


Figure 2.2: Sketches of the radial variations of the first few LP modes.

Power coupling among degenerate modes of the same mode group is usually much stronger than power coupling between different mode groups. Even if they are not equally excited, the strong coupling will distribute power evenly among these degenerate modes [27] after they propagate a short distance. The radial distribution of a mode group will then be the superposition of those of all these modes. Figure 2.3 shows the radial distribution of some of the mode groups.

The cutoff condition for a propagating mode is

$$\beta = n_2 k_0. \quad (2.24)$$

Modes whose propagation constants satisfy

$$k_0 n_1 > \beta > k_0 n_2 \quad (2.25)$$

are propagating modes. When  $\beta < k_0 n_2$ , the field is not confined. Analysis by the WKB method [28] shows that there are two kinds of modes for  $\beta < k_0 n_2$ : leaky modes and radiation modes. When  $k_0^2 n_2^2 - \frac{\nu^2 - 1/4}{a^2} < \beta^2 < k_0^2 n_2^2$ , the electromagnetic field decays for a short radial distance near the core-cladding boundary and becomes oscillatory again in the cladding region; thus some of its energy propagates outward. These kinds of modes are called leaky modes. They behave like very lossy propagation modes. When  $\beta$  becomes even smaller and satisfies  $\beta^2 < k_0^2 n_2^2 - \frac{\nu^2 - 1/4}{a^2}$ , the modes become radiation modes, which have oscillatory field distribution in both the core and cladding regions and whose transmission loss is much higher than the leaky modes.

The condition for propagation modes of Equation (2.25) can also be expressed in terms of the principal mode number  $m$  as

$$0 < m \leq \frac{V}{2}. \quad (2.26)$$

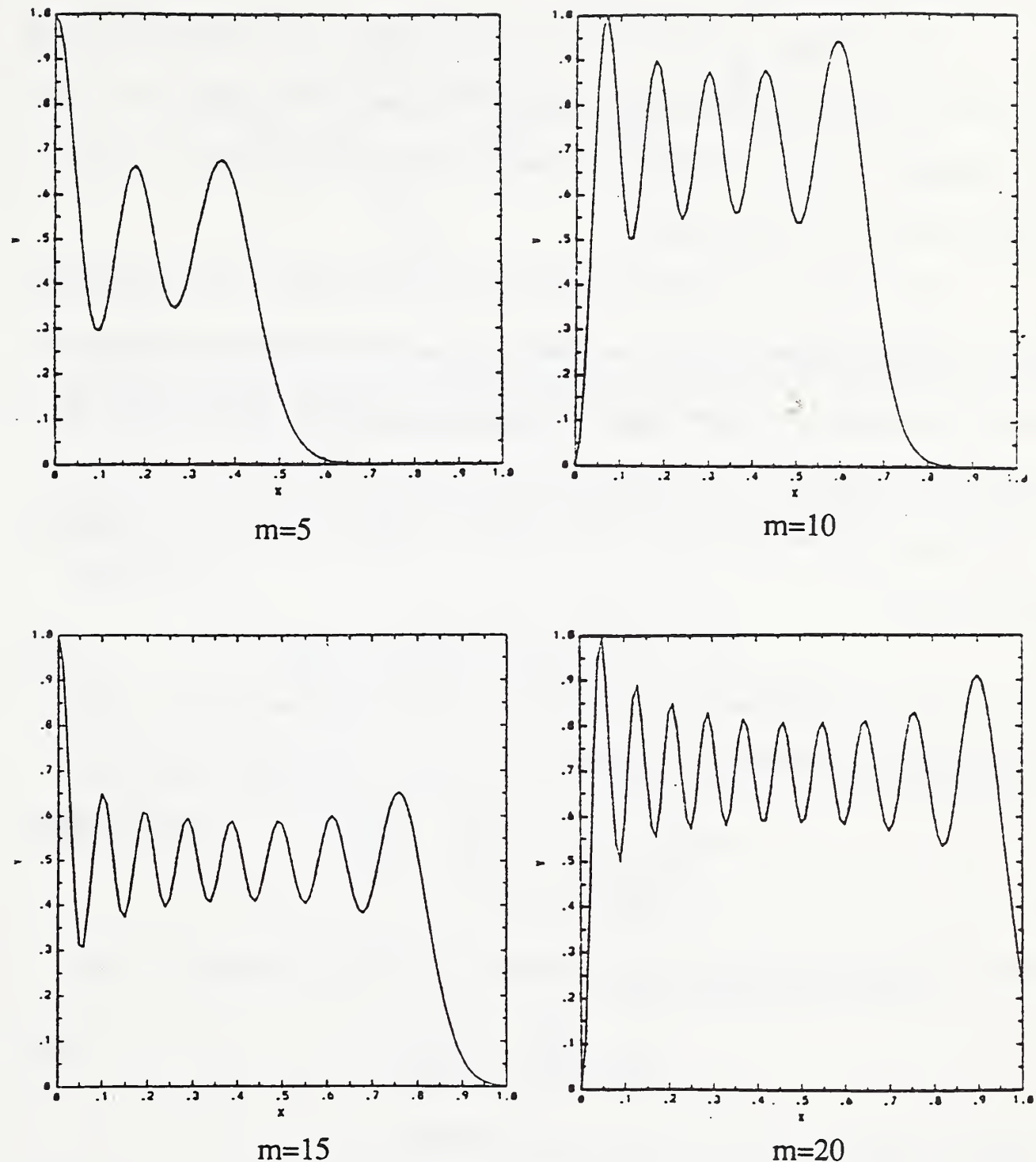


Figure 2.3: Radial distributions of mode groups  $m=5, 10, 15$ , and  $20$ .

### 2.3 Mode Parameter

A very useful parameter representing degenerate modes will be used frequently throughout this technical note. This parameter is designated as  $R$ . It is defined in terms of both wave theory and ray theory [29]. It is thus a bridge between the two theories.

Consider the geometrical optics of an optical fiber. The coordinates  $\mathbf{r}$  of a ray path represent the evolution in space of the normal to the phase front of a local plane wave travelling through a medium whose index varies slowly (compared to a wavelength). Figure 2.4 shows a sketch of a ray path. The distance measured along the ray path is  $s$  and is defined, in cylindrical coordinates, as

$$s = \int_0^s ds = \int_0^s \sqrt{(dr)^2 + (rd\phi)^2 + (dz)^2}. \quad (2.27)$$

The unit vector  $\hat{s}$  along the ray path is

$$\hat{s} = \frac{d\mathbf{r}}{ds} = \frac{dr}{ds}\hat{e}_r + r\frac{d\phi}{ds}\hat{e}_\phi + \frac{dz}{ds}\hat{e}_z. \quad (2.28)$$

The ray equation is [30]

$$\frac{\partial}{\partial s}[n(\mathbf{r})\frac{d\mathbf{r}}{ds}] = \nabla n(\mathbf{r}). \quad (2.29)$$

It can be expressed in the cylindrical coordinates as

$$\frac{\partial}{\partial s}\{n(r)[(\frac{dr}{ds})\hat{e}_r + r\frac{d\phi}{ds}\hat{e}_\phi + \frac{dz}{ds}\hat{e}_z]\} = \frac{dn(r)}{dr}\hat{e}_r, \quad (2.30)$$

where the relation that  $\hat{s} = d\mathbf{r}/ds$  has been used. Since fibers are weakly guiding, the modes are plane wave-like. The direction of the ray at any position in the fiber is the effective normalized  $k$  vector of a local plane wave. Thus

$$\hat{s} = \frac{\mathbf{k}}{|\mathbf{k}|}. \quad (2.31)$$

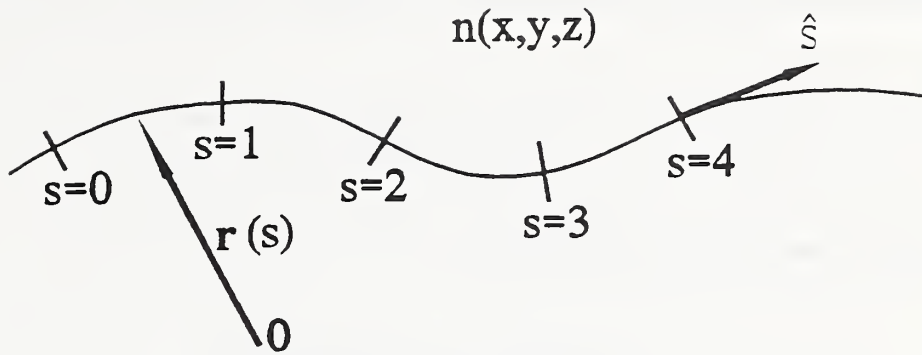


Figure 2.4. A sketch of a ray path in a spatially varying medium of index  $n(x,y,z)$ , where  $s$  is the distance measured along the ray path,  $\hat{s}(s)$  is the unit direction of the ray path at  $s$  and  $r(s)$  is the vector describing the ray path.

Vector  $\mathbf{k}$  can be represented by its components in the three coordinates (see Figure 2.5):

$$\mathbf{k} = k_r \hat{e}_r + k_\phi \hat{e}_\phi + k_z \hat{e}_z. \quad (2.32)$$

The  $z$  component of the  $k$  vector is just  $\beta$ , the propagation constant. From Equations (2.28), (2.31) and (2.32), we obtain the following expression for the  $z$  direction

$$\beta = n(r) k_0 \frac{dz}{ds}. \quad (2.33)$$

The  $z$  component of the ray equation in cylindrical coordinates (Equation

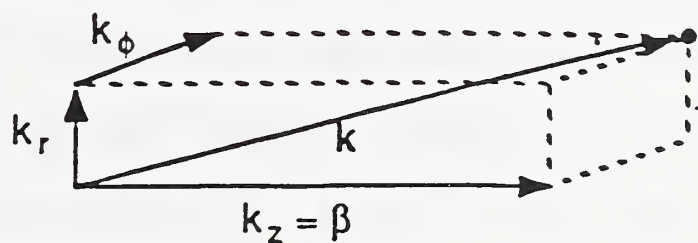


Figure 2.5: A sketch which defines the components of the  $\mathbf{k}$  vector.

The  $z$  component of the ray equation (Equation (2.30)) in cylindrical coordinates is

$$\frac{d}{ds} \left( n(r) \frac{dz}{ds} \right) = 0, \quad (2.34)$$

which can be rewritten in the form

$$n(r) k_0 \frac{dz}{ds} = \text{constant} = \beta, \quad (2.35)$$

where the last equal sign comes from Equation (2.33). Note that  $dz/ds$  is the cosine of the angle representing the angular direction of a ray with respect to the  $z$  axis. Using this fact, together with Equation (2.6) for parabolic index profile, Equation (2.35) can be expressed in the form

$$\frac{\beta^2}{k_1^2} = [1 - 2\Delta(\frac{r}{a})^2][1 - \sin^2 \theta(z)]. \quad (2.36)$$

The weakly guiding assumption implies that  $\Delta$  is small and that  $\theta^2$  is of the same order. We can then expand Equation (2.36) to obtain

$$\begin{aligned} R^2 &= \frac{1}{2\Delta} \left[ 1 - \frac{\beta^2}{k_1^2} \right] \\ &= \left[ \frac{r(z)}{a} \right]^2 + \frac{\sin^2 \theta(z)}{2\Delta} \\ &= \left[ \frac{r(z)}{a} \right]^2 + \frac{\sin^2 \theta(z)}{(NA/n_1)^2}, \end{aligned} \quad (2.37)$$

where  $R$  is the mode parameter which is the bridge between ray and wave optics.  $NA/n_1$  is the numerical aperture inside the fiber. Since  $\beta$  is a constant for a mode,  $R$  also is a constant for a mode. This also means that the right side of the last equal sign in Equation (2.37) defines an invariant along a ray path. As is sketched in Figure 2.6, a constant  $R$  parameter defines rays whose angles must decrease with increasing radius from the axis. This is by definition a bound mode. Further, the value of  $R$  is between 0 (lowest-order mode) and

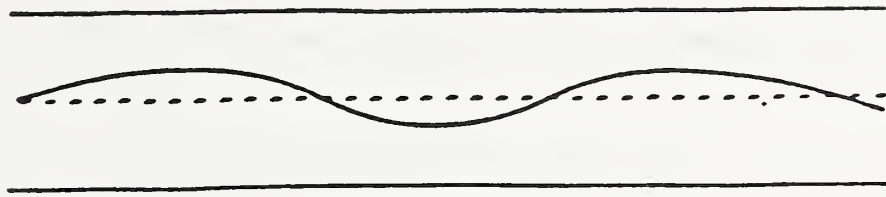


Figure 2.6: Path of a ray with mode parameter  $R$ .

1 (cutoff). Since a group of degenerate modes with the same principal mode number  $m$  have the same  $\beta$  (Section 2.2), mode parameter  $R$  actually represents a group of degenerate modes. Thus we will often say mode group  $R$  as well as mode  $R$ . Using Equations (2.19), (2.20) and (2.37), we obtain

$$R^2 = \frac{2m}{V}. \quad (2.38)$$

## 2.4 Mode Continuum

As was stated in Section 2.2, the principal mode number  $m$  as well as the radial and azimuthal mode numbers  $\mu$  and  $\nu$  can only take integral values. This means that modes are discrete and the propagation constant  $\beta$  of modes in a fiber also forms a discrete set. As a result,  $R$  can take on only discrete values. This discretization of modes can be depicted in the  $\beta$  spectrum by delta spikes at certain values of  $\beta$ , as is shown in Figure 2.7(a). The spacing between the values of  $\beta$  of two adjacent modes is

$$\begin{aligned} \Delta\beta &= \beta_{m+1} - \beta_m \\ &= n_1 k_0 \sqrt{1 - \frac{\sqrt{2\Delta}}{n_1 k_0 a} \frac{m+1}{N}} - n_1 k_0 \sqrt{1 - \frac{\sqrt{2\Delta}}{n_1 k_0 a} \frac{m}{N}} \\ &= \frac{\sqrt{2\Delta}}{a}. \end{aligned} \quad (2.39)$$

However, the values of  $\beta$  are directly affected by the wavelength of the source through the factor  $k_0$ . In fact, a source of linewidth  $\delta\lambda$  at a central frequency  $\lambda$  would induce a spread of  $\delta\beta$  in  $\beta$  space, the spread is given by

$$\delta\beta = \beta(\lambda) - \beta(\lambda + \delta\lambda) = \bar{n}_1 k_0 \frac{\delta\lambda}{\lambda}, \quad (2.40)$$

where  $\bar{n}_1 = \lambda \frac{dn_1}{d\lambda} - n_1$  is the group index. Clearly, if  $\delta\beta \gg \Delta\beta$ , then the  $\beta$  spectrum will become a continuum [31] between the cutoff points as is depicted in Figure 2.7(b).

Using Equation (2.39) and (2.40), we obtain the condition for a continuum of  $\beta$ :

$$\frac{\delta\lambda}{\lambda} > \frac{\sqrt{2\Delta}}{\bar{n}_1 k_0 a} = \frac{2\Delta}{V} = \frac{1}{n_1^2} \frac{(NA)^2}{V}. \quad (2.41)$$

With the typical numbers for a  $50 \mu m$  diameter,  $0.2 NA$  fiber, of  $V=35$ , the limit on  $\delta\lambda$  is

$$\frac{\delta\lambda}{\lambda} > 5 \times 10^{-4}. \quad (2.42)$$

Equation (2.42) is satisfied in most practical cases where multimode sources are used to excite multimode fibers. The typical value of  $\Delta$  is 0.01, of  $n_1$  is 1.46, of  $a$  is  $50 \mu m$ . For wavelength  $\lambda = 1.33 \mu m$ , if  $\Delta\lambda \geq 10^{-3}$ , Equation (2.42) is satisfied. A typical multimode laser diode has a linewidth of  $\frac{\delta\lambda}{\lambda} > 5 \times 10^{-3}$ . Single-mode sources are not used for multimode fiber excitation because of the severe modal noise [32, 33, 34, 35] caused by the interference between different propagation modes.

However, the continuum of  $\beta$  does not necessarily lead to a continuum of  $R$ , and it is  $R$  that dictates whether a continuum of ray paths exist. The reason is that the variation of  $\lambda$  will cause a variation of  $k$  as well as of  $\beta$ . Thus, due to Equation (2.37), the  $\beta$  continuum caused by the source linewidth does

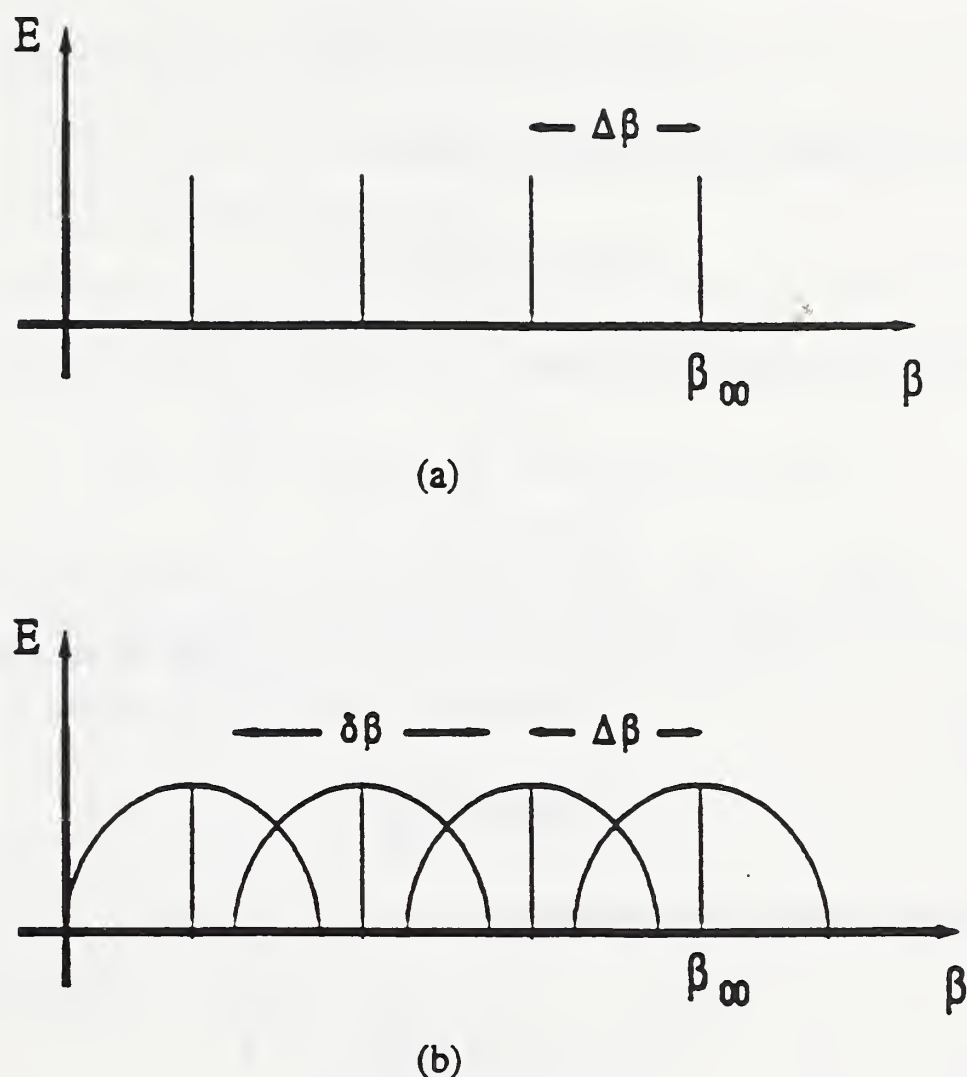


Figure 2.7. A sketch of a  $\beta$  spectrum for a multimode waveguide excited with (a) a monochromatic source and (b) a source whose spectral width induces a spread  $\delta\beta$  which greatly exceeds  $\Delta\beta$ .

not mean a corresponding continuum of  $R$ . The condition for the continuum of  $R$  must be sought in a different way. We will use the relation  $R^2 = 2m/V$  (Equation (2.38)). Adjacent modes are separated by

$$(R + \Delta R)^2 = \frac{2(m+1)}{V}. \quad (2.43)$$

Equations (2.38) and (2.43) yield the relation

$$(\Delta R)^2 + 2R\Delta R = \frac{2}{V}. \quad (2.44)$$

Solving Equation (2.44), we obtain

$$\Delta R = -R + \sqrt{R^2 + \frac{1}{V}} = R\left(\sqrt{1 + \frac{1}{2m}} - 1\right). \quad (2.45)$$

Since  $V = \sqrt{2\Delta}k_1a = \sqrt{n_1^2 - n_2^2}\frac{2\pi}{\lambda}a$  depends on  $\lambda$ , the variation of  $\lambda$  will cause a variation of  $V$ , which will in turn result in the variation of  $R$ . First we have the relation

$$2\frac{dR}{R} = -\frac{dV}{V}. \quad (2.46)$$

From the expression of  $V$  we obtain

$$\begin{aligned} \frac{dV}{V} &= \left(\frac{\lambda}{n_1 + n_2} \frac{dn}{d\lambda} - 1\right) \frac{d\lambda}{\lambda} \\ &\simeq \frac{1}{2n} (\hat{n} - n) \frac{d\lambda}{\lambda} \\ &\simeq -\frac{d\lambda}{\lambda}. \end{aligned} \quad (2.47)$$

From Equations (2.46) and (2.47), we obtain

$$dR = \frac{R}{2} \frac{d\lambda}{\lambda}. \quad (2.48)$$

For a mode continuum, we must have  $dR \geq \Delta R$ . The condition for mode continuum is then

$$\frac{d\lambda}{\lambda} \geq 2\left(\sqrt{1 + \frac{1}{2m}} - 1\right). \quad (2.49)$$

This mode continuum condition depends on the principal mode number  $m$  and can be further approximated to

$$\frac{d\lambda}{\lambda} \geq \frac{1}{2m}. \quad (2.50)$$

A much broader spectrum must be used for a continuum of  $R$  than for a continuum of  $\beta$ . Most practical light sources can still satisfy the condition of mode continuum for higher-order modes.

We will use very often a concept of mode density when modes constitute a continuum. With discrete modes, the total power in the guided modes is given by

$$P_t = \sum_i^M mp(m), \quad (2.51)$$

where  $M$  is the maximum principal mode number. When the modes become continuous, Equation (2.51) can be replaced by

$$P_t = \int_0^M mp(m)dm, \quad (2.52)$$

where  $m$  is now continuous. Changing variables from  $m$  to  $R$  by using Equation (2.38), we obtain

$$P_t = \frac{V^2}{2} \int_0^1 R^3 p(R)dR. \quad (2.53)$$

Equation (2.53) implies that mode density in  $R$  space is

$$m(R) = \frac{V^2}{2} R^3, \quad (2.54)$$

where  $m(R)$  designates the mode density of mode group  $R$ . The letter  $m$  here has a different meaning than the principal mode number  $m$ . In the following, we shall often omit the constant factor  $V^2/2$  and simply say that the mode density is  $R^3$ . The total power in mode group  $R$  is given by

$$P(R) = R^3 p(R). \quad (2.55)$$

We can infer from Equation (2.55) that in most cases lower-order modes carry much less power than the higher-order modes. Thus the higher-order modes play a more significant role in the power propagation behavior of the fiber than the lower-order modes. Therefore, we will use the mode continuum approximation for all the modes even though the condition is not satisfied for the lower-order modes.

## 2.5 Phase Space

Phase space is a two-dimensional coordinate system illustrated in Figure 2.8, in which the horizontal axis is the index profile function  $f(s)$ , where  $s = r/a$  is the normalized radial position of a ray, and the vertical axis is the square of the normalized numerical aperture  $t = \sin \theta/NA$  of the ray in the fiber. For a parabolic index fiber,  $f(s) = s^2$ . From the definition of mode parameter  $R$  of Equation (2.37), a particular mode with the parameter  $R$  is represented in phase space by a straight line which lies at an angle of  $45^\circ$  to the axes and intersects the axes where  $s^2 = R^2$  and  $t^2 = R^2$ . All the guided modes lie in the area under the line  $R^2 = 1$ . Above this line, are leaky modes and radiation modes.

For a step index fiber, modes with parameter  $R$  are represented by a line parallel to the horizontal axis and intercepts with the vertical axis at  $t^2 = R^2$ , as shown in Figure 2.8(b).

The power in all the degenerate modes with the same parameter  $R$  is uniformly distributed along the line representing mode  $R$ .

The relation between the nearfield pattern and the modal power distribution can be derived straightforwardly in the phase space representation. As is illustrated in Figure 2.9(a), the total power at radial position  $s$  is the

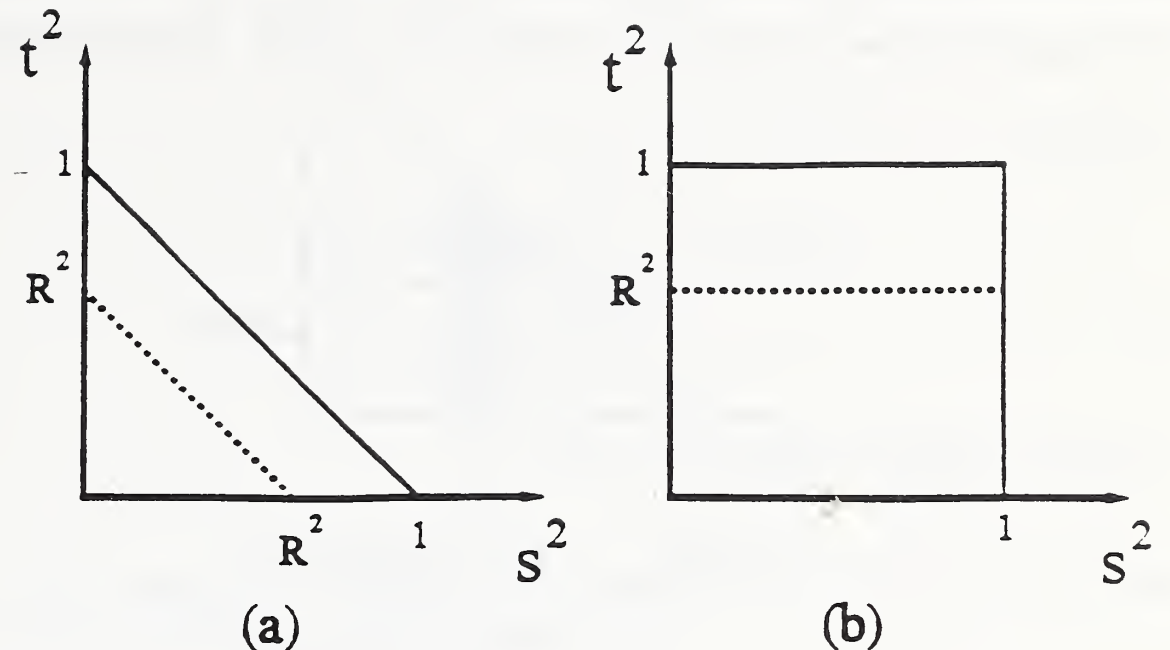


Figure 2.8. Phase space presentation of modes for (a) parabolic index fiber, and (b) step index fiber.

integral of all the power in the modes that are present at this position. Only those modes with a parameter  $1 > R > s$  will be present at  $s$ . Since the mode spacing in the phase space is  $R^2$ , the total power at  $s$  in the area element  $ds^2 dt^2$  in phase space is

$$p(s)dA = K p(R)ds^2 dt^2, \quad (2.56)$$

where  $K$  is mode density in the phase space.  $K$  can be determined in the following way. Since mode density in  $R$  space is  $V^2 R^3 / 2$ , we have

$$\frac{V^2}{2} R^3 dR = \frac{V^2}{4} R^2 dR^2. \quad (2.57)$$

This equation means that mode density is  $V^2 R^2 / 4$  in  $R^2$  space. Phase space represents the  $R^2$  space. The length of the straight line representing mode group  $R$  in phase space is  $R^2$ . Thus the mode density in phase space is  $V^2 / 4$ ,

which is constant throughout phase space and is the  $K$  of Equation (2.56). In phase space we also have the relation  $R^2 = s^2 + t^2$ . Thus Equation (2.56) becomes

$$\begin{aligned} p(s)dA &= \frac{V^2}{4}p(R)ds^2d(R^2 - s^2) \\ &= \frac{V^2}{4}p(R)(ds^2dR^2 - ds^2ds^2). \end{aligned} \quad (2.58)$$

The total power at position  $s$  is then

$$\begin{aligned} P(s)ds^2 &= \int_s^1 \frac{V^2}{4}p(R)ds^2dR^2 \\ &= V^2sds \int_s^1 p(R)RdR. \end{aligned} \quad (2.59)$$

The term with  $ds^2ds^2$  in Equation (2.58) has no contribution to this integral over  $R^2$ . All this power is distributed along the annular element of radius  $s$  and width  $ds$  (Figure 2.9). Thus the nearfield intensity at  $s$  is

$$\begin{aligned} I(s) &= \frac{P(s)ds^2}{2\pi sds} \\ &= \frac{V^2}{2\pi} \int_s^1 p(R)RdR. \end{aligned} \quad (2.60)$$

Taking derivatives with respect to  $s$  on both sides of this equation, we get

$$p(R) = -\frac{2\pi}{V^2} \frac{1}{\partial f/\partial s} \frac{dI(s)}{ds} |_{s=R}. \quad (2.61)$$

This same expression was obtained earlier from different approaches [27, 31, 36, 37, 38]. Since the measured nearfield pattern is always in a normalized scale, the constant factors in these two equations are never used in practice.

Similarly, we can derive the relation between the farfield pattern and the modal power distribution. In phase space representation, parameters  $t$  and

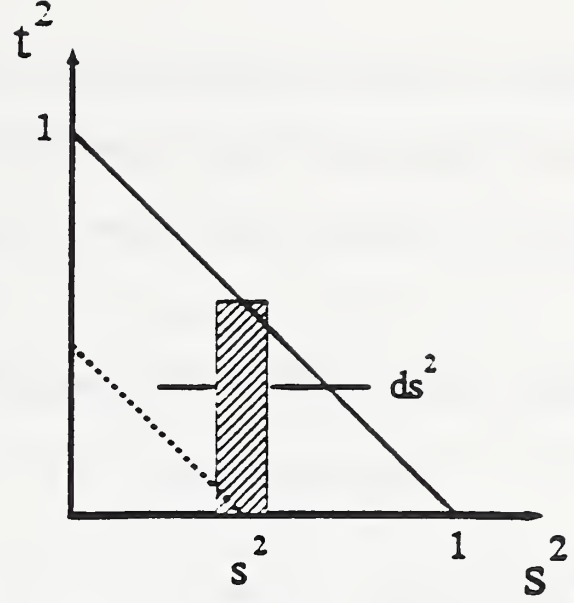


Figure 2.9. Depiction of derivation of nearfield power distribution  $I(s)$  from modal power distribution  $p(R)$  in phase space.

$s$  are symmetrical. We can then in Equations (2.60) and (2.61) replace  $s$  with  $t$  and get

$$I(t) = \frac{V^2}{2\pi} \int_t^1 p(R) R dR \quad (2.62)$$

and

$$p(R) = -\frac{2\pi}{V^2} \frac{1}{\partial f/\partial t} \frac{dI(t)}{dt} \Big|_{t=R}, \quad (2.63)$$

or in terms of  $\theta$

$$I(\theta) = \frac{V^2}{2\pi} \int_{n_1 \sin \theta / NA}^1 p(R) R dR \quad (2.64)$$

and

$$p(R) = -\frac{2\pi}{V^2} \frac{1}{\partial f/\partial \theta} \frac{dI(\theta)}{d\theta} \Big|_{\theta=\sin^{-1}(RN_A/n_1)}. \quad (2.65)$$

For overfilled launch,  $p(R) = 1$  and Equation (2.64) yields

$$\begin{aligned} I(\theta) &= \frac{V^2}{2\pi} \left( 1 - \frac{\sin^2 \theta}{NA^2/n_1^2} \right) \\ &= P(0) \left( 1 - \frac{\sin^2 \theta}{2n_1^2 \Delta} \right), \end{aligned} \quad (2.66)$$

which was first derived by Gloge and Marcatili in Reference [24].

In phase space, an incident light spot with uniform intensity and a Lambertian angular distribution will create a uniform modal power distribution. This kind of launch is called an overfilled excitation. The argument is as follows.

The solid angle element of the incident light at the angle  $\theta$  is

$$d\Omega = 2\pi \sin \theta d\theta. \quad (2.67)$$

The area element of the annulus at radius  $r$  is

$$dA = 2\pi r dr. \quad (2.68)$$

The incident Lambertian light has irradiance

$$I(\theta) = I(0) \cos \theta. \quad (2.69)$$

Thus the total power received at  $r$  and  $\theta$  is

$$\begin{aligned} P(r, \theta) &= 4\pi^2 I(0) r dr \cos \theta \sin \theta d\theta \\ &= \pi^2 a^2 (NA)^2 I(0) ds^2 dt^2. \end{aligned} \quad (2.70)$$

Since  $ds^2 dt^2$  is the area element in the phase space, Equation (2.20) means that the incident light distribution is uniform in phase space, or  $p(R)$  is constant.

The equations relating the nearfield and farfield patterns and the modal power distribution (Equations 2.60, 2.61, 2.64, and 2.65) were derived using the mode continuum assumption. However, when the light source has a narrower bandwidth, or when the input light is well collimated, as in the case of plane wave launch (Section 3.4), the light will have relatively higher degree of temporal and/or spatial coherence and the measured nearfield or farfield pattern will have ripples due to interference (these ripples are significantly different from noise fluctuations). Using Equation (2.61) or (2.65) to

determine modal power distribution will result in negative values of  $p(R)$  at certain values of  $R$ . The appearance of these negative values can be treated in the following way. In the continuum limit,  $p(R)$  at a single value of  $R$  indeed carries no power. Only the integral of  $p(R)$  in a certain range of  $R$  will give us the power of some discrete mode, which should be positive. In the partially coherent situation, modes will not be completely continuous; that is, there will be some spread of  $R$  but no overlapping. Thus these negative values are an indication of a certain degree of coherence. Since the actual nearfield pattern can be obtained from the modal power distribution with these negative values by using Equations (2.61) and (2.65), we will call this kind of modal power distribution a generalized modal power distribution. The generalized modal power distribution can formally be treated the same as the normal (positive definite) modal power distribution. Experimental results presented in Chapter 5 show that when the transfer function is applied to the generalized input modal power distribution, we can get the right output modal power distribution. Various authors have studied the generalized radiance, a quantity which roughly corresponds to a free space version of the generalized modal power distribution (Walther [39, 40], Wolf [41, 42]).

## CHAPTER 3

# MODE TRANSFER MATRIX (MTM) AND MODE TRANSFER FUNCTION (MTF)

### 3.1 Introduction

In this chapter, we will discuss the mode transfer matrix method and the mode transfer function method. We will use the mode transfer function to analyze the precision of the mode transfer matrix. Expressions have been derived which show how the transfer matrices can deviate from the ideal matrix due to the finite discretization and nonideal modal power distribution. Relations between the measured matrix and the matrices corresponding to the launch conditions involved in the measurement are also derived. With this analysis the measurement results can be better understood. The experimental setup and procedures are discussed. Experimental results of transfer matrices, especially those of a round-robin measurement test conducted in collaboration with the NIST and TIA are presented. Measured transfer functions will be shown in Chapter 5, where details of transfer functions for different devices are discussed.

### 3.2 MTM Technique

In 1981, G. T. Holmes proposed using a mode transfer matrix to model modal power redistribution in optical fiber devices [14]. The basic tenet of his technique is that all the modes in an optical fiber component can be divided into  $n$  mode groups. The power incident on a component is represented by a

vector  $\mathbf{P}^i$  and the power exiting the component by a vector  $\mathbf{P}^o$ , both being  $n$ -dimensional. A component can be represented by a  $n \times n$  matrix  $\mathbf{T}$ . The diagonal elements of this matrix represent proportions of power remaining in each mode group after going through the component, and all the other elements represent proportions of power transferred from one mode group to another. For example, element  $t_{ij}$  represents the proportion of power in mode group  $j$  transferred to mode group  $i$ . The transfer matrix is defined by the matrix relation

$$\mathbf{P}^o = \mathbf{T}\mathbf{P}^i, \quad (3.1)$$

where

$$\mathbf{T} = \begin{bmatrix} t_{11} & t_{12} & \cdots & t_{1n} \\ t_{21} & t_{22} & \cdots & t_{2n} \\ \vdots & \vdots & \ddots & \vdots \\ t_{n1} & t_{n2} & \cdots & t_{nn} \end{bmatrix}, \quad (3.2)$$

$$\mathbf{P}^o = \begin{bmatrix} P_{o1} \\ P_{o2} \\ \vdots \\ P_{on} \end{bmatrix}, \mathbf{P}^i = \begin{bmatrix} P_{i1} \\ P_{i2} \\ \vdots \\ P_{in} \end{bmatrix}. \quad (3.3)$$

Using Equation (2.53), we can make the identifications

$$\begin{aligned} P_j^o &= \int_{R_{j-1}}^{R_j} p^o(R)m(R)dR \quad \text{for } 1 \leq j \leq n, \\ P_j^i &= \int_{R_{j-1}}^{R_j} p^i(R)m(R)dR \quad \text{for } 1 \leq j \leq n, \end{aligned} \quad (3.4)$$

where  $R_o = 0$  and  $R_n = 1$ . Matrix  $\mathbf{T}$  has  $n^2$  elements while  $\mathbf{P}^o$  and  $\mathbf{P}^i$  have only  $n$  elements each. Therefore, although Equation (3.1) defines matrix  $\mathbf{T}$ , it is not sufficient to solve for  $\mathbf{T}$ . We need  $n^2$  equations to determine the  $n^2$

components of  $\mathbf{T}$ . This can be done by making  $n$  independent excitations. What we mean by ‘independent excitation’ is that the  $n$  input power vectors we get from these  $n$  excitations are linearly independent. We can thus get  $n$  input and output power vectors and form  $\mathbf{P}^o$  and  $\mathbf{P}^i$  according to the rules

$$\mathbf{P}^o = [\mathbf{P}_1^o, \mathbf{P}_2^o, \dots, \mathbf{P}_n^o], \quad (3.5)$$

$$\mathbf{P}^i = [\mathbf{P}_1^i, \mathbf{P}_2^i, \dots, \mathbf{P}_n^i], \quad (3.6)$$

where  $\mathbf{P}_j^o(\mathbf{P}_j^i)$  is the output (input) vector for the  $j$ th independent excitation. With these matrices, we can now write the analog of Equation (3.1)

$$\mathbf{P}^o = \mathbf{T}\mathbf{P}^i, \quad (3.7)$$

which can be solved for  $\mathbf{T}$  to yield

$$\mathbf{T} = \mathbf{P}^o[\mathbf{P}^i]^{-1}. \quad (3.8)$$

Though modal power distribution cannot be measured directly, it can be determined from the nearfield pattern by Equation (2.61). Thus the experimental determination of the  $n \times n$  mode transfer matrix of a particular fiber-optic component requires the measurements of  $n$  input and output nearfield patterns of the  $n$  independent launches. Input and output power values also need to be measured in order to determine the relative values of  $\mathbf{P}^o$  and  $\mathbf{P}^i$ .

Since the mode transfer matrix takes power coupling between different modes into account, it represents a more accurate approach to the characterization of multimode fiber-optic components than a single loss value. Indeed, the tool has been successfully applied to the prediction of loss in fusion splice [43], microbends [44], connectors [45], power splitters [46], and fibers [47], as well as

to the prediction of system bandwidth [48]. It is also used in the loss prediction of step index LAN link [19]. The MTM method has been adopted by the industry as a candidate for the standard method of optical fiber components and systems characterization.

### 3.3 Definition of MTF

In the mode transfer matrix approach of the last section, the choice of the discretization of Equation (3.4) is somewhat arbitrary, because there is no rule on how to discretize the modes. But in fact, if we have a mode continuum, it is not necessary to discretize the modes. Instead of input and output modal power vectors, we have input and output modal power distributions in terms of the mode parameter  $R$ . The output distribution can be represented as an integral operator operating on an incident distribution [49]:

$$P^o(R) = \hat{T}P^i(R), \quad (3.9)$$

where  $P^o(R)$  and  $P^i(R)$  are the total output and input power in mode group  $R$  and are given by

$$\begin{aligned} P^o(R) &= p^o(R)m(R), \\ P^i(R) &= p^i(R)m(R). \end{aligned} \quad (3.10)$$

The kernel of this operator is the transfer function  $T(R, R')$  defined as

$$p^o(R)m(R) = \int_0^1 T(R, R')p^i(R')m(R')dR'. \quad (3.11)$$

This transfer function can therefore be taken as the object which represents given fiber components, at least in practical systems where the mode continuum approximation applies.

The main task of the transfer function approach is to find specific

forms of the transfer function for different kinds of devices. The transfer function would have some free parameters that need to be determined for individual components. The form of the transfer function characterizes the kind of device, while the values of the free parameters characterize the individual components. It is left for Chapters 4 and 5 to derive the transfer functions for some of the most commonly used devices in optical fiber communications.

From the definition of the transfer function of Equation (3.11), it is possible that one single launch measurement could determine the transfer function of a particular component, which is a great practical advantage over the transfer matrix approach.

### 3.4 MTM as a Truncation of MTF

Though the MTM method has achieved some success in characterizing optical fiber systems, it has long been known that the MTM is dependent on model power distribution incident on the component [18, 19]. However, detailed analysis has never been given. In the following, we will show how the measured matrix is dependent on the launch conditions.

Equation (3.9) defines the effect of a component in a rigorous sense. To find a matrix corresponding to the operator  $\hat{T}$  of Equation (3.9), we choose an orthogonal basis of functions  $\phi_k(R)$  and find that [49]

$$t_{jk} = \frac{1}{E_k} \int_0^1 dR \phi_j(R) \hat{T} \phi_k(R), \quad (3.12)$$

where

$$E_k = \int_0^1 dR \phi_k^2(R), \quad (3.13)$$

with the power vectors of Equation (3.4) now given by

$$P_j^o = \int_0^1 dR p^o(R) m(R) \phi_j(R), \quad (3.14)$$

$$P_j^i = \int_0^1 dR p^i(R) m(R) \phi_j(R). \quad (3.15)$$

Whereas in Equations (3.1 - 3.4), it was assumed that the power vectors could be chosen of an arbitrary dimension  $n$ , here it is evident that the power vectors are infinite-dimensional because it takes an infinite number of functions  $p(R)$  to span the space  $0 \leq R \leq 1$ . In the two mode group case, however, we could choose

$$\phi_{2j+1} = \frac{1}{m(R)} \begin{cases} a_{2j+1} \cos(R - \frac{R_c}{2}) \frac{2\pi}{R_c} \\ a_{2j+1} \sin(R - \frac{R_c}{2}) \frac{2\pi}{R_c} \end{cases} \quad 0 < R < R_c, \quad j = 0, 1, 2, \dots, \quad (3.16)$$

$$\phi_{2j} = \frac{1}{m(R)} \begin{cases} b_{2j} \cos(R - \frac{1+R_c}{2}) \frac{2\pi}{1-R_c} \\ b_{2j} \sin(R - \frac{1+R_c}{2}) \frac{2\pi}{1-R_c} \end{cases} \quad 0 < R < R_c, \quad j = 0, 1, 2, \dots, \quad (3.17)$$

which is just a double Fourier series, one on  $[0, R_c]$  and one on  $[R_c, 1]$ . The first terms of  $\phi_1(R)$  and  $\phi_2(R)$  are rectangle functions which have the value 1 on the two intervals, respectively. They represent the amount of power in the two mode groups, incident or exiting. The rest of the terms of these two vectors describe the shape of modal power distribution in the two mode groups. The terms  $t_{jk}$  for  $j, k = 1, 2$ , purely represent modal power transfer of the two mode groups regardless of the variation of model power distribution in the two modes, which is portrayed by all the other terms. Therefore, the values of  $t_{jk}$  for  $j, k = 1, 2$ , and the first two elements of the power vectors are exactly those which are defined for a  $2 \times 2$  case from Equations (3.1 - 3.4). Unfortunately, there are still a countable infinity of terms left over. To clarify what these

other terms do, we pick a set of  $n$  excitations. We can then choose input and output matrices as in Equation (3.6). These matrices will now have dimensions of  $\infty \times n$ . Clearly, Equation (3.8) will still hold except that now the transfer matrix will have dimensions of  $\infty \times \infty$ . If we had the correct power matrices, we could perform the operations of Equation (3.8) and then truncate to  $n \times n$  to obtain a transfer matrix we will denote by  $\mathbf{T}^e$ , meaning the exact  $\mathbf{T}$ . However, in practice we do not determine the exact power matrices but use truncated  $n \times n$  versions  $\mathbf{P}^{oT}$  and  $\mathbf{P}^{iT}$  to determine the measured transfer matrix  $\mathbf{T}^{(m)}$ . This operation is not the same as calculating directly, as can be denoted by writing

$$\begin{aligned}\mathbf{T}^{(m)} &= \mathbf{P}^{oT}(\mathbf{P}^{iT})^{-1} \\ &= \mathbf{T}^e + \mathbf{T}^+ \mathbf{P}^{i+}(\mathbf{P}^{iT})^{-1},\end{aligned}\quad (3.18)$$

where  $\mathbf{T}^+$  is the transfer matrix with the first  $n$  columns replaced by zero vectors and  $\mathbf{P}^{i+}$  is the excitation matrix with its first  $n$  rows replaced by zeros, a situation illustrated in Figure (3.1).

A major point of this argument is that the truncation of the power matrices causes an added error. The only way this error can be made to go away is if the  $\mathbf{P}^{i+}$  is identically zero. Equations (3.14) and (3.15) show that this could be the case only if

$$\int_0^1 dR p^i(R) m(R) \phi_j(R) = 0, \forall j > n, \text{ and } p^i(R); \quad (3.19)$$

that is, if all the  $n$  excitations were orthogonal to all the basis functions. In the double Fourier series example of Equations (3.16) and (3.17) as applied to a  $2 \times 2$  case, the two excitations would have to be perfectly flat modal distributions, the first flat between 0 and  $R_c$  and the second flat between  $R_c$  and 1. This

$$\begin{aligned}
 P^{0T} &= T^e P^{iT} + T^* P^{i+} \\
 T^{(m)} &= P^{0T} (P^{iT})^{-1} \\
 &= T^e + T^* P^{i+} (P^{iT})^{-1}
 \end{aligned}$$

Figure 3.1: Truncation of the infinite-dimensional matrices.

is what is meant by orthogonal excitations. They cannot overlap and must be orthogonal to all higher-order terms. Unfortunately, the diffraction limit precludes us from actually generating such launches.

### 3.5 Dependence on Launch Conditions of the Measured Matrix

In the last section, we explained that the measured transfer matrix depends on the input modal power distribution. Since, as was described in Section 3.2,  $n$  independent launches are required for determining an  $n \times n$  matrix, the question naturally arises, What matrix is determined by the measurement of  $n$  outputs, given  $n$  conditions? For simplicity, we consider only the  $2 \times 2$  case. However, the conclusion can be generalized to the  $n \times n$  case. Clearly,

the power exiting a component can be expressed in the form

$$\begin{aligned} P^0 &= P_1^o + P_2^o \\ &= t_{11}P_1^i + t_{12}P_2^i + t_{21}P_1^i + t_{22}P_2^i. \end{aligned} \quad (3.20)$$

A second expression for the power can be found by writing Equation (3.4) in the form

$$\begin{aligned} P^0 &= \int_0^{R_c} dR \int_0^{R_c} dR' T(R, R') m(R') p^i(R') \\ &+ \int_0^{R_c} dR \int_{R_c}^1 dR' T(R, R') m(R') p^i(R') \\ &+ \int_{R_c}^1 dR \int_0^{R_c} dR' T(R, R') m(R') p^i(R') \\ &+ \int_{R_c}^1 dR \int_{R_c}^1 dR' T(R, R') m(R') p^i(R'). \end{aligned} \quad (3.21)$$

Each of the corresponding terms in Equations (3.20) and (3.21) have the same physical meaning; that is, the first term represents power coupled from the input lower-order mode group to the output lower-order mode group; the second term is power coupled from the input higher-order mode group to the output lower-order mode group; the third and fourth terms are power coupled to the output higher-order mode group from the input lower and higher mode groups, respectively. We can thus identify the corresponding terms in these two equations. Using Equation (3.4) to express the incident power vectors, we obtain

$$t_{11} = \frac{\int_0^{R_c} dR \int_0^{R_c} dR' T(R, R') m(R') p^i(R')}{\int_0^{R_c} dR' m(R') p^i(R')}, \quad (3.22)$$

$$t_{12} = \frac{\int_0^{R_c} dR \int_{R_c}^1 dR' T(R, R') m(R') p^i(R')}{\int_{R_c}^1 dR' m(R') p^i(R')}, \quad (3.23)$$

$$t_{21} = \frac{\int_{R_c}^1 dR \int_{R_c}^0 dR' T(R, R') m(R') p^i(R')}{\int_0^{R_c} dR' m(R') p^i(R')}, \quad (3.24)$$

$$t_{22} = \frac{\int_{R_c}^1 dR \int_{R_c}^1 dR' T(R, R') m(R') p^i(R')}{\int_{R_c}^1 dR' m(R') p^i(R')}. \quad (3.25)$$

Equations (3.22 - 3.25) show that the measured transfer matrix is simply a weighted average of the transfer function, where the weighting is given by the incident modal power distribution. In practice, however, several launches are needed to get one measured matrix. Different launches create different incident modal power distributions and each has a transfer matrix. Therefore, it is not clear what information the measured matrix gives us.

In the following, we will derive the relations between the measured matrix elements and the elements of each matrix corresponding to the different launch conditions. We will use superscripts (1) and (2) to denote power vectors, transfer matrices and matrix elements corresponding to the first and second launch, and superscript (m) for the measured results.

When the two launches are independent, from Equation (3.1) we have for the two launch conditions the following expressions:

$$\begin{pmatrix} P_{o1}^{(1)} \\ P_{o2}^{(1)} \end{pmatrix} = \begin{pmatrix} t_{11}^{(1)} & t_{12}^{(1)} \\ t_{21}^{(1)} & t_{22}^{(1)} \end{pmatrix} \begin{pmatrix} P_{i1}^{(1)} \\ P_{i2}^{(1)} \end{pmatrix}, \quad (3.26)$$

$$\begin{pmatrix} P_{o1}^{(2)} \\ P_{o2}^{(2)} \end{pmatrix} = \begin{pmatrix} t_{11}^{(2)} & t_{12}^{(2)} \\ t_{21}^{(2)} & t_{22}^{(2)} \end{pmatrix} \begin{pmatrix} P_{i1}^{(2)} \\ P_{i2}^{(2)} \end{pmatrix}. \quad (3.27)$$

We can write explicitly the expressions for the output power vector elements from the above equations:

$$P_{o1}^{(1)} = t_{11}^{(1)} P_{i1}^{(1)} + t_{12}^{(1)} P_{i2}^{(1)}, \quad (3.28)$$

$$P_{o2}^{(1)} = t_{21}^{(1)} P_{i1}^{(1)} + t_{22}^{(1)} P_{i2}^{(1)}, \quad (3.29)$$

$$P_{o1}^{(2)} = t_{11}^{(2)} P_{i1}^{(2)} + t_{12}^{(2)} P_{i2}^{(2)}, \quad (3.30)$$

$$P_{o2}^{(2)} = t_{21}^{(2)} P_{i1}^{(2)} + t_{22}^{(2)} P_{i2}^{(2)}. \quad (3.31)$$

However, for the measured matrix we should use Equation (3.7) and write in the present notation the following expression:

$$\begin{pmatrix} P_{o1}^{(1)} & P_{o1}^{(2)} \\ P_{o2}^{(1)} & P_{o2}^{(2)} \end{pmatrix} = \begin{pmatrix} t_{11}^{(m)} & t_{12}^{(m)} \\ t_{21}^{(m)} & t_{22}^{(m)} \end{pmatrix} \begin{pmatrix} P_{i1}^{(1)} & P_{i1}^{(2)} \\ P_{i2}^{(1)} & P_{i2}^{(2)} \end{pmatrix}. \quad (3.32)$$

Inserting Equations (3.28 - 3.31) into Equation (3.32) and solving for the measured matrix elements, we obtain the following relations:

$$t_{11}^m = \frac{t_{11}^{(1)} k_1 k_2 - t_{11}^{(2)} + [t_{12}^{(1)} - t_{12}^{(2)}] k_2}{k_1 k_2 - 1}, \quad (3.33)$$

$$t_{12}^m = \frac{t_{11}^{(2)} k_1 k_2 - t_{12}^{(2)} + [t_{11}^{(2)} - t_{11}^{(1)}] k_2}{k_1 k_2 - 1}, \quad (3.34)$$

$$t_{21}^m = \frac{t_{21}^{(1)} k_1 k_2 - t_{21}^{(2)} + [t_{22}^{(1)} - t_{22}^{(2)}] k_2}{k_1 k_2 - 1}, \quad (3.35)$$

$$t_{22}^m = \frac{t_{22}^{(2)} k_1 k_2 - t_{22}^{(1)} + [t_{21}^{(2)} - t_{21}^{(1)}] k_2}{k_1 k_2 - 1}, \quad (3.36)$$

where  $k_1$  and  $k_2$  are defined as

$$\begin{aligned} k_1 &= \frac{P_{i1}^{(1)}}{P_{i2}^{(1)}}, \\ k_2 &= \frac{P_{i1}^{(2)}}{P_{i2}^{(2)}}, \end{aligned} \quad (3.37)$$

which are power ratios of the two mode packets for the two launch conditions. If the launches become orthogonal, that is, if  $k_1$  and  $k_2$  approach  $\infty$ , then

$$\begin{aligned} t_{11}^m &= t_{11}^{(1)}, \\ t_{12}^m &= t_{12}^{(2)}, \\ t_{21}^m &= t_{21}^{(1)}, \\ t_{22}^m &= t_{22}^{(2)}. \end{aligned} \tag{3.38}$$

The measured matrix thus gives us some meaningful results; that is, it tells us at least two exact matrix elements for each launch condition. The other four missing elements are indeed useless because their values would not affect the power transfer results since  $P_{i2}^{(1)}$  and  $P_{i1}^{(2)}$ , on which they act, are zero. However,  $t_{11}^{(1)}$ ,  $t_{12}^{(2)}$ ,  $t_{21}^{(1)}$ , and  $t_{22}^{(2)}$  still depend on modal power distribution within the mode packets. When, in addition, the modal power distributions are flat, the measured matrix becomes the truncated version of the exact matrix, and the measured matrix represents exactly that for the ideal overfilled launch where the modal power distribution is all flat, that is,  $p(R) = 1$ . We might be able to create launch conditions that are almost orthogonal; that is,  $k_1$  and  $k_2$  are very large in a specially designed measurement system [50, 51]. However, in real application cases, the launch conditions can never be ideal and controlled. The measured matrix will never be completely accurate. Though the transfer matrix for any launch condition can never be measured except for the overfilled excitation, it is possible to create matrices for any input modal power distribution  $p^i(R)$  by using Equations (3.22 - 3.25), if the transfer function of the component is known. It is also possible to create matrices of any  $n \times n$  dimensions in the same way by using equations similar to (3.22 - 3.25).

Table 3.1. Measured matrix and matrices corresponding to the two excitations of one connector.

$$\begin{array}{c} \mathbf{T}^{(1)} \qquad \qquad \mathbf{T}^{(2)} \qquad \qquad \mathbf{T}^{(m)} \\ \left( \begin{array}{cc} 0.8779 & 0.1982 \\ 0.0976 & 0.3921 \end{array} \right) \quad \left( \begin{array}{cc} 0.7415 & 0.2274 \\ 0.2099 & 0.4014 \end{array} \right) \quad \left( \begin{array}{cc} 0.9508 & 0.0128 \\ 0.0158 & 0.6005 \end{array} \right) \end{array}$$

Table 3.2. Measured matrix and matrices corresponding to the two excitations of a second connector.

$$\begin{array}{c} \mathbf{T}^{(1)} \qquad \qquad \mathbf{T}^{(2)} \qquad \qquad \mathbf{T}^{(m)} \\ \left( \begin{array}{cc} 0.9026 & 0.1206 \\ 0.0401 & 0.6899 \end{array} \right) \quad \left( \begin{array}{cc} 0.8783 & 0.1207 \\ 0.0501 & 0.6910 \end{array} \right) \quad \left( \begin{array}{cc} 0.9259 & 0.0619 \\ 0.0296 & 0.7164 \end{array} \right) \end{array}$$

To give some idea of how the measured matrix is different from the matrices pertinent to the two excitations, the resultant matrices calculated from the transfer functions of two components are shown in Tables 3.1 and 3.2. Details about the transfer functions will be shown in Chapter 5, which deals specifically with transfer functions for different kinds of devices.

It is obvious from Tables 3.1 and 3.2 that the measured matrix is quite different from either of the matrices corresponding to the two excitations. In Table 3.1, one can see how the values of each matrix element in  $\mathbf{T}^{(m)}$  is different from the values of corresponding elements in  $\mathbf{T}^{(1)}$  and  $\mathbf{T}^{(2)}$ . In Table 3.2, though  $t_{12}^{(1)}$  and  $t_{12}^{(2)}$  have almost the same value,  $t_{12}^{(m)}$  is still very different from them. This is because the measured matrix element depends not only on the values of corresponding elements in  $\mathbf{T}^{(1)}$  and  $\mathbf{T}^{(2)}$ , but also on other elements, as can be seen in Equations (3.34 - 3.37). In some cases, we even get negative values for  $t_{12}^{(m)}$  or  $t_{21}^{(m)}$  and values greater than 1 for  $t_{11}^{(m)}$ . The measured matrix can

be meaningless.

### 3.6 Experimental Setup

The experimental apparatus is depicted in Figure 3.2. A 100-W halogen lamp with an ellipsoidal reflector was used as the source. The light source is focused onto a variable field stop by means of a  $5\times$  microscope objective. The combination of the lens of 100-mm focal length and input microscope objective of  $20\times$  magnification produces a demagnification of 10.96, since the focal length of the  $20\times$  lens is 9.12 mm. To select the range of the wavelengths, an infrared bandpass filter with center wavelength of 850 nm and a passband of 50 nm was employed. The variable field stop consists of three patterns. The first is a small hole with a diameter of 100  $\mu\text{m}$  which is used for central excitation; the second is used for off-central excitation and is an annulus which has an outer diameter of  $\sim 688 \mu\text{m}$  and an opaque center circle with a diameter of 525  $\mu\text{m}$ ; and the third is a large hole with a diameter of  $\sim 1.5 \text{ mm}$  which is used for overfilled excitation. The variable aperture stop provides a second control of launch conditions. The numerical aperture can be changed from 0.06 to 0.4.

In the receiving system, the fiber output is imaged with a  $60\times$  microscope lens onto a TV camera. The beam splitter allows 90% of the output to be transmitted to the camera channel and 10% to the power meter. This configuration allows most of the energy to be transmitted to the camera channel, since the power meter channel does not require a large signal with the lock-in amplifier sensitivity. The camera is a charge-coupled device (CCD) array camera which produces resolution in the horizontal direction of 280 TV lines and in the vertical direction of 350 TV lines. The nearfield intensity is then digitized with the use of a solid state video memory with high speed A-D

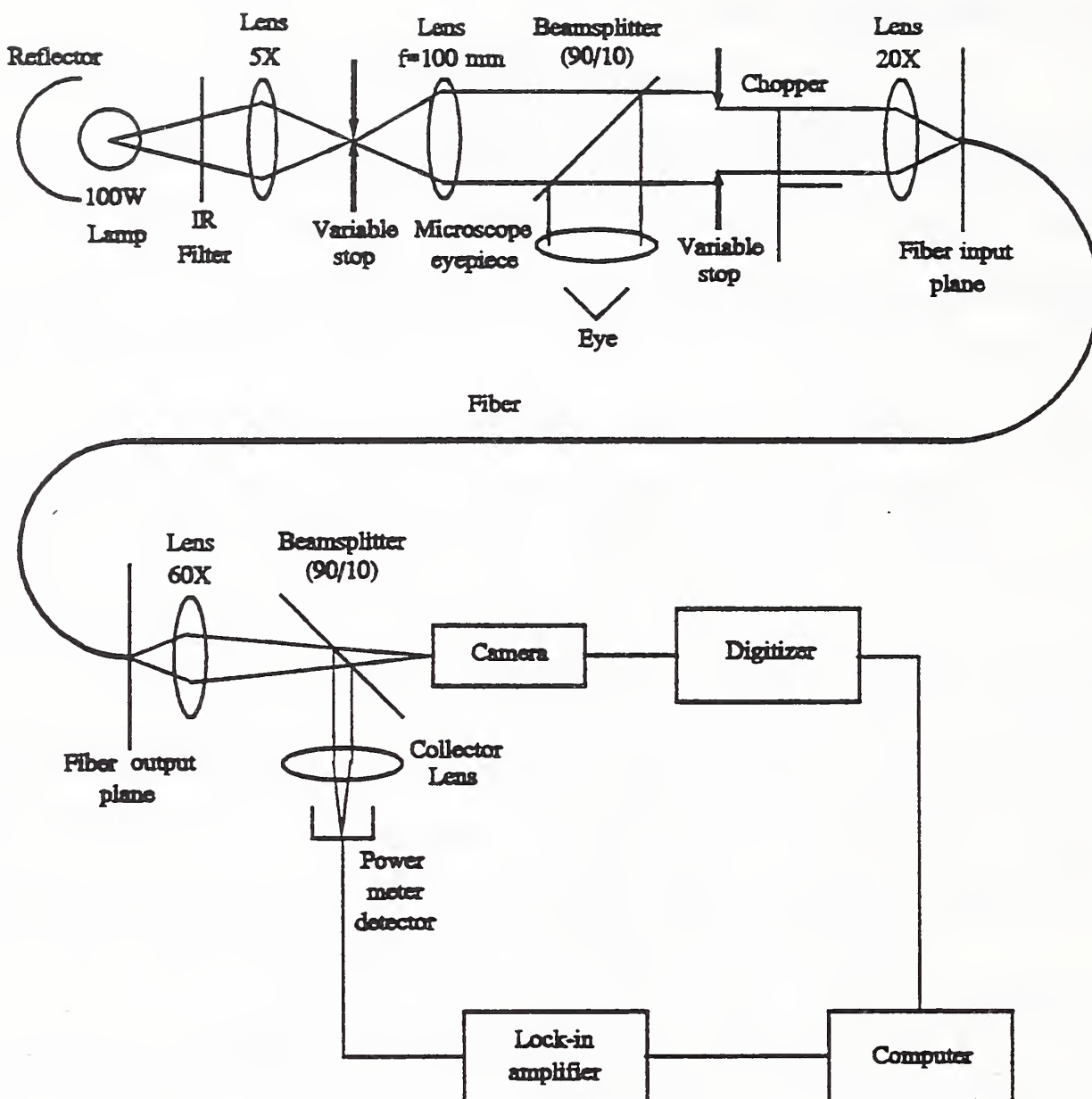


Figure 3.2: Schematic diagram of measurement set-up.

and D-A converters and capable of digitizing, storing, and displaying a single frame of video information. This unit uses standard 2:1 interlace and dot interlace to increase horizontal resolution. An I/O module is installed in the video frame store, which provides interfacing to a personal computer. Power measurements are critical in obtaining the transfer matrices. To obtain accurate power measurements, the software is written so that 100 power measurements are averaged. Also, the nearfield intensity measurement requires some caution. Here, the software is written so that the total nearfield intensity can be averaged for up to 80 measurements. The technique is much superior to the one used in mechanical scanning setups, since the high accuracy is achieved by simple and fast averaging. The chopper with the lock-in amplifier will improve the signal-to-noise ratio in power measurement. The speed of the system minimizes the noise-producing effects of thermal variation.

The variable field stop can provide three kinds of launches: central, overfilled, and off-central excitations. Central excitation is the kind of launch where the lower-order modes are excited with more power than higher-order modes. In the off-central launch, the higher-order modes have more power at input than the lower-order modes. When all the modes have the same input power, that is, when the input modal power distribution is uniform, the excitation is called overfilled. The practical overfilled launch may not be so ideal that the modal power distribution is completely uniform, but as long as the modal power distribution shows no significantly biased concentration it can be considered as an overfilled launch. Any two of these three excitations are independent launches. Figure 3.3 shows typical modal power distributions of the three kinds of excitations.

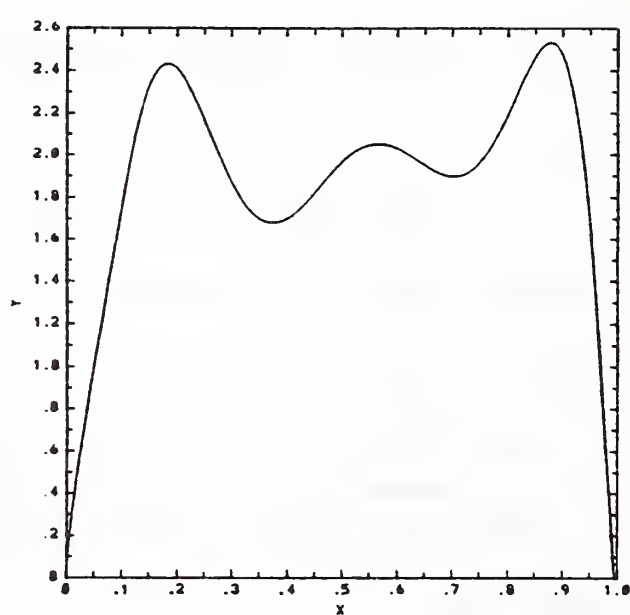
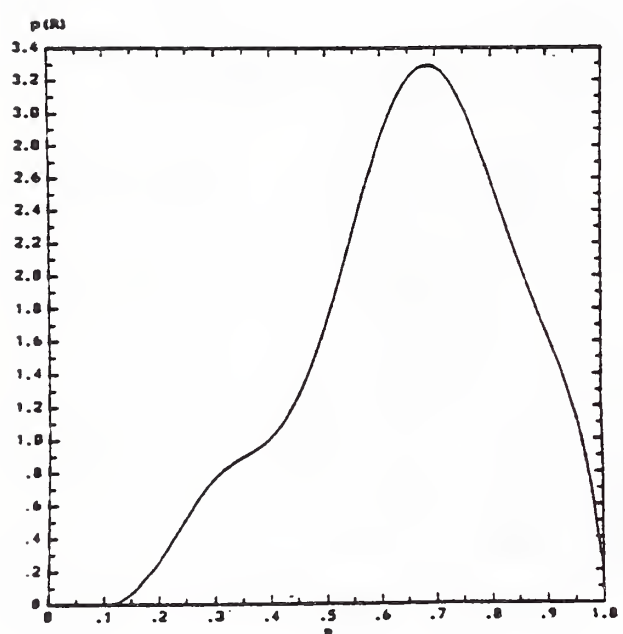
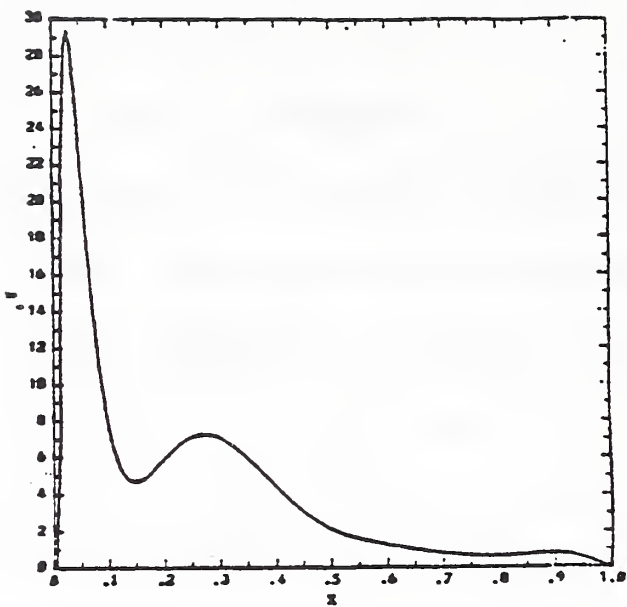


Figure 3.3. Typical modal power distributions of (a) central excitation, (b) off-central excitation, and (c) overfilled excitation.

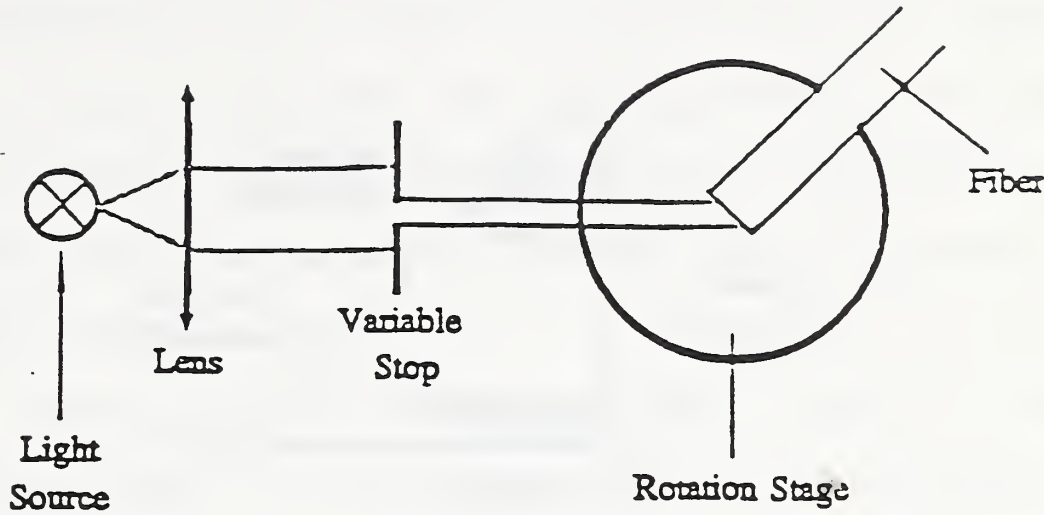


Figure 3.4. Schematic diagram of the incident part of plane wave launch setup.

Since the  $2 \times 2$  matrix is the least measurement-intensive, measurements were made with two different launch conditions for each component. In most cases, we use a combination of central and overfilled excitations. The other combination used is the overfilled and off-central excitations.

Another kind of launch, which is called plane wave launch [51], is used by some laboratories for the measurement of transfer matrix. The incident setup of the plane wave launch is sketched in Figure 3.4. A source with a small emitting area is used, which is usually a multimode laser diode or a light emitting diode (LED). The source is put at the focal point of a lens and the light beam is thus well collimated after going through the lens. The size of the beam can be varied by means of a variable aperture stop. The collimated beam is directed through the center of a rotating stage where the input fiber of the test component is laid. The end of the input fiber is placed right at the center of the stage. By rotating the stage and selecting the size of the

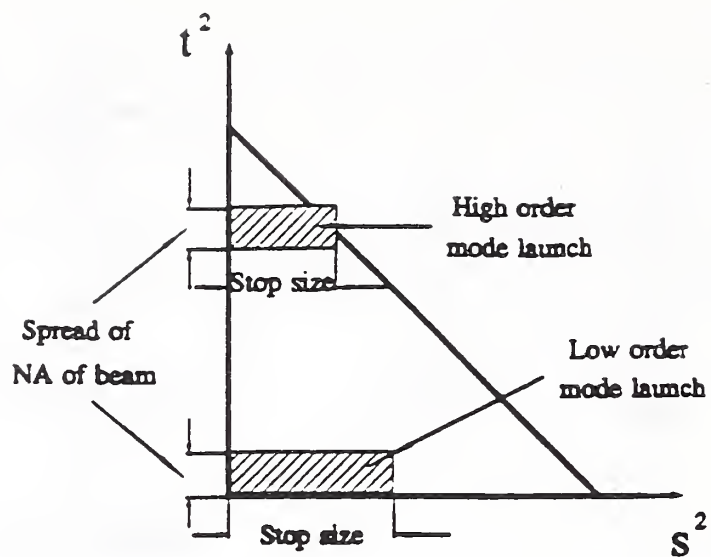


Figure 3.5: Phase space illustration of plane wave launch.

variable aperture stop, we can select the modes to be launched into the fiber. For example, when the beam is parallel to the optical axis of the input fiber and the aperture stop is relatively small, lower-order modes will be launched, whereas higher-order modes can be launched if the stage is rotated so that the incident beam is at an angle slightly less than the numerical aperture of the fiber with the optical axis of the fiber. Figure 3.5 illustrates these selective launches in phase space.

The plane wave launch has the advantage of selective launch. However, if the size of the aperture stop is not properly selected, high leaky mode power will be launched into the component. If the input nearfield pattern is not measured far enough from the input end, the input nearfield and modal power distribution will be distorted and hence error will be introduced. A second problem is that since the launch is also highly selective in azimuthal angle, the degenerate modes with the same mode number  $R$  may not attain equal power distribution at the measurement point. A third problem is related

to the second and invokes the high spatial coherence due to the collimation. The nearfield pattern may exhibit fluctuations which will make it difficult to calculate the modal power distribution and the generalized modal power distribution (Section 2.5) may be necessary to be adopted. Figure 3.6 shows the measured input nearfield pattern of a low-order mode and a high-order mode plane wave launch.

There are two ways to calculate modal power vectors  $\mathbf{P}^o$  and  $\mathbf{P}^i$  from the measured nearfield patterns. The first is to calculate the elements in the vectors directly from the nearfield. If the lower- and higher-order mode packets are divided at mode parameter  $R_c$ , element  $P_1$ , which is the power in the lower-order mode packet in either the input or the output power vector, can be expressed as

$$P_1 = \int_0^{R_c} p(R)m(R)dR. \quad (3.39)$$

Inserting the expressions for  $p(R)$  (Equation 2.61) and  $m(R)$  (Equation 2.54) into Equation 3.39 and using integration by parts, we have

$$\begin{aligned} P_1 &= -\frac{\pi}{a^2} \int_0^{R_c} R^2 dI \\ &= -\frac{\pi}{a^2} R_c^2 I(R_c) + \frac{2\pi}{a^2} \int_0^{R_c} RI dR. \end{aligned} \quad (3.40)$$

The integration in the second term of Equation (3.40) can be done numerically from the measured nearfield, and the first term can be immediately obtained from the nearfield value at  $R_c$ . The total power  $P_t$  can be obtained in a similar manner by changing the upper limit of the integration to 1 and omitting the first term in Equation (3.40) because  $I(1) = 0$ . The value of  $P_2$ , the power in the higher-order mode packet, can be obtained from

$$P_2 = P_t - P_1. \quad (3.41)$$

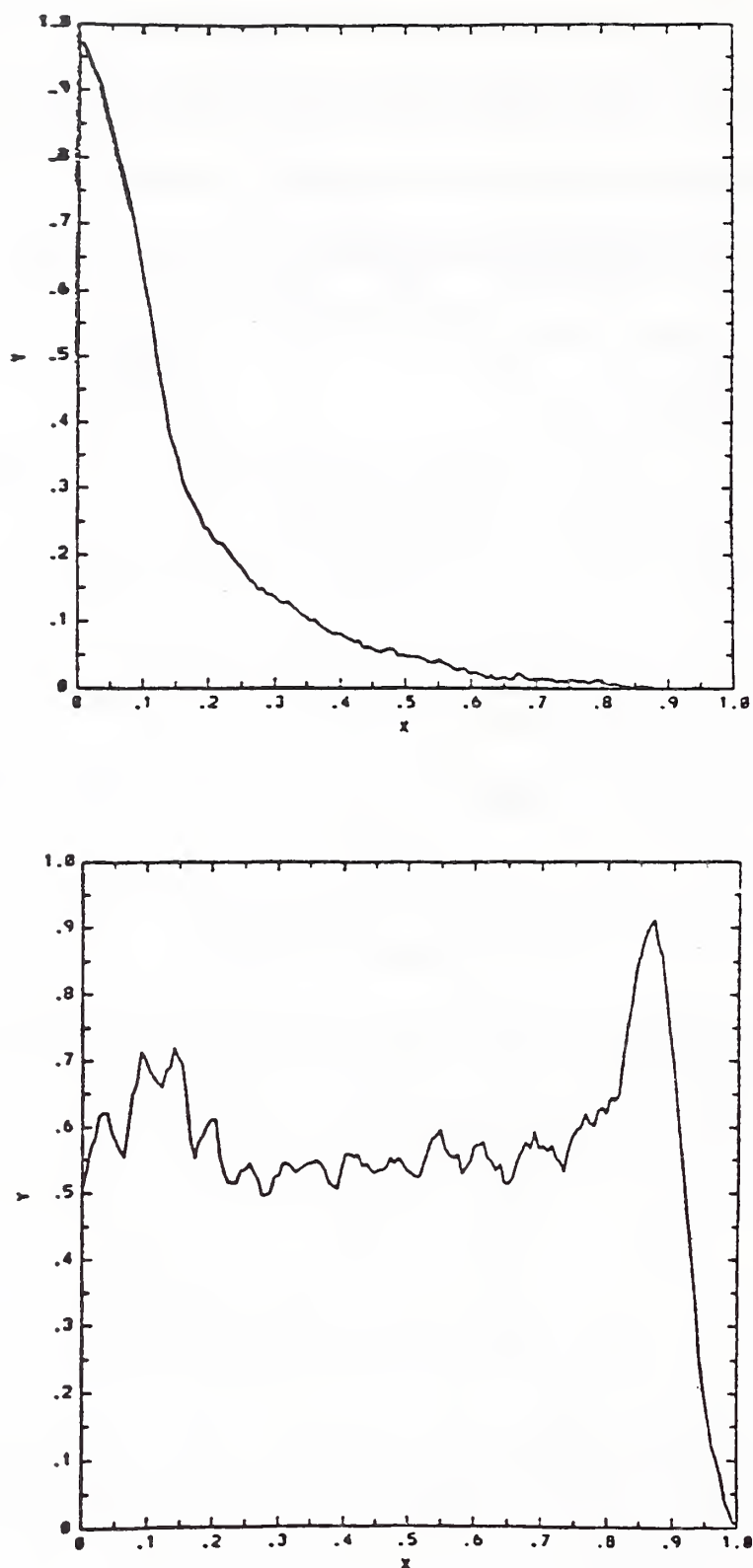


Figure 3.6: Input nearfield patterns of plane wave launch.

This way we have avoided calculating the modal power distribution from the derivatives of the nearfield pattern. The derivatives of the measured nearfield could show very large random oscillations because of the noise in the measurement. The integration in the last equation averages out the effect of the noise. However, the value of  $I(R_c)$  is still affected by the noise. We can do curve fitting in the neighboring section of that point and determine the value of  $I(R_c)$  from the fitted curve. Because the input and output nearfield patterns are normalized, they carry no information of the loss. We have to use the measured loss to modify the values of the elements of one of these vectors relative to the other.

The second method is to curve fit the measured nearfield. Curve fitting can be done using Chebyshev polynomials or other empirical forms [43]. The modal power distribution  $p(R)$  is then obtained by taking the derivative of the fitted curve, and the vector power components are then obtained by Equation (1.20). Empirical curve fitting can obtain a smooth modal power distribution but lacks generality because the form of the curve may not fit for all launch conditions. Chebyshev fitting can be used for all launch conditions, but sometimes unusually sharp changes in the measured nearfield caused by faults in the measurement or in the fiber structure may affect the fitting result. For example, we may get negative values in the modal power distribution. Some modifications might be necessary to improve the fitting accuracy. The modal power distribution needed for the calculation of transfer function is obtained in the same way.

Test components are usually prepared in two ways. One kind of component has long pigtail fibers at both ends, one of which is usually longer than

the other. These components are used for the cut-back method. Other components are connectorized at both ends and are used for the dummy input method. The measurement procedures for these two kinds of measurements are described as follows.

#### Cut-back method:

The test component is placed in the measurement setup. The longer fiber end is used as the input end. The input light is focused onto the center of the input fiber. The output end is focused onto the CCD camera through the beamsplitter. The nearfield pattern and output power are then measured. They are the output nearfield and power of the component for the first excitation. Then the input pigtail fiber is cut about one or two meters from the input end. The test component is taken out and the output end of the remaining short piece of fiber is focused onto the CCD camera through the beamsplitter. The nearfield pattern and power output are then measured. They are the input nearfield and power of the test component for the first excitation. The launch condition is then changed to the second excitation and the above steps are repeated to obtain the output and input nearfield patterns and power values for the second excitation. The length of the short piece of fiber cut from the component is usually 2m long for overfilled and off-central excitations and 1m long for central excitation. The 2m length is sufficient for the leaky modes excited in these two launches to dissipate.

#### Dummy input method:

Two pieces of short fiber about 2m long and connectorized at one end are used for this method of measurement. They are used as the input and output connectors. First we connect the input and output connectors.

The loose fiber ends are placed onto the input and output stages. The light is focused onto the input end, and the output end is focused onto the CCD camera through the beamsplitter. The nearfield pattern and the power output are measured. These are the input nearfield pattern and power of the first excitation. The input and output connectors are then disconnected and the test components inserted. The connector at the input end of the component is connected to the input connector and the connector at the output end is connected to the output connector. The nearfield pattern and the power are measured. These are the output nearfield and power of the first excitation. The launch condition is then changed to the second excitation. The nearfield pattern and power, which are the output nearfield pattern and power of the second excitation are then measured. The test component is then disconnected from the input and output connectors and the input and output connectors reconnected. The input nearfield and power of the second excitation are then measured.

The cut-back method is usually more accurate than the dummy input method because the dummy input is not the true input. However, the cut-back method is destructive to the component because the input pigtail fiber will become shorter and shorter with repeated measurements.

### 3.7 Round-Robin Test and Experimental Results

As was mentioned in Section 3.2, the TIA Subcommittee on Fiber Optic Measurements has discussed using the mode transfer matrix as a possible standard method for the characterization of optical fiber devices and systems. It is the desire of the TIA to test the repeatability of measured matrices obtained by different laboratories. Our purpose is to direct this exercise for the

TIA and simultaneously test the premise that the measured matrix is a complex mixture of the matrices corresponding to the two excitations. So, in collaboration with TIA and the NIST, we conducted a round-robin measurement test. Four laboratories participated in the round-robin. No mandatory launch conditions were stipulated; that is, the participants used whatever excitations they normally use in their laboratories. This provided us with a good variety of excitations for the measurement of the same component. Three participants used more or less the same kind of measurement setup described in the first part of the last section, whereas the fourth participant used the plane wave launch.

Artifacts for the round-robin test include connectors which have pigtailed fibers at both ends, short pieces of fiber which are about 2m long and connectorized at both ends, two long pieces of cable about two hundred meters long, of which one is connectorized at both ends, and two power splitters which are connectorized at the input and output ports. Not all the participants measured all the test artifacts. Results will be presented here of those artifacts that were measured by most of the participants; thus a comparison can be made and meaningful statistical results be calculated. Results presented here are of these components:

- ccl: a short piece of fiber connectorized at both ends;
- ccml: a connector with pigtailed fibers at both ends;
- cpml: a connector with pigtailed fibers at both ends;
- canc: a piece of cable about 200 m long;
- caec: a piece of cable about 200 m long connectorized at both ends;
- psg: a power splitter connectorized at all the input and output ports.

Participants are named as P1, P2, P3, and P4, respectively, in the presentation of the results. Participant P1 made four or five measurements on most of the components, so it is possible to compare the statistics of measurements made by one participant using the same launch condition and that by participants using different launch conditions.

The input modal power distributions used by the participants are shown in Figures 3.7 to 3.10. These modal power distributions show that we have a good variety of launch conditions. Modal power distributions used by participant P4 are especially different from those of the other participants because it used the plane wave launch.

Details of the measured matrices of cable canc, connector ccml and power splitter psg are listed in Tables 3.3 to 3.8. Matrices of each of these components measured by participant P1 are listed in Tables 3.3, 3.5, and 3.7 and those measured by different participants are listed in Tables 3.4, 3.6, and 3.8. Average values and standard deviations are calculated and listed at the bottom of each table. That the standard deviation of matrix elements measured made by participant P1 is significantly lower than that by different participants. This fact is summarized in Table 3.9, where standard deviations of seven components (the two output ports of a power splitter are listed as two components) are listed. The large differences between these two standard deviations convincingly shows that the measured transfer matrix is seriously dependent on modal power distribution. Also, for most of the components listed, the matrices made by P4 are more different from those of the others, a fact which strengthens the above conclusion because the launch condition used by P4 is the most different from the others.

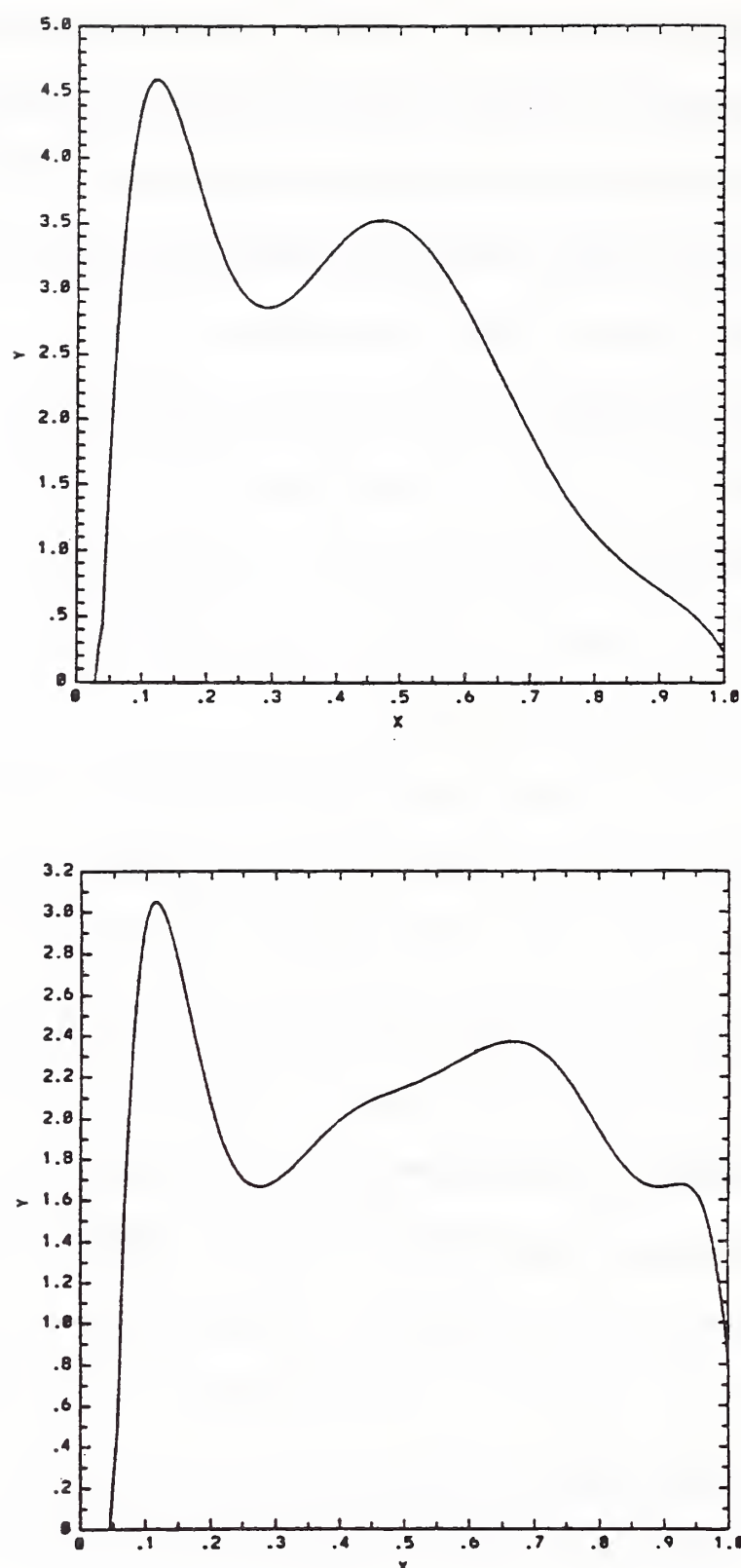


Figure 3.7: Input modal power distributions used by P1.

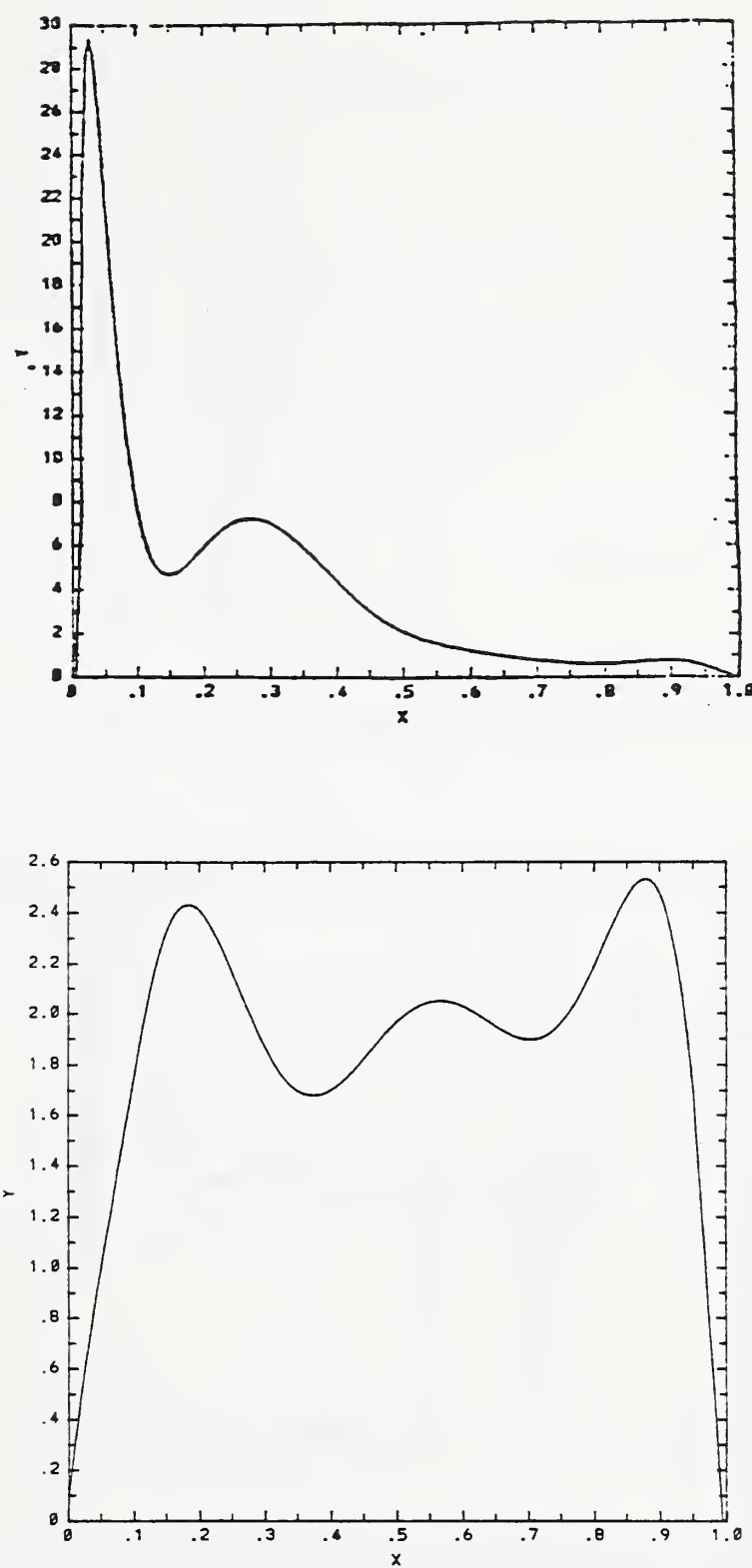


Figure 3.8: Input modal power distributions used by P2.

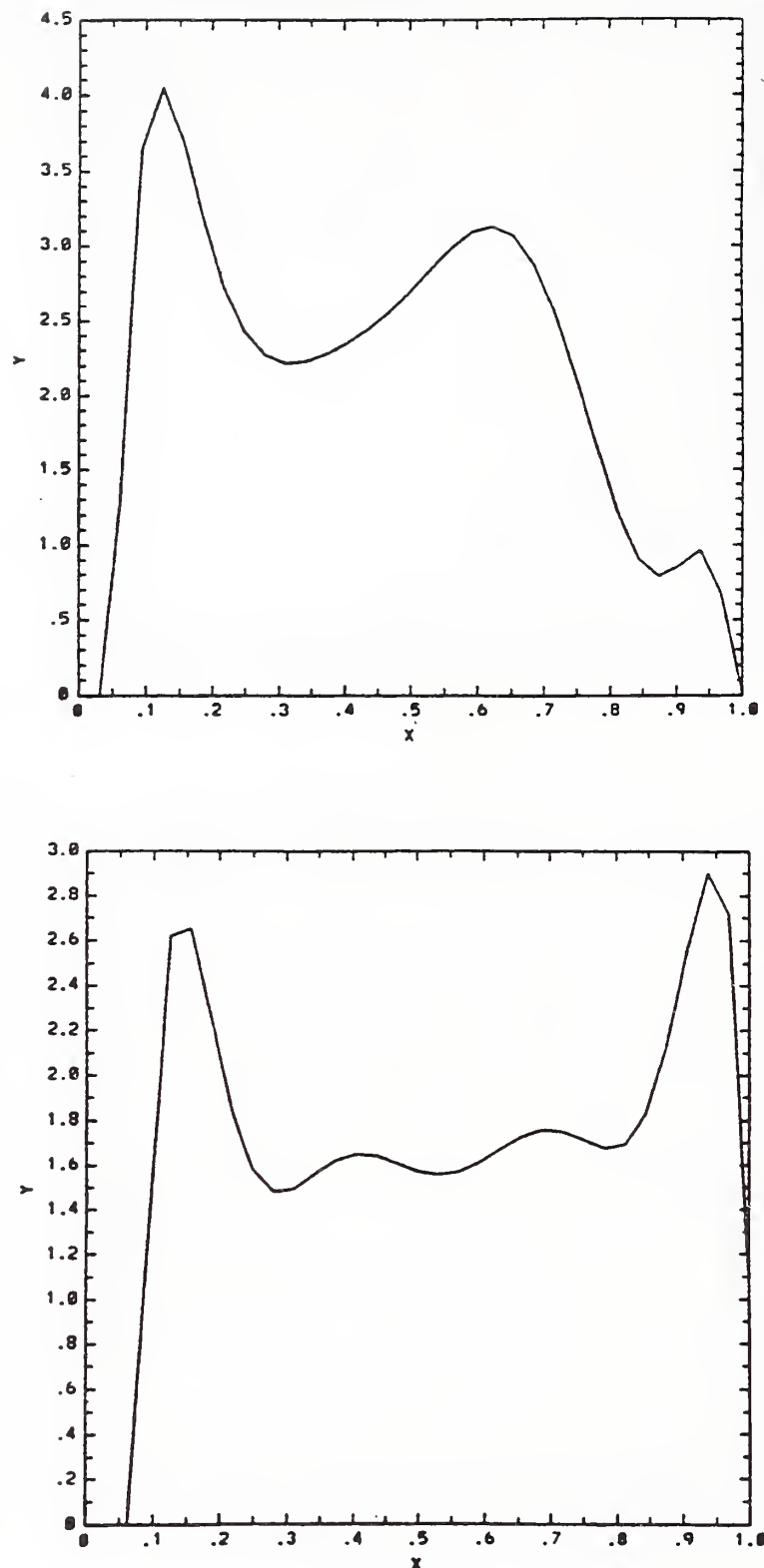


Figure 3.9: Input modal power distributions used by P3.

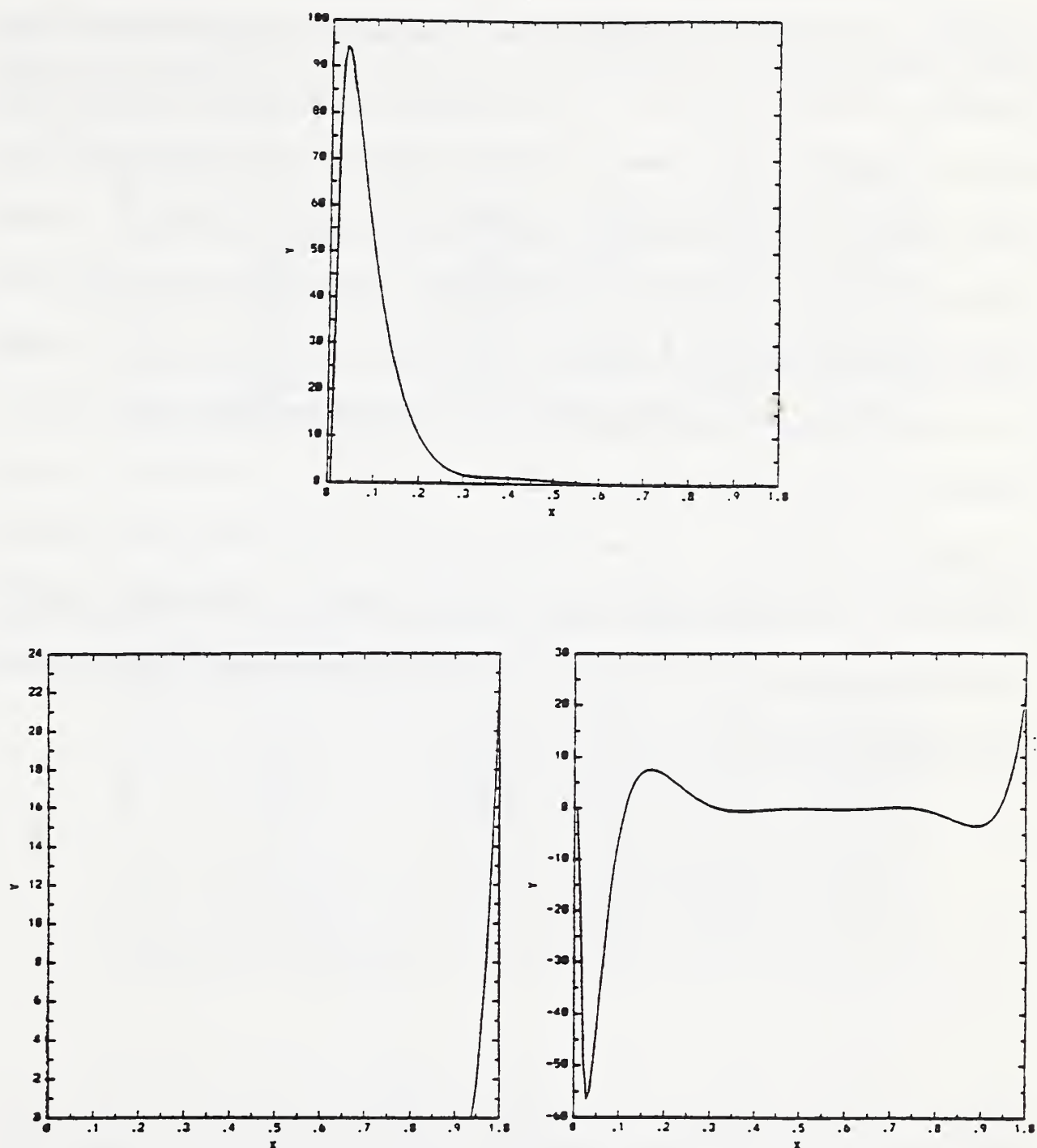


Figure 3.10. Input modal power distributions used by P4, who used plane wave launch. (a) is low-order mode launch; (b) is high-order mode launch; and (c) is generalized modal power distribution for high-order mode launch.

Besides the launch conditions, causes for the deviation of the measured matrices include the imperfections in the fibers, measurement error, and error due to data processing. Almost all the participants used Chebyshev fitting to obtain the modal power distribution from the measured nearfield pattern. However, they used different order of Chebyshev polynomial. In order to show the effect of different data processing, Table 3.10 lists the matrices of four components calculated from the same raw measured data yet processed by two participants using three different processing methods. Participant P1 processed the data twice using two different programs, one of which is written by another participant. Comparing the average standard deviations listed at the bottom of this table with those listed in Table 3.9, we conclude that the standard deviations due to different measurement and different data processing are roughly the same.

Table 3.3. Measured transfer matrices of cable canc. Three measurements were made by participant P1 using the same launch conditions.

	$t_{11}$	$t_{12}$	$t_{21}$	$t_{22}$
P1-1	0.8852	0.0200	0.0187	0.7056
P1-2	0.8510	0.0670	0.0496	0.6703
P1-3	0.8463	0.0597	0.0543	0.6638
Average	0.8608	0.0489	0.0409	0.6799
Standard Deviation	0.0212	0.0253	0.0193	0.0225

Table 3.4. Comparison of measured transfer matrices of cable canc. Measurements were made by four participants using different launch conditions. Data of P1 are the average values in Table 3.3.

	$t_{11}$	$t_{12}$	$t_{21}$	$t_{22}$
P1	0.8608	0.0489	0.0409	0.6799
P2	1.1385	-0.2729	-0.0472	0.7037
P3	0.9635	0.0487	0.0702	0.5871
P4	0.6910	0.1214	0.2117	0.3470
Average	0.9134	-0.0135	0.0689	0.5794
Standard Deviation	0.1874	0.1763	0.1075	0.1629

Table 3.5. Measured transfer matrices of connector ccm1. Four measurements were made by participant P1 using the same launch condition.

	$t_{11}$	$t_{12}$	$t_{21}$	$t_{22}$
P1-1	0.8810	-0.0169	0.1012	0.6336
P1-2	0.8818	0.0212	0.0913	0.6354
P1-3	0.8778	0.0439	0.0912	0.6615
P1-4	0.9184	-0.0188	0.0717	0.6842
Average	0.8897	0.0073	0.0888	0.6537
Standard Deviation	0.0192	0.0305	0.0124	0.0240

Table 3.6. Comparison of measured transfer matrices of connector ccm1. Measurements were made by different participants using different launch conditions. Data for P1 are the average values in Table 3.5.

	$t_{11}$	$t_{12}$	$t_{21}$	$t_{22}$
P1	0.8897	0.0073	0.0888	0.6537
P2	0.9380	0.0779	0.1519	0.4414
P3	0.8357	0.1087	0.1426	0.4120
P4	0.5715	0.1951	0.1526	0.3222
Average	0.8087	0.0972	0.1340	0.4573
Standard Deviation	0.1635	0.0778	0.0305	0.1404

Table 3.7. Measured transfer matrices of power splitter psg. Five measurements were made by participant P1 using the same launch condition.

Port 1	$t_{11}$	$t_{12}$	$t_{21}$	$t_{22}$
P1-1	0.4022	0.0227	0.0371	0.3060
P1-2	0.4059	0.0312	0.0371	0.3183
P1-3	0.4120	0.0284	0.0304	0.3231
P1-4	0.4300	0.0538	0.0289	0.3636
p1-5	0.4250	0.0145	0.0291	0.3488
Average	0.4150	0.0301	0.0325	0.3320
Standard Deviation	0.0120	0.0147	0.0042	0.0236
Port 2	$t_{11}$	$t_{12}$	$t_{21}$	$t_{22}$
P1-1	0.4796	0.0372	0.0363	0.3393
P1-2	0.4586	0.0548	0.0271	0.3705
P1-3	0.4491	0.0517	0.0463	0.3197
P1-4	0.4784	0.0328	0.0308	0.3772
p1-5	0.4765	0.0186	0.0305	0.3499
Average	0.4684	0.0390	0.0342	0.3513
Standard Deviation	0.0138	0.0147	0.0075	0.0234

Table 3.8. Measured transfer matrices of power splitter psg. Measurements were made by three participants using different launch conditions. Data of P1 are the average values in Table 3.7.

Port 1	$t_{11}$	$t_{12}$	$t_{21}$	$t_{22}$
P1	0.4150	0.0301	0.0325	0.3320
P2	0.5762	-0.0640	0.0033	0.2951
P4	0.3689	0.0883	0.0936	0.2766
Average	0.4534	0.0181	0.0431	0.3012
Standard Deviation	0.1088	0.0768	0.0461	0.0282
Port 2	$t_{11}$	$t_{12}$	$t_{21}$	$t_{22}$
P1	0.4684	0.0390	0.0342	0.3513
P2	0.5157	0.0030	0.0129	0.3313
P4	0.3675	0.0894	0.0981	0.2788
Average	0.4505	0.0438	0.0484	0.3205
Standard Deviation	0.0757	0.0434	0.0443	0.0374

Table 3.9. Comparison of standard deviations of measured matrices made by participant P1 using the same launch condition and by different participants using different launch conditions.

component		$t_{11}$	$t_{12}$	$t_{21}$	$t_{22}$
ccm1	SD-P1	0.0192	0.0305	0.0124	0.0240
	SD-All	0.1636	0.0778	0.0305	0.1404
cpml	SD-P1	0.0071	0.0409	0.0094	0.0159
	SD-All	0.1082	0.1039	0.0196	0.1337
ccl	SD-P1	0.0275	0.0261	0.0132	0.0542
	SD-All	0.0941	0.0492	0.0509	0.0896
canc	SD-P1	0.0212	0.0253	0.0193	0.0225
	SD-All	0.1404	0.1857	0.0611	0.0616
caec	SD-P1	0.0037	0.0471	0.0141	0.0078
	SD-All	0.1176	0.0665	0.1172	0.1551
psg port 1	SD-P1	0.0120	0.0147	0.0042	0.0236
	SD-All	0.1088	0.0768	0.0461	0.0282
psg port 2	SD-P1	0.0138	0.0147	0.0075	0.0234
	SD-All	0.0757	0.0434	0.0443	0.0374
Average	SD-P1	0.0149	0.0285	0.0114	0.0245
	SD-All	0.1155	0.0861	0.0528	0.0922

Table 3.10. Average values of measured transfer matrices of four components. Averages are taken on four or five measurement results. Results are calculated by two participants using three different data processing methods. The average values and standard deviations of the results of the three methods are then calculated and also listed in this table. Listed at the bottom of this table are the average values of the standard deviations of the four components. This average represents the uncertainty due to data processing methods.

ccl	$t_{11}$	$t_{12}$	$t_{21}$	$t_{22}$
P1-1	0.765	0.013	0.076	0.740
P1-2	0.7939	0.0290	0.0400	0.7138
P2	0.7900	0.0334	0.0352	0.6985
Average	0.7830	0.0251	0.0504	0.7174
Standard Deviation	0.0157	0.0107	0.0233	0.0210
caec	$t_{11}$	$t_{12}$	$t_{21}$	$t_{22}$
P1-1	0.826	0.023	0.058	0.808
P1-2	0.8801	0.0242	0.0218	0.7708
P2	0.8989	0.0435	0.0109	0.7742
Average	0.8683	0.0302	0.0302	0.7843
Standard Deviation	0.0378	0.0115	0.0246	0.0206
port 1 of psg	$t_{11}$	$t_{12}$	$t_{21}$	$t_{22}$
P1-1	0.394	0.017	0.070	0.374
P1-2	0.4082	0.0324	0.0396	0.3323
P2	0.4150	0.0301	0.0325	0.3320
Average	0.4057	0.0265	0.0474	0.3461
Standard Deviation	0.0107	0.0083	0.0199	0.0242
port 2 of psg	$t_{11}$	$t_{12}$	$t_{21}$	$t_{22}$
P1-1	0.452	0.031	0.077	0.392
P1-2	0.4645	0.0405	0.0413	0.3436
P2	0.4684	0.0390	0.0342	0.3513
Average	0.4616	0.0368	0.0508	0.3623
Standard Deviation	0.0086	0.0051	0.0229	0.0260
Average of Standard Deviation	0.0182	0.0083	0.0199	0.0242

## CHAPTER 4

### COUPLING MECHANISMS AND TRANSFER FUNCTIONS

#### 4.1 Introduction

In this chapter, we will discuss the basic power coupling processes occurring in fiber-optic devices and derive the mode transfer functions corresponding to these coupling mechanisms. Two coupling mechanisms can cause modal power transfer in fiber-optic devices: scattering and geometrical transition of a ray.

Scattering can occur when light passes through a medium. Whenever there are discrete variations in the refractive index due to the presence of particles or because of small scale density fluctuations, part of the radiation will be scattered in all directions [52]. Scattering in optical fibers can also be caused by irregularities of fiber geometry and index inhomogeneities, stress, and microbending, etc. [53]. Scattering coupling in optical fibers has been discussed extensively in the literature [20, 21, 54, 55], though it is oftentimes called coupling. It is the coupling referred to by Marcuse when he discusses coupled mode equations and coupled power equations [20]. In the coupled mode equation,

$$\frac{\partial a_\nu}{\partial z} = \sum_{\mu=1}^N C_{\nu\mu} a_\mu, \quad (4.1)$$

where  $a_\nu (\nu = 1, 2, \dots)$  and  $C_{\nu\mu}$  denote the amplitude of the  $\nu$ th mode and the conversion coefficient from the  $\mu$ th to the  $\nu$ th mode, respectively. The

amplitude coupling coefficients are complex-valued and satisfy

$$\begin{aligned} C_{\nu\mu}^* &= -C_{\mu\nu}, \\ C_{\nu\nu} &= -j\beta_\nu. \end{aligned} \quad (4.2)$$

The solution of the coupled mode equation gives the amplitude and phase of each mode as a function of position along a fiber section. However, this information is generally unnecessary and, due to the randomness of the fluctuations that cause the coupling, it is impossible to determine the phase difference between modes along the fiber length. In addition, the use of incoherent sources for multimode fiber excitation in practical cases leads to excitation of a continuum of modes (Section 2.3), so the phase information is averaged out. Marcuse, therefore, proceeds to derive the coupled power equations [56], which take the form

$$dP_\mu/dz = -2\alpha_\mu P_\mu + \sum_{\nu=1}^N h_{\nu\mu}(P_\nu - P_\mu). \quad (4.3)$$

The coupled power equations have the simple meaning that the variation of power in mode  $\mu$  equals the total power coupled from other modes into this mode minus the total power coupled out of this mode to other modes. The first term on the right is the differential mode loss. Our derivation of the transfer function for scattering coupling in Section 4.2 is based upon the same assumption, but in the mode continuum limit and for a case where the coupling coefficients have a specific expression which is derived from analysis of the physical processes that cause scattering.

Total power coupling due to the geometrical offset of two fibers was studied by Gloge [29] and Di Vita et al. [57]. Although in his calculation, Gloge used for the first time the concept of modal power distribution  $p(R)$ , details of modal power conversion due to geometrical offset have never been

studied. In devices comprising two pieces of fiber such as splices and connectors, geometrical offset between the two fibers is unavoidable. When a ray of a certain mode exits a first fiber and enters a second, it may enter a different ray path in the second fiber relative to the ray path in the first fiber. We call this kind of coupling overlap coupling, because it is caused by the overlap of the two rays in the spatial position at the crossing plane. Evidently, the transfer function for overlap coupling would be quite different from that for scattering coupling, and it will be derived in Section 4.3.

## 4.2 Transfer Function for Scattering Coupling

For discrete modes, it is assumed that mode coupling takes place between adjacent modes [20, 21, 58]. This assumption is based on an experiment of Gloge [59], who found that the power in a mode moved gradually to neighboring modes along the fiber length. With this assumption, the coupled power equation can be rewritten as [21]

$$m \frac{dP_m}{dz} = -m\alpha_m P_m + md_m(P_{m+1} - P_m) + (m-1)d_{m-1}(P_{m-1} - P_m). \quad (4.4)$$

This equation was represented in matrix form in Reference [44], where good experimental results were obtained with overfilled excitation. In the mode continuum limit, the assumption of adjacent mode coupling can be generalized so that the scattering coupling operator is proportional to a Gaussian function of the mode difference. This assumption is plausible because a great amount of random factors contribute to the coupling, so the central limit theorem applies. The scattering coupling function then takes the form

$$\alpha(R, R') = \alpha_0 e^{-|R^2 - R'^2|/\tau} K(R, R'), \quad (4.5)$$

where  $\alpha_0$  is a parameter used to determine the amount of scattering and  $K(R, R')$  is a factor representing mode-dependent effects. The cause of these effects can be described as follows. Because scattering alters only the ray's propagation direction and not its position, this can be represented in phase space by a vertical line that runs through the point representing the mode at the place where scattering takes place (Figure 4.1). It can be assumed that scattering coupling between modes  $R'$  and  $R$  is proportional to  $[\min(R, R')]^2$ , that is, proportional to the common area traversed by the two modes. Since mode  $R'$ , from which power is coupled out, traverses an area proportional to  $R'^2$ , the relative scattering coupling is then  $[\min(R, R')]^2/R'^2$  (Figure 4.2). Rayleigh scattering is always present in the medium and the scattered power is proportional to the density of the medium. Since refractive index, or the dopant concentration, is higher in the center than at the edge of the fiber, Rayleigh scattering will be stronger in the center than at the edge [20, 21, 60]. Conversely, stress and deformation caused by external forces will be greater at the edge than in the center and would cause the extraneously induced scattering to be greater at the edge than in the center.

These last two facts suggest that scattering coupling coefficient is proportional to  $(1 - R'^x + R'^y)$ , where  $x$  and  $y$  determine the shape of the variation with the mode parameter. Using this assumption, we write that

$$K(R, R') = \frac{[\min(R, R')]^2}{R'^2} (1 - R'^x + R'^y). \quad (4.6)$$

Scattering coupling takes place along the propagation path. The variation of power per unit length in a particular mode  $R$  at position  $z$  must be equal to the total power coupled into this mode from all the guided modes minus the total amount of power coupled out of this mode to all other modes

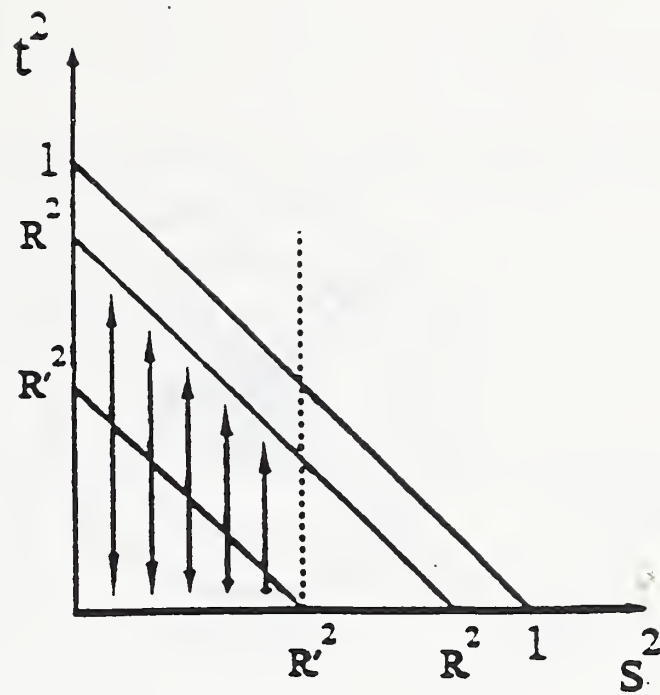


Figure 4.1: Phase space diagram of scattering coupling.

guided or radiated. These effects can be expressed in the form

$$\begin{aligned} \frac{dP(R, z)}{dz} &= \int_0^1 \alpha(R, R') P(R', z) dR' \\ &- \int_0^\infty \alpha(R'', R) P(R, z) dR''. \end{aligned} \quad (4.7)$$

The first term on the right side of Equation (4.7) represents the amount of power coupled into mode  $R$  from all the guided modes, which have mode parameter in the range from 0 to 1. The second term represents the total amount of power coupled out of mode  $R$  into all the guided or radiated modes, the latter having mode parameters from 1 to  $\infty$ . Marcuse's coupled power equation (Equation 4.3) contains a differential mode attenuation term, which is not included in Equation (4.7). There are two reasons. First, present high quality fibers have very low absorption loss, which is the sole major source of differential mode attenuation. Rayleigh scattering loss is the dominant loss mechanism and is manifested in the typical spectral loss behavior of a fiber (Figure 4.3). If a fiber had a high absorption loss, we would observe a significant

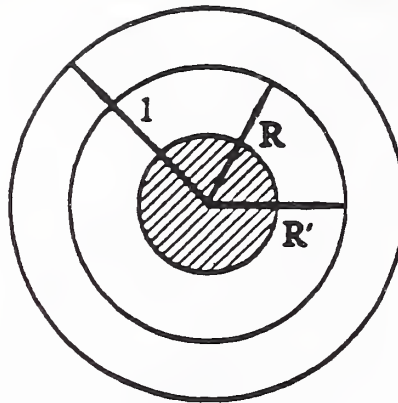


Figure 4.2. Common area traversed by two mode groups involved in the scattering coupling.

difference between the measured loss and the loss calculated from the transfer function. Further, for usual devices, absorption loss is negligible because only very short pieces of fibers are used for pigtailing those devices. In a device, extrinsic scattering could be stronger than Rayleigh scattering. As a result of these considerations, in general, absorption loss can be ignored. The first-order solution to Equation (4.7) is then

$$\begin{aligned} P(R; z) &= P(R; 0) - P(R; 0)z \int_0^\infty \alpha(R'', R)dR'' \\ &+ z \int_0^1 \alpha(R, R')P(R'; 0)dR'. \end{aligned} \quad (4.8)$$

Rewriting the definition of the transfer function of Equation 3.11, which is  $z$  independent, in a  $z$ -dependent form,

$$P(R; z) = \int_0^1 P(R'; 0)T(R, R'; z)dR', \quad (4.9)$$

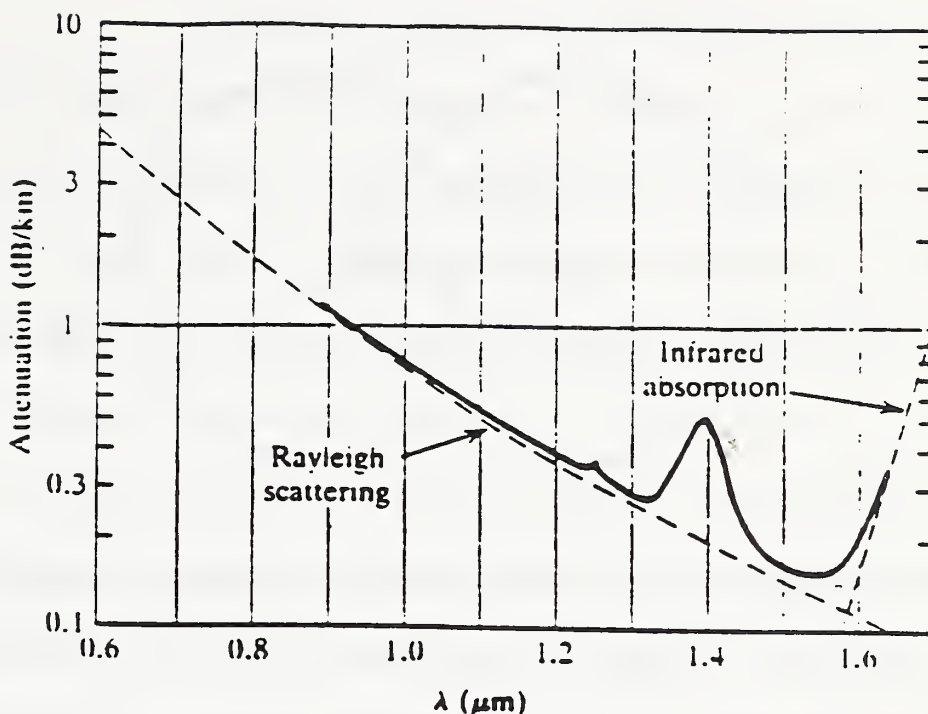


Figure 4.3: Loss spectrum of a typical high quality fiber.

we find the following expression for the transfer function for scattering coupling

$$T(R, R'; z) = [1 - \int_0^\infty z\alpha(R'', R')dR'']\delta(R' - R) + z\alpha(R, R'). \quad (4.10)$$

In the first-order solution, parameters  $\alpha_0$  and  $z$  always appear as a product, so  $\alpha_0 z$  can be treated as one parameter. In a piece of fiber or cable, scattering coupling is the sole coupling mechanism. If the fiber is of high quality and in an almost stress free state, the scattering per length should be small. This will be manifested in a relatively small value of  $\alpha_0 z$ . Only when such a fiber is very long does  $\alpha_0 z$  take on a significant value. In devices like power splitters, where short pieces of fiber are severely twisted and deformed, scattering will be very strong and  $\alpha_0 z$  will be large in spite of the small value of  $z$ . These effects will be illustrated in experimental results to be presented in Chapter 5. At this moment, I have no idea how the internal and external

physical conditions of the devices will affect the other parameters.

### 4.3 Transfer Function for Overlap Coupling

Overlap coupling is caused by geometrical offset of the fiber ends in devices consisting of two pieces of fibers. Connectors, splices, and power splitters are such devices. Butt coupling is a typical case of overlap coupling. There are three kinds of geometrical offset: lateral shift, longitudinal shift, and tilt. From the relation  $R^2 = s^2 + t^2$ , we see that  $R$  is symmetrical in  $s$  and  $t$ , the normalized radial position and the normalized numerical aperture of the ray. This implies that lateral shift and tilt will have similar effects on modal power conversion. The effect of longitudinal offset is less than lateral shift and tilt; this will be shown in the last part of this section. We will, therefore, start with the discussion of lateral shift.

Figure 4.4 illustrates the change of the radial position of a ray exiting a fiber at  $r'$  and entering a second fiber at  $r$ . The coordinate  $r$  can be related to  $r'$  by

$$r^2 = r'^2 + d^2 + 2r'd \cos \psi, \quad (4.11)$$

where  $d$  is the lateral shift of the two fibers, that is, the distance between the centers of the two fibers;  $\psi$  is the angle the radial  $r'$  makes with the line connecting the two centers.

From Equation (4.11), we derive

$$R^2 = R'^2 + l^2 + 2s'l \cos \psi \quad (4.12)$$

for the magnitude of the shift in mode number from the first to the second fiber, where  $R'$  is the mode parameter of the ray in the first fiber and  $R$  the mode parameter it takes when entering the second fiber,  $s = r/a$  is the normalized

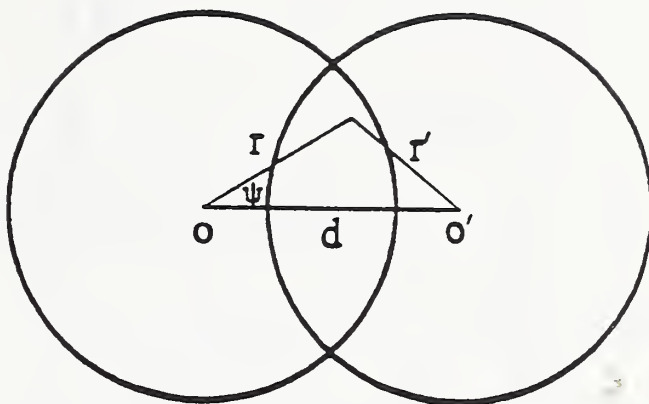
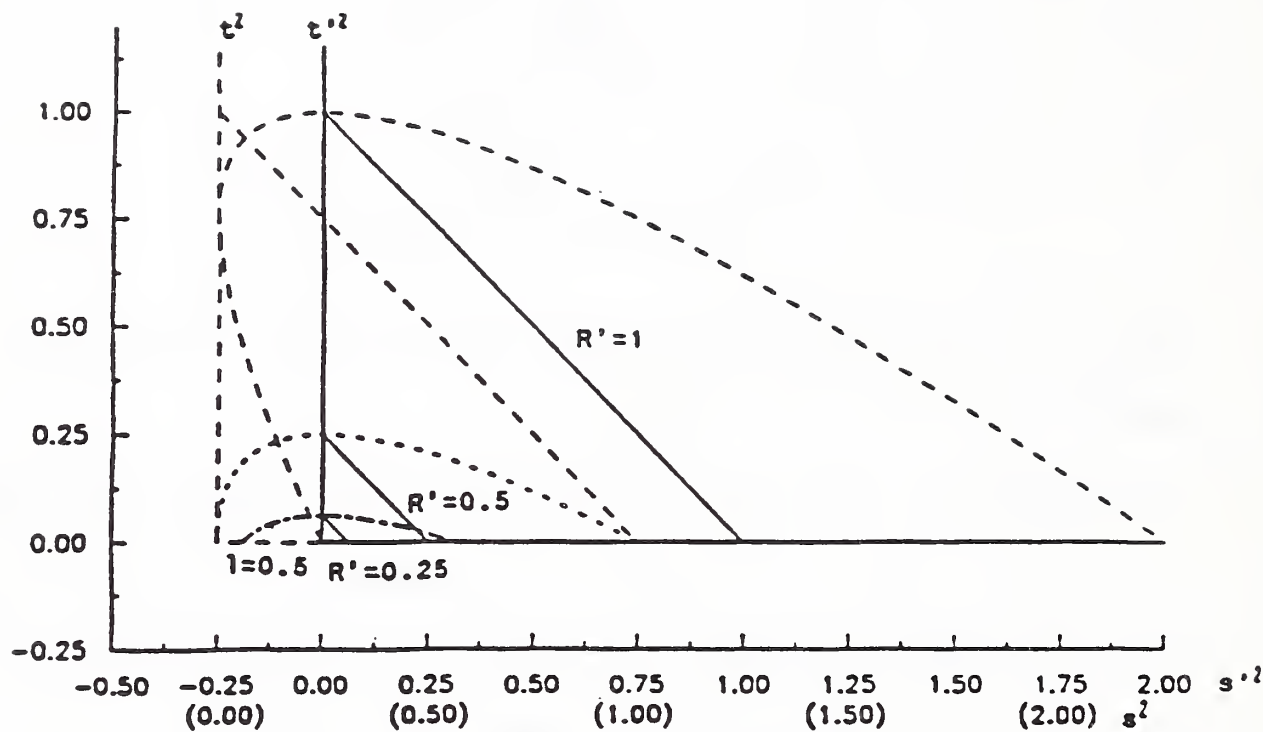


Figure 4.4. Change of radial position of a ray crossing two fibers having lateral displacement.

position, and  $l = d/a$  the normalized shift. A ray exiting the first fiber and entering the second will experience a slight change of refractive index due to the lateral shift of the fiber ends. Typical index difference between the core and the cladding of the fiber is 1 to 2%. Thus a 100% relative shift, that is,  $l = 1$ , will cause 1 to 2% change of index profile, which will in turn result in a similar variation of the ray's propagation angle and the value of  $t$ . This variation of  $t$  can be ignored compared to the 100% variation of  $s$ . When the relative shift is less than 100%, the change of the propagation angle and  $t$  will correspondingly become less and still can be ignored.

This mode transition relation is illustrated in the phase space diagram of Figure 4.5, where the two sets of phase space coordinates representing the two fibers are plotted. The first set of coordinates  $s'^2 - t'^2$  is represented by the solid lines and the second set  $s^2 - t^2$  by the dashed lines. The other solid or dashed curves represent the spread of coordinates in the first and second fibers accordingly. Power in mode  $R'$  of the first fiber lying on a solid line will



$$s = \frac{r}{a}$$

$$t = \frac{\sin \theta}{NA}$$

Figure 4.5. Power spreading of a mode in one fiber into other modes in the second fiber due to lateral displacement.

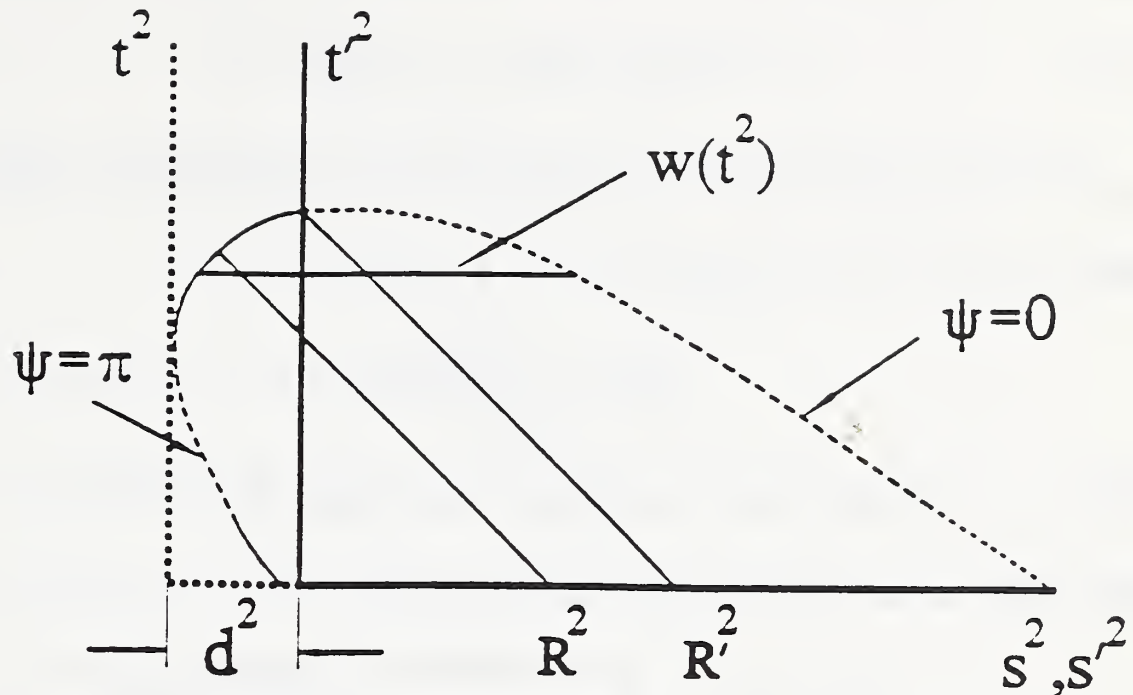


Figure 4.6. Illustration of calculation of power transfer from mode group  $R'$  to mode group  $R$ .

couple into the modes of the second fiber which are located in an area below the corresponding dashed curve shown in the figure. The transfer function due to overlap coupling can be derived from this picture.

Consider power coupling between mode group  $R'$  in the first fiber and mode group  $R$  in the second fiber (Figure 4.6). Total power along the line  $R^2$  under the spread curve is the power coupled from mode group  $R'$  to mode group  $R$ . Though the power distribution is uniform along  $R'^2$ , the power distribution along  $R^2$  is not uniform. This is because power at different points on  $R'^2$  spreads to different numbers of mode groups in the second fiber. Since a ray does not change its propagation direction, that is, its angle with the optical axis of the fiber, in its transition between the fibers, power spread is

along the horizontal line across a certain point on  $R'^2$ . The width within the spread curve on this horizontal line is  $w(t^2)$

$$w(t^2) = R_{\psi=0}^2 - R_{\psi=\pi}^2 = 4l\sqrt{R'^2 - t^2}. \quad (4.13)$$

Power at that point on  $R'^2$  is proportional to the power density  $p(R'^2)$ ; thus power intensity along  $R^2$  at  $t^2$  is

$$I(t^2) = \frac{C p(R'^2)}{4l\sqrt{R'^2 - t^2}}. \quad (4.14)$$

We denote the total power coupled from mode group  $R'^2$  to mode group  $R^2$  by  $P(R^2, R'^2)$ , which is the integral of  $I(t^2)$  over  $t^2$ :

$$\begin{aligned} P(R^2, R'^2) &= \int_0^{R'^2 - (\frac{R^2 - R'^2 - l^2}{2l})^2} \frac{C p(R'^2)}{4l\sqrt{R'^2 - t^2}} dt^2 \\ &= \frac{C p(R'^2)}{2l} \left( R' - \left| \frac{R^2 - R'^2 - l^2}{2l} \right| \right). \end{aligned} \quad (4.15)$$

The upper limit in Equation (4.15) is determined from Equation (4.12) by taking  $\psi = 0$  or  $\pi$ . The proportionality factor  $C$  can be determined from the relation of power conservation; that is, the total power beneath the curve must equal the total power in mode group  $R'^2$ :

$$\int_{R_{min}^2}^{R_{max}^2} P(R^2, R'^2) dR^2 = p(R'^2) R'^2, \quad (4.16)$$

where  $R_{min}$  and  $R_{max}$  denote the minimum and maximum order of mode groups of the second fiber that have power coupled into them from mode group  $R'$  of the first fiber and are determined at  $\psi = 0$  or  $\pi$  and  $t = 0$ :

$$\begin{aligned} R_{min}^2 &= (R' - l)^2, \\ R_{max}^2 &= (R' + l)^2. \end{aligned} \quad (4.17)$$

Equation (4.16) yields  $C = 1$ .

The total power coupled from the first fiber into mode group  $R^2$  in the second fiber can be expressed as

$$P(R^2) = \int_0^1 P(R^2, R'^2) dR'^2. \quad (4.18)$$

Inserting the relation  $P(R^2) = p(R^2)R^2$  into the above equation, we have

$$P(R^2)R^2 = \int_0^1 P(R^2, R'^2) dR'^2. \quad (4.19)$$

Inserting Equation (4.15) into (4.19), we obtain

$$p(R)R^3 = \int_0^1 \frac{R}{lR'^2} \left( R' - \left| \frac{R^2 - R'^2 - l^2}{2l} \right| \right) p(R') R'^3 dR'. \quad (4.20)$$

Comparing Equation (4.20) with the definition of transfer function of Equation 3.11, we finally get the overlap transfer function:

$$T_{ol}(R, R') = \begin{cases} \frac{R}{lR'^2} \left( R' - \left| \frac{R^2 - R'^2 - l^2}{2l} \right| \right), & \text{if } |R - l| < R' < \min(1, R + l), \\ 0, & \text{otherwise.} \end{cases} \quad (4.21)$$

When  $l$  approaches zero,  $T_{ol}(R, R')$  will become a  $\delta$ -function since the integration area in Equation (4.20) will shrink to zero.

As was stated earlier in this section, tilt will have a similar effect to lateral shift. The discussion above can be generalized to include the effect of tilt. We can define  $l$  as the combined relative offset:

$$l^2 = \frac{d^2}{a^2} + \frac{\sin \theta^2}{(NA)^2}. \quad (4.22)$$

Thus all the above expressions and discussions about lateral shift apply to tilt also.

The variation of radial position of a ray due to longitudinal offset is illustrated in Figure 4.7 and can be expressed as

$$r^2 = r'^2 + d^2 \tan^2 \theta + 2r'd \tan \theta \cos \psi. \quad (4.23)$$

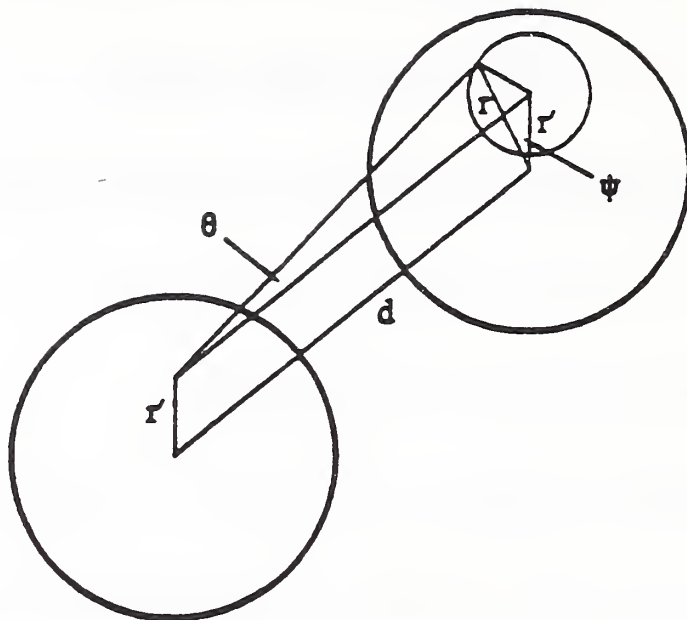


Figure 4.7. Variation of the radial position of a ray due to longitudinal displacement of the ends of two fibers.

Remembering that  $\theta$  is small, we can replace  $\tan \theta$  by  $\sin \theta$ , which equals  $t(NA)$ .

We then obtain the mode conversion relation

$$R^2 = R'^2 + 2s'l t(NA) \cos \psi + l^2 t^2 (NA)^2. \quad (4.24)$$

Since  $(NA) \simeq 0.2$  and for a practical device we can assume that  $l$  is no more than 0.4 (which corresponds to a longitudinal displacement of  $10 \mu\text{m}$  for a  $50 \mu\text{m}$  diameter fiber) and  $t < 1$ , the last term on the right side of Equation (4.24) can be safely ignored and the equation becomes

$$R^2 = R'^2 + 2s'l t(NA) \cos \psi. \quad (4.25)$$

The mode conversion area in the phase space is illustrated in Figure 4.8. Its behavior is similar to that of scattering coupling. The maximum spread occurs at  $\psi = 0$  or  $\pi$  and at  $t = s'$  where  $ts' = R'^2/2$  because  $t^2 + s'^2 = R'^2$ .

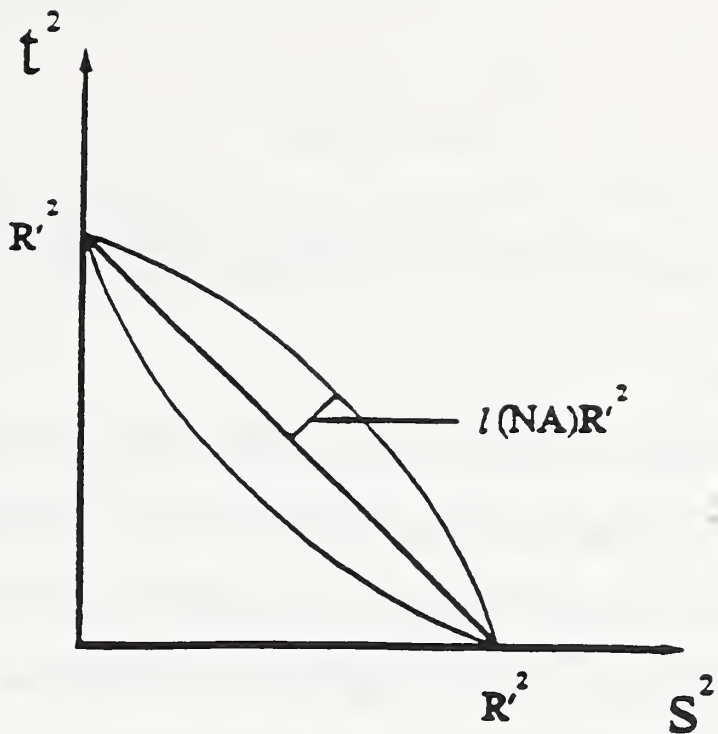


Figure 4.8: Illustration of mode spread due to longitudinal shift.

Thus for maximum spread we have

$$R^2 = R'^2 + l(NA)R'^2 \quad (4.26)$$

or

$$\begin{aligned} R &\simeq R' + \frac{l(NA)}{2}R' \\ &\simeq R' + 0.1lR'. \end{aligned} \quad (4.27)$$

Devices such as splices and power splitters have no gap between the two pieces of fiber that compose the device; that is,  $l = 0$ . The only device that has longitudinal displacement is the connector. Practical, high-quality connectors have very small value of  $l$ , which means a very narrow spread. Since connectors also exhibit scattering coupling (Chapter 5) and this localized coupling is similar to scattering coupling, its effect could be absorbed into the scattering coupling expression and thus be ignored.

## CHAPTER 5

### FIBER-OPTIC DEVICES AND THEIR TRANSFER FUNCTIONS

#### 5.1 Introduction

In this chapter we will discuss some fiber-optic devices commonly used in telecommunications systems. These devices are fibers and cables, connectors, splices, and power splitters. To derive the transfer functions, it is necessary to study the physical structure of these devices and find out how and where the two basic coupling mechanisms discussed in Chapter 4 contribute to modal power transfer in these devices. The devices can then be modeled in terms of the transfer functions of the two coupling mechanisms. Section 5.2 discusses fibers and cables while connectors and splices are discussed in Section 5.3. A power splitter is more complicated in structure and power coupling. Section 5.4 is dedicated to this kind of device.

A fiber-optic system is a concatenation of these devices. Once the transfer functions of the devices are known, the modal power transfer relation of the system can be formed by applying these functions successively. This can be expressed for a  $n$ -component system with the relation [61]

$$P^n(R^n) = \int_0^1 dR^{n-1} \int_0^1 dR^{n-2} \cdots \int_0^1 dR^0 T^n(R^n, R^{n-1}) T^{n-1}(R^{n-1}, R^{n-2}) \cdots T^1(R^1, R^0) P^0(R^0). \quad (5.1)$$

This relation is equivalent to expressing the system matrix as the product of matrices of constituent components when the transfer matrix is used to

characterize components and systems [61]:

$$\mathbf{T}^s = \mathbf{T}^n \mathbf{T}^{n-1} \cdots \mathbf{T}^1. \quad (5.2)$$

We would expect, according to the discussions of Chapter 3, that Equation (5.1) will give a more precise description of the power transfer property of the system.

Experiments were made on devices whose transfer functions are derived in this chapter. In the experiment, the input and output nearfield patterns of a device are measured. The input and output modal power distributions are then calculated by Equation (2.61). The transfer function with a set of chosen values of free parameters is then used to operate on the input modal power distribution to obtain the output modal power distribution, from which a predicted output nearfield pattern is calculated by Equation (2.60). This nearfield pattern is then compared with the measured output nearfield pattern. The transfer function is determined in this way by best fitting the measured and the predicted nearfield patterns using the least squares method. Experiments with two different launch conditions were made on many components to determine whether the transfer function of a component is independent of launch conditions. Experimental setup and procedures are exactly the same as those described in Section 3.4. Experimental results for different devices are shown in the relevant sections. Most of them are obtained from round-robin data taken by different participants and calculated by the transfer function method. Since parameters in the transfer function have physical meanings different from the transfer matrix elements, it is meaningless to compare the statistical results of the transfer function parameters with the matrix elements calculated from the same set of data. Matrices are calculated by operating the

transfer functions determined from different measurements on the same input modal power distribution using Equations (3.22-3.25) and (3.33-3.36). The statistical results of these matrices are then compared with those of the corresponding matrices directly determined from the same sets of measured data. In this way, a meaningful comparison can be made between the two approaches about their dependence on measurement launch conditions. Interpretations of the resultant values of the parameters are discussed. A concatenation experiment for a link containing only splices is also presented. Based on the experimental results, especially the comparison between results obtained from the same measurement data by the transfer matrix method and the transfer function method, some conclusions are made in Section 5.5.

## 5.2 Fibers and Cables

**5.2.1 Transfer function** Fibers and cables are the basic and perhaps the simplest devices in a fiber-optic system. Scattering coupling is the sole coupling mechanism in the fiber or cable itself. The transfer function of a fiber or cable is therefore exactly the same as the transfer function for scattering coupling. It is length dependent and is written

$$T_{fb}(R, R'; z) = [1 - \int_0^\infty z\alpha(R'', R')m(R'')dR'']\delta(R' - R) + z\alpha(R, R')m(R). \quad (5.3)$$

Important physical and propagation characteristics that are relevant to the transfer function of a piece of fiber or cable are core diameter, length, index profile, loss, and bandwidth (or dispersion). Two kinds of fibers with different nominal core diameters are now commonly being used: 50  $\mu m$  and 62.5  $\mu m$ . In the experiment as well as in real systems, different components must be of the same diameter. As long as this requirement is satisfied, core

diameter is not a critical parameter because radial position in our theory is always normalized with respect to the core radius. Random deviations of core diameter will cause scattering coupling, which was discussed in Section 4.2. The length  $z$  of the fiber appears in the transfer function. It is always combined with the coupling strength  $\alpha_0$ .  $\alpha_0 z$  can be determined from experiment. If the length is known, we can obtain the coupling strength  $\alpha_0$ , and fibers of different lengths can be compared. It is also possible to compare values of  $\alpha_0$  of a fiber before and after cabling and the see effect of cabling on the scattering of the fiber.

We have assumed in the derivation of the transfer function that the fiber has a parabolic index profile. This is appropriate because almost all present-day fibers are approximately parabolic index. However, the index profile of a real fiber will more or less deviate from the ideal profile, which is one source of error in the experimental results. The effect of random fluctuations of index profile has already been included in the scattering transfer function.

There are two major causes of loss in the fibers: scattering loss and absorption loss [62]. In high-quality fibers, absorption is reduced to a very low level, and scattering loss, especially the intrinsic Rayleigh scattering, dominates. This is manifested in the Rayleigh scattering behavior of the spectral loss characteristics of a good-quality fiber as is illustrated in Figure 4.3. The loss of a fiber or cable calculated from the scattering transfer function should be close to the measured loss if the fiber is of good quality. When the calculated value is notably lower than the measured value, we should consider the difference to be the absorption loss. Details of the differential mode attenuation could be obtained by including a differential mode loss term in the equation for

the length variation of modal power (Equation 4.7). This term is equivalent to the first term in Marcuse's coupled power equation.

The transfer function can be used to solve the modal dispersion problem in multimode fibers [63]. We write the time dependent equation of transfer,

$$\left( \frac{\partial}{\partial z} + \frac{1}{v_g(R)} \frac{\partial}{\partial t} \right) P(z, t, R) = \int_0^1 dR' \alpha(R, R') P(z, t, R'), \quad (5.4)$$

where  $v_g(R)$  is the group velocity of mode  $R$  and  $\alpha(R, R')$  is the same as defined in Equation (4.4). If absorption loss is significant, we could also include an extra term for differential mode attenuation. The first-order solution of Equation (5.4) is given by

$$P_1(z, t, R^2) = v_g(R^2) \int_{-\infty}^t dt' \int_0^1 d(R'^2) \alpha(R^2, R'^2) P(0, t' - \frac{z - v_g(R^2)(t - t')}{V_g(R'^2)}, R'^2). \quad (5.5)$$

The function  $v_g(R^2)$  is the group velocity of modes designated by  $R^2$  and is assumed to have the form

$$v_g(R^2) = v_{g0} + v_{g1} R^2. \quad (5.6)$$

Making some modifications in the nearfield measurement setup to include a laser diode and a fast detector, we can also measure the pulse broadening of the fiber in addition to the nearfield pattern. The modal dispersion  $v_g(R^2)$  as well as the transfer function of the fiber can thus be determined. Details about the modal dispersion are beyond the scope of this technical note.

**5.2.2 Experimental results** One of the artifacts in the round-robin test is a piece of cable about 200m long. The fiber has a  $62.5 \mu m$  core diameter and an  $NA \simeq 0.25$ . The cable is not connectorized, and the cut-back method was used in its measurement. The fitting results of the output nearfield measured by three participants are shown in Figures 5.1 - 5.3.

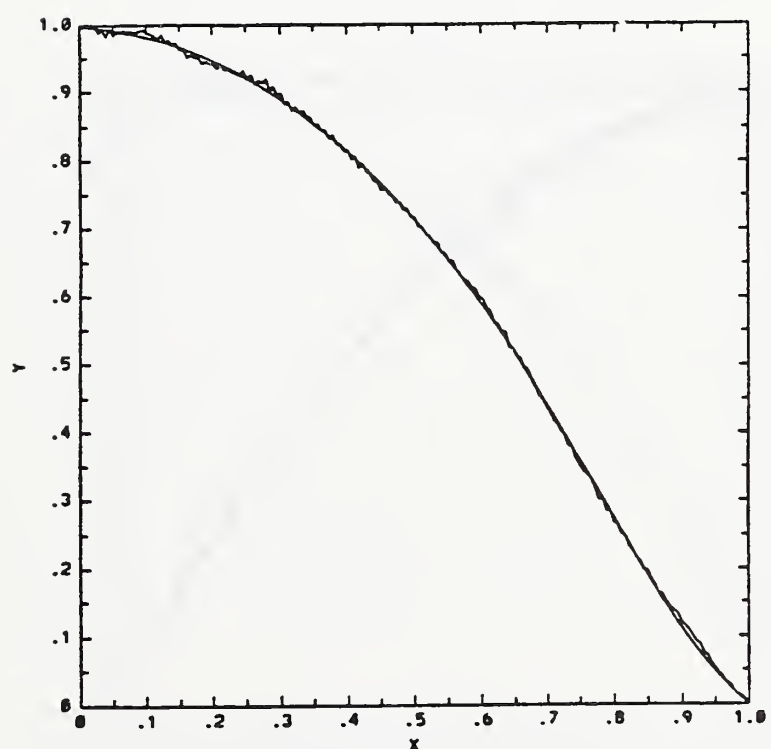
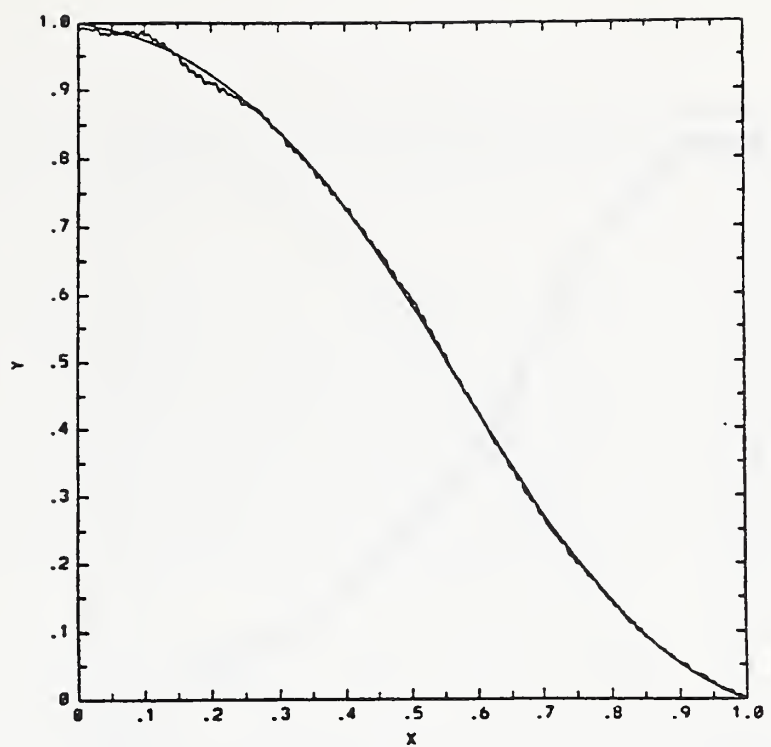


Figure 5.1. Curve fitting results of the nearfield pattern of cable canc measured by participant P1 for (a) central launch and (b) overfilled launch.

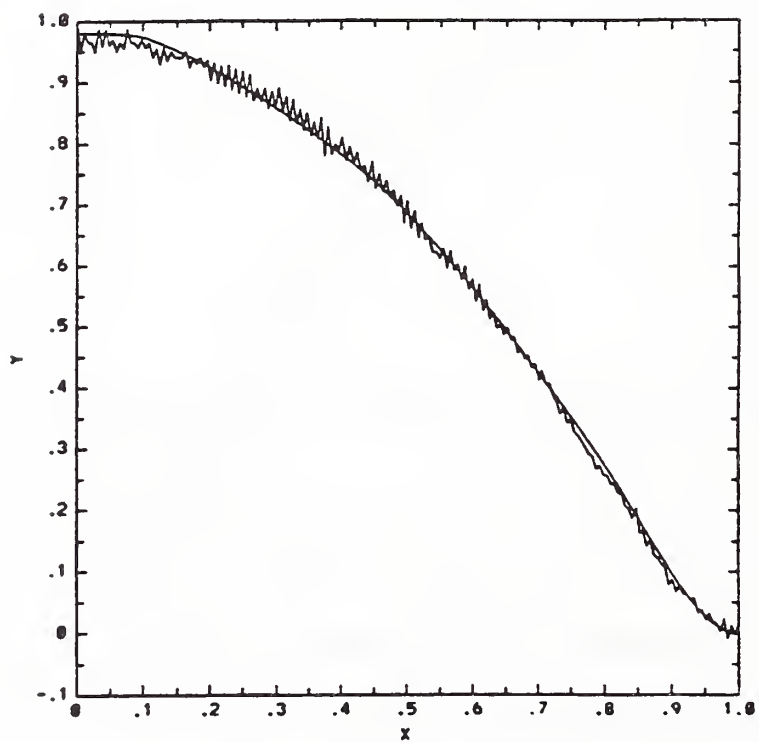
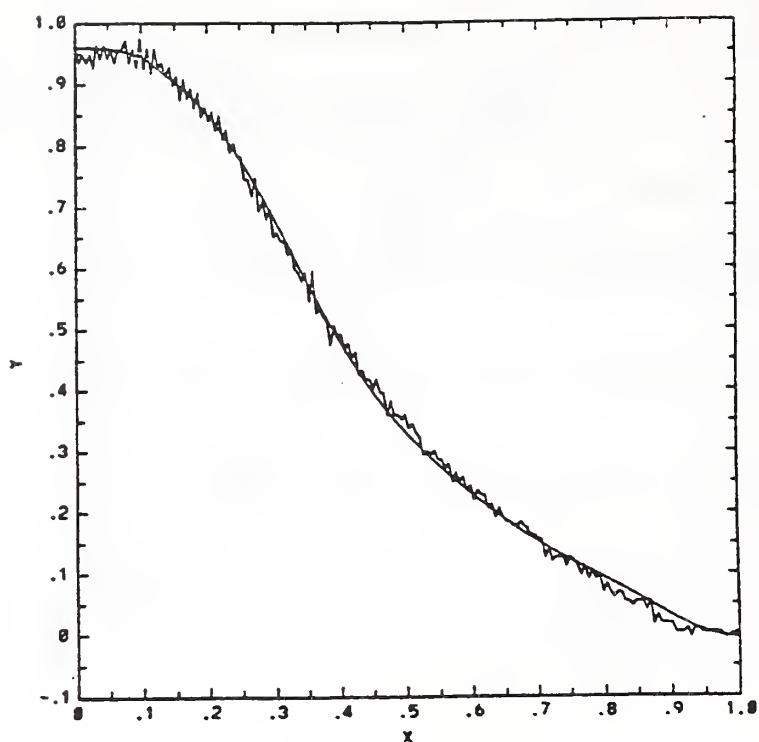


Figure 5.2. Curve fitting results of the nearfield pattern of cable canc measured by participant P2 for (a) central launch and (b) overfilled launch.

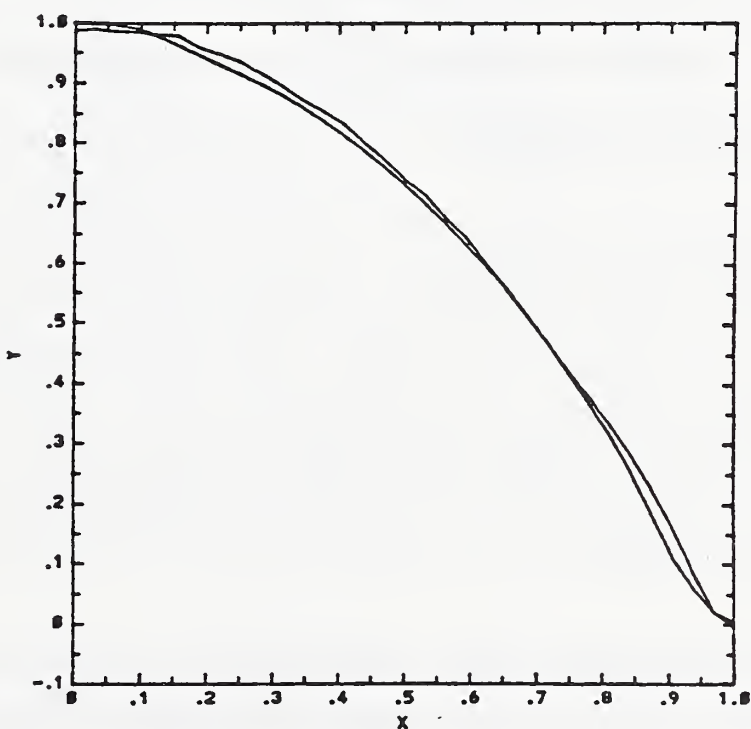
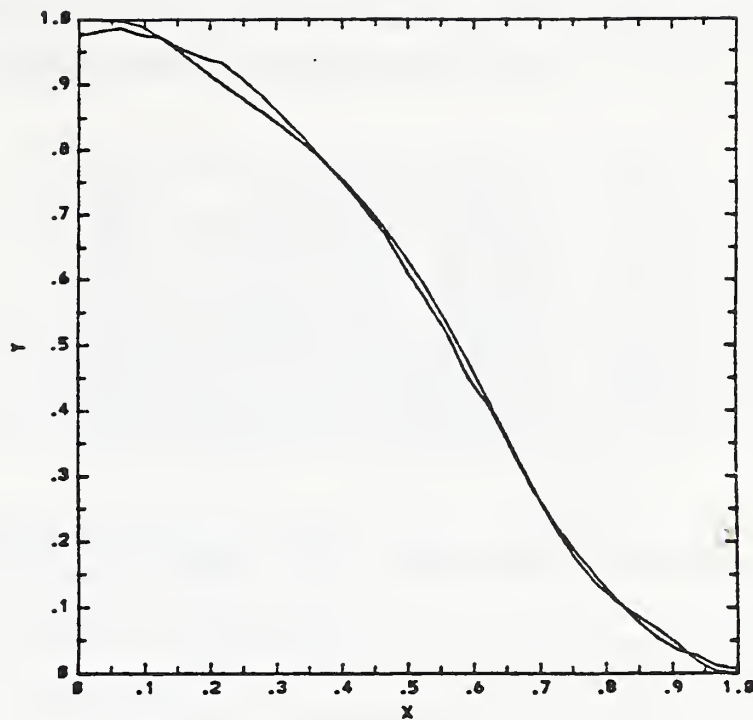


Figure 5.3. Curve fitting results of the nearfield pattern of cable canc measured by participant P3 for (a) central launch and (b) overfilled launch.

Table 5.1. Main parameters of the transfer function of cable canc determined from three measurements made by participant P1 using the same launch condition.

canc	$\tau$	$\alpha z$
P1-1	0.48	1.2
P1-2	0.32	1.7
P1-4	0.49	2.0
Average	0.43	1.5
Standard Deviation	0.09	0.4

Table 5.1 lists the values of the main parameters  $\tau$  and  $\alpha_0 z$  determined from three measurements made by P1 using the same launch condition. Table 5.2 lists the values of the same parameters determined from measurements made by P1, P2, and P3 using different launch conditions. Comparing the standard deviations in these two tables, we can see no indication of dependence of  $\tau$  and  $\alpha_0 z$  on launch conditions.

Since parameters of the transfer function have different physical meaning than the transfer matrix elements, transfer matrices are calculated by operating the transfer functions on the same input modal power distributions of central and overfilled excitations using Equations (3.22-3.25). The 'measured' matrices are then obtained from these matrices by using Equations (3.33-3.36),

Table 5.2. Main parameters of the transfer function of cable canc determined from measurements made by three participants using different launch conditions. Data for P1 are the average values in Table 5.1.

canc	$\tau$	$\alpha z$
P1	0.43	1.5
P2	0.60	1.2
P3	0.42	1.25
Average	0.48	1.3
Standard Deviation	0.10	0.2

Table 5.3. Transfer matrices of cable canc calculated from transfer functions measured by P1 using the same launch condition.

canc	$t_{11}$	$t_{12}$	$t_{21}$	$t_{22}$
P1-1	0.9918	0.0410	0.0032	0.8686
P1-2	1.0003	0.0377	-0.0013	0.8956
P1-3	0.9849	0.0383	0.0056	0.9067
Average	0.9923	0.0390	0.0025	0.8903
Standard Deviation	0.0077	0.0018	0.0035	0.0196

Table 5.4. Transfer matrices of cable canc calculated from transfer functions measured by three participants using different launch conditions. Data for P1 are the average values in Table 5.3.

canc	$t_{11}$	$t_{12}$	$t_{21}$	$t_{22}$
P1	0.9923	0.0390	0.0025	0.8903
P2	0.9259	0.0619	0.0296	0.7164
P3	0.9984	0.0352	0.0001	0.8550
Average	0.9722	0.0454	0.0107	0.8206
Standard Deviation	0.0402	0.0144	0.0164	0.0919

which are listed in Tables 5.3 and 5.4. Comparing the standard deviations in the last two tables, we can see that the standard deviation for the same launch condition is less than that for different launch condition, which indicates the dependence on launch condition of the measured transfer function. However, when this difference is compared with those in Tables 3.3 and 3.4, we can see that, except for  $t_{22}$ , the differences between the standard deviations for matrices determined from the transfer functions are much less than those for matrices directly calculated from the measurement results. This fact implies that the transfer function depends less on launch conditions than the transfer matrix. It might be too early to reach this conclusion from the result of only one component where one matrix element does not satisfy this conclusion. A more comprehensive comparison will be made in the conclusion section of this

chapter, where statistics of all the test components for the transfer function and the transfer matrix are calculated and more convincing conclusions will be reached.

### 5.3 Connectors and Splices

Connectors and splices are devices that link two pieces of fibers end to end. There are different kinds of connectors and splices according to the structure [64, 65, 66, 67]. The key portion of a connector of any structure is a thin tube to hold the fiber. The coating of the fiber is stripped before it is inserted into the tube. This is to avoid the effect of the eccentricity of the coating and ensure good alignment. The thin tube is filled with epoxy to fix the fiber with respect to the tube.

There are two commonly used splices: fusion splices [68, 69, 70] and rotary splices [71]. Fusion splices use an electric arc to fuse together two finely aligned fiber ends. The completed fusion splice is put in a glass tube to protect it. The splice is fixed inside the tube by epoxy. Rotary splices use three short thin glass rods that hold the two pieces of fiber between them. Then epoxy is used to fix the fiber ends. A copper clip keeps the glass rods together and holds and protects the splice.

A connector or a splice is basically a butt coupler. However, both devices hold a short piece of the fiber on each side of the actual connection and the actual connection, either fusion or the employment of epoxy, will deform or exert stress on sections of both fibers in the vicinity of the device, causing a significant amount of scattering coupling in spite of the short length of the fibers. Coupling can be characterized by a short scattering region, the overlap region, and another scattering region. The output modal power distribution

can therefore be obtained by operating on the input modal power distribution the scattering and overlap transfer functions in this order. Parameters in the two scattering processes can be assumed the same because the two sections are close to each other and are perturbed by the same operation. The factor  $K(R, R')$  is the same as in Equation (3.20) for connectors. Since fusion deforms the outer region of the fiber more than the central area and will result in scattering much stronger than the Rayleigh scattering, the parameter  $x$ , which represents the effect of Rayleigh scattering, is much less than  $y$ , which represents the effect of fusion, and can be taken to zero. Thus the factor  $k(R, R')$  in Equation (4.6) is reduced to

$$K(R, R') = \frac{[\min(R, R')]^2}{R'^2} R'^y. \quad (5.7)$$

Reduction of one parameter will ease the curve fitting in data processing.

**5.3.1 Experimental results of connectors** The results for one connector, ccml, are presented here. It is a connector with pigtailed fibers at both ends and was measured by using the cut-back method. The curve fitting results of measurements made by four participants are shown in Figures 5.4 - 5.7. The main transfer function parameters are listed in Tables 5.5 and 5.6. Standard deviations in these two tables show that parameters  $\tau$  and  $\alpha_0 z$  have some dependence on launch conditions, whereas the parameter  $d$  seems independent of launch conditions. Transfer matrices calculated from these transfer functions are listed in Tables 5.7 - 5.8. The standard deviations in Table 5.8, compared with their counterparts in Table 3.6, show less dependence on the launch condition of transfer matrices calculated from the transfer functions than those calculated directly by transfer matrix method, a fact which implies that for connectors the transfer function is less dependent on launch condition.

Table 5.5. Main parameters of the transfer function of connector ccm1 determined from four measurements made by participant P1 using the same launch condition.

ccm1	$\tau$	$\alpha z$	$d$
P1-1	0.57	0.69	0.24
P1-2	0.52	0.67	0.18
P1-3	0.54	0.61	0.20
P1-4	0.41	0.61	0.15
Average	0.51	0.64	0.19
Standard Deviation	0.07	0.04	0.04

Table 5.6. Main parameters of the transfer function of connector ccm1 determined from measurements made by four participants using different launch conditions. Data for P1 are the average values in Table 5.5.

ccm1	$\tau$	$\alpha z$	$d$
P1	0.51	0.64	0.19
P2	0.34	0.66	0.245
P3	0.26	1.14	0.23
P4	0.56	1.10	0.22
Average	0.42	0.88	0.22
Standard Deviation	0.14	0.27	0.02

Table 5.7. Transfer matrices of connector ccm1 calculated from transfer functions listed in Table 5.5.

ccm1	$t_{11}$	$t_{12}$	$t_{21}$	$t_{22}$
P1-1	0.8873	0.0642	0.0493	0.6838
P1-2	0.8585	0.0592	0.0673	0.5828
P1-3	0.8860	0.0602	0.0516	0.6586
P1-4	0.9266	0.0479	0.0331	0.7611
Average	0.8896	0.0579	0.0503	0.6716
Standard Deviation	0.0280	0.0070	0.0140	0.0735

Table 5.8. Transfer matrices of connector ccm1 calculated from transfer functions listed in Table 5.6. Data for P1 are the average values in Table 5.7.

ccm1	$t_{11}$	$t_{12}$	$t_{21}$	$t_{22}$
P1	0.8896	0.0579	0.0503	0.6716
P2	0.9137	0.0476	0.0501	0.5533
P3	0.9255	0.0563	0.0438	0.5450
P4	0.7867	0.0730	0.0936	0.5786
Average	0.8789	0.0587	0.0594	0.5871
Standard Deviation	0.0632	0.0105	0.0230	0.0581

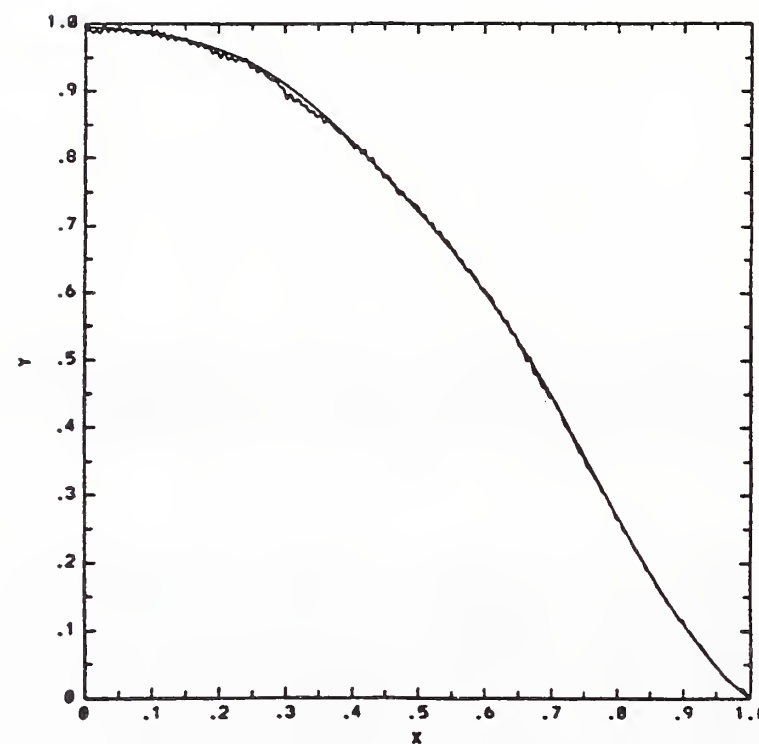
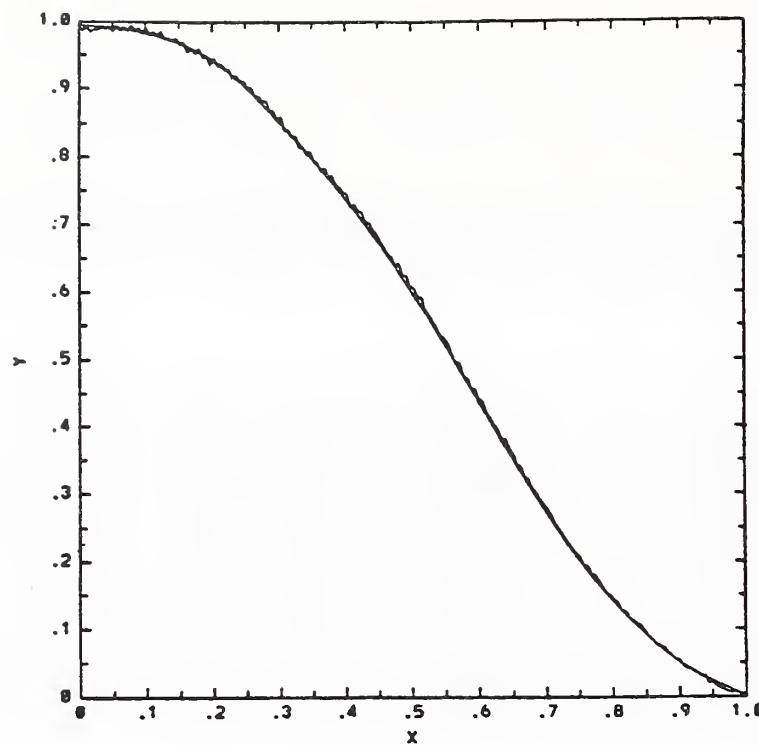


Figure 5.4. Curve fitting results of connector ccml measured by participant P1 for (a) central and (b) overfilled launches.

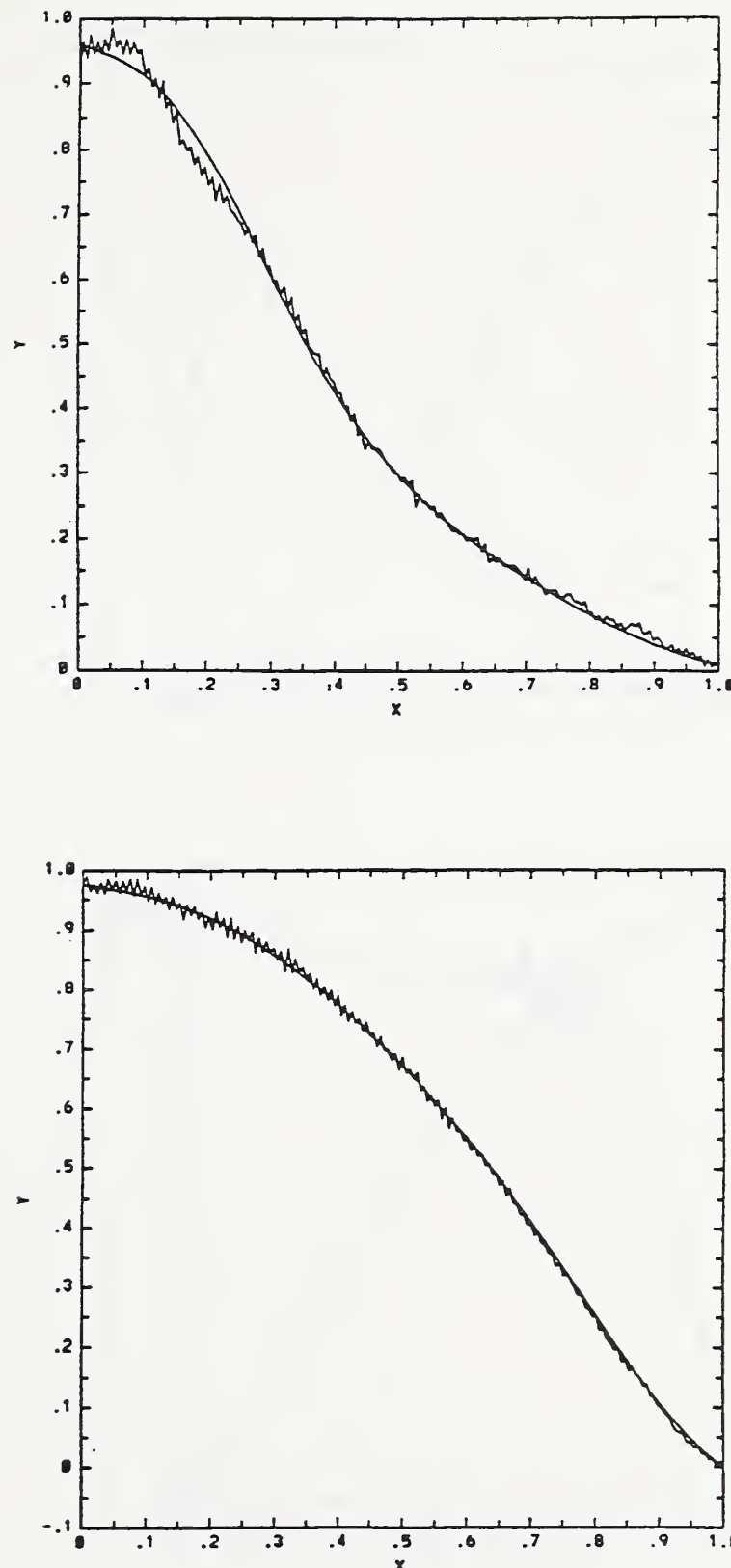


Figure 5.5. Curve fitting results of connector ccml measured by participant P2 for (a) central and (b) overfilled launches.

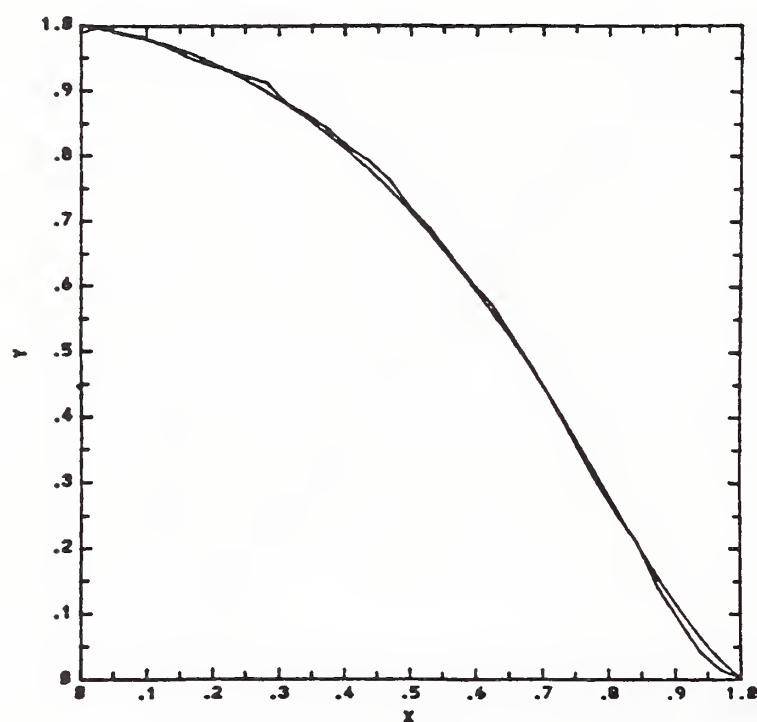
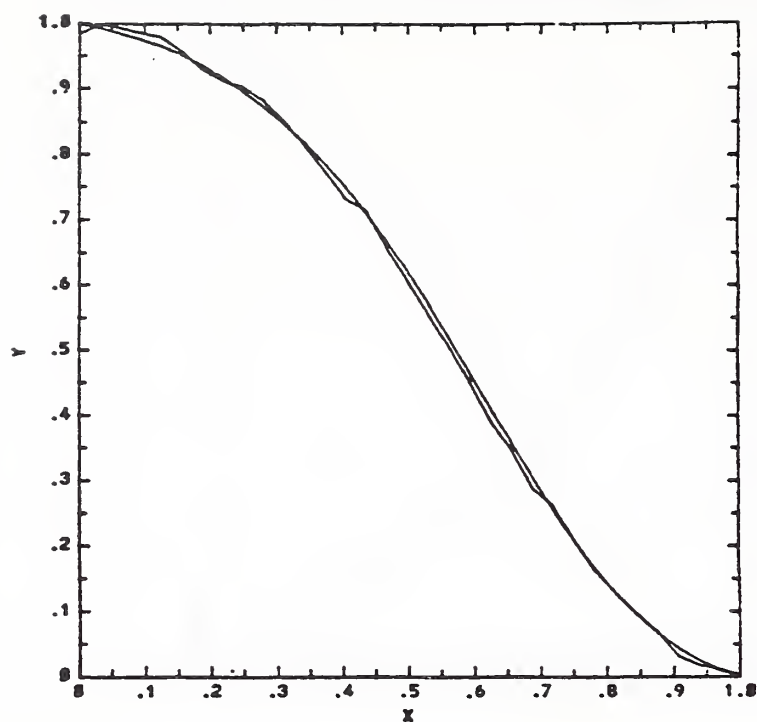


Figure 5.6. Curve fitting results of connector ccml measured by participant P3 for (a) central and (b) overfilled launches.

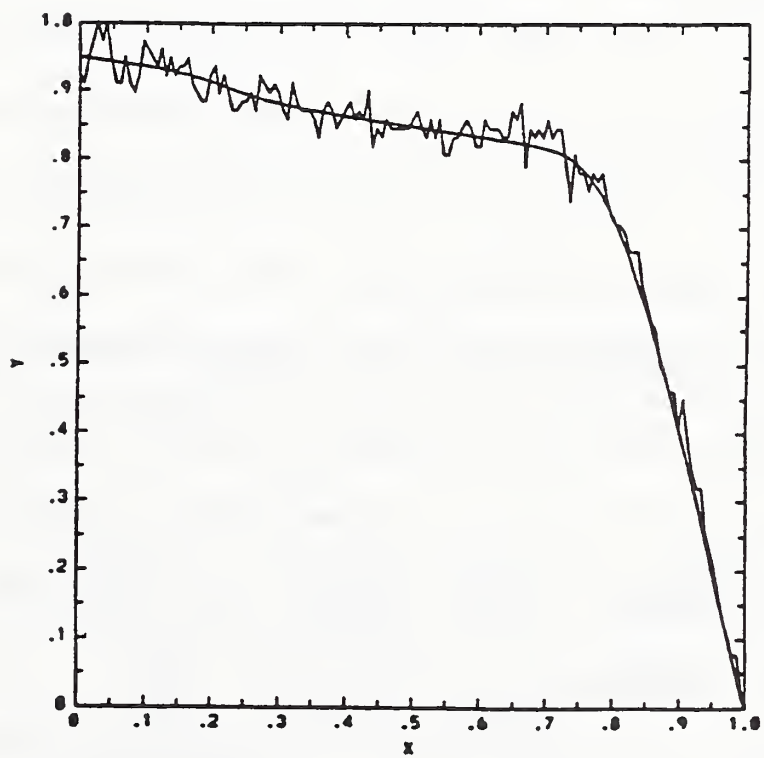
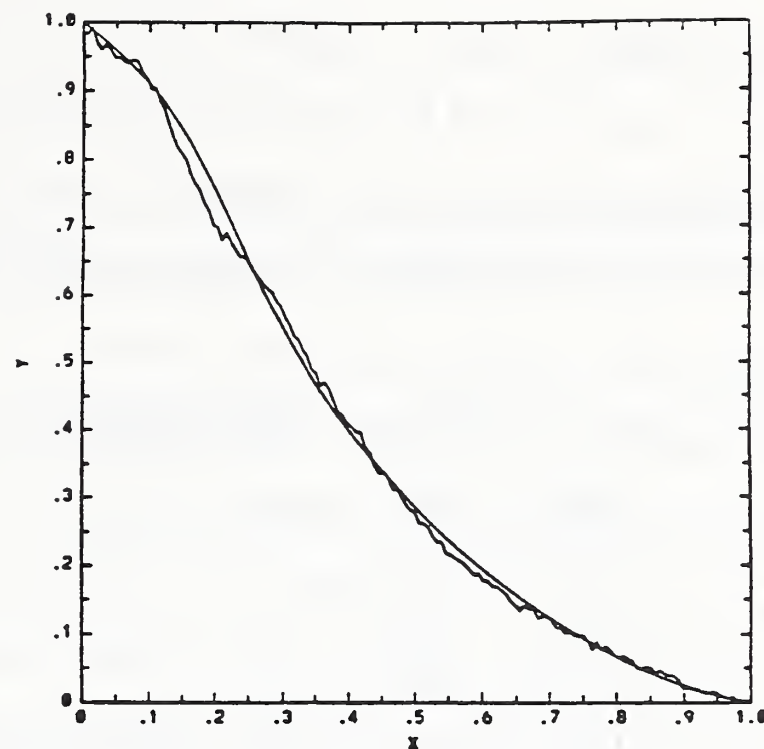


Figure 5.7. Curve fitting results of connector ccml measured by participant P4 using plane wave launch. (a) is low-order mode excitation, and (b) is high-order mode excitation.

### 5.3.2 Experimental results of splices and their concatenation

A concatenation experiment of four fusion splices was carried out to verify that the transfer function technique can be applied to concatenated links of components and to compare the precision of the three methods, that is, loss measurement, transfer matrix method, and transfer function method, in the prediction of loss of concatenated components. A 20-m section of  $125\text{-}\mu\text{m}$  outer diameter,  $62.5\text{-}\mu\text{m}$  core diameter, 0.26-NA multimode fiber was selected. The fiber was cut 2m from the end and then respliced with a fusion splicing apparatus. The fiber was then cut 2m in from the splice and then respliced. This procedure was repeated until the link contained four splices, each located 2 m from its nearest neighbor(s). The end, located 12m from the nearest splice, was chosen as the input end. The input and output nearfield patterns and the loss were measured with central and overfilled excitations using the cut-back method described in Section 3.6. The four splices were then cut from the link and input and output nearfield patterns and loss for each were measured with central and overfilled excitations. The measured data were processed to get both the transfer matrix and the transfer function. The measured loss, the transfer matrix, and the parameters of the transfer function for individual splices are listed in Table 5.9. The curve fitting of the transfer function method for the individual splices are shown in Figures 5.8 - 5.11.

The measured and predicted loss and matrices for the link are listed in Table 5.10. The predicted loss for the loss measurement method is simply the sum of the loss of each splice and no matrix can be obtained using this method. The concatenated matrix is the product of the matrices of the four splices using Equation (5.2) and the concatenated loss is calculated by operating with

Table 5.9. Measured loss for central and overfilled excitations, transfer matrices, and main parameters of transfer functions of splices sp1, sp2, sp3, and sp4.

	$l_c$ (dB)	$l_o$ (dB)	Matrix		$\tau$	$\alpha z$	$d$
sp1	0.062	0.491	0.9139	0.0779	0.03	1.5	0.16
			0.0838	0.6804			
sp2	0.274	0.475	1.0719	-0.0589	0.18	1.1	0.16
			-0.0478	0.7905			
sp3	0.126	0.751	0.9265	0.1039	0.10	2.0	0.19
			0.0820	0.5793			
sp4	0.215	0.836	1.1765	-0.3853	0.01	0.3	0.25
			-0.1157	0.9209			

Table 5.10. Measured loss for central and overfilled excitations and transfer matrix of the concatenation of the four splices compared with those calculated from the losses and matrices of the individual splices measured by the three methods.

SP1-4	$l_c$ (dB)	$l_o$ (dB)	Matrix	
Measured Value	0.834	2.081	0.9071	-0.0841
			0.0268	0.3376
Loss Measurement	0.677	2.553		
Transfer Matrix	0.497	1.755	1.0294	-0.0080
			-0.0191	0.2772
Transfer Function	0.778	2.110	0.8665	-0.0829
			0.0587	0.3062

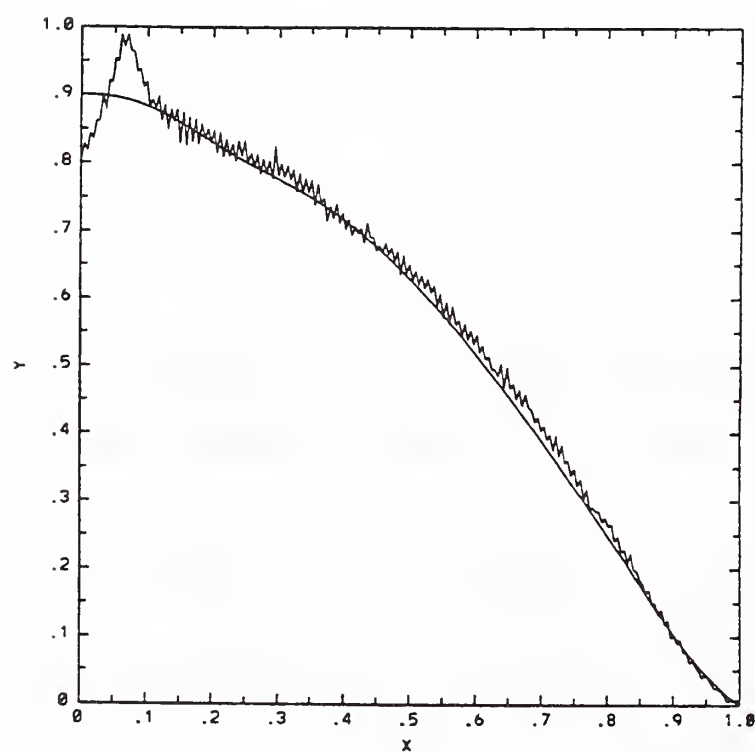
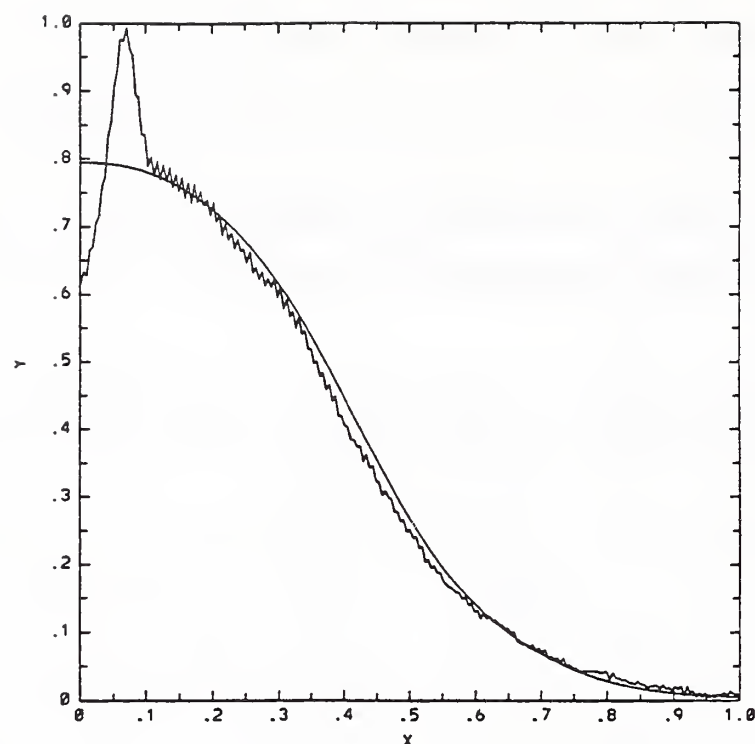


Figure 5.8. Curve fitting results of splice SP1 for (a) central excitation, and (b) overfilled excitation.

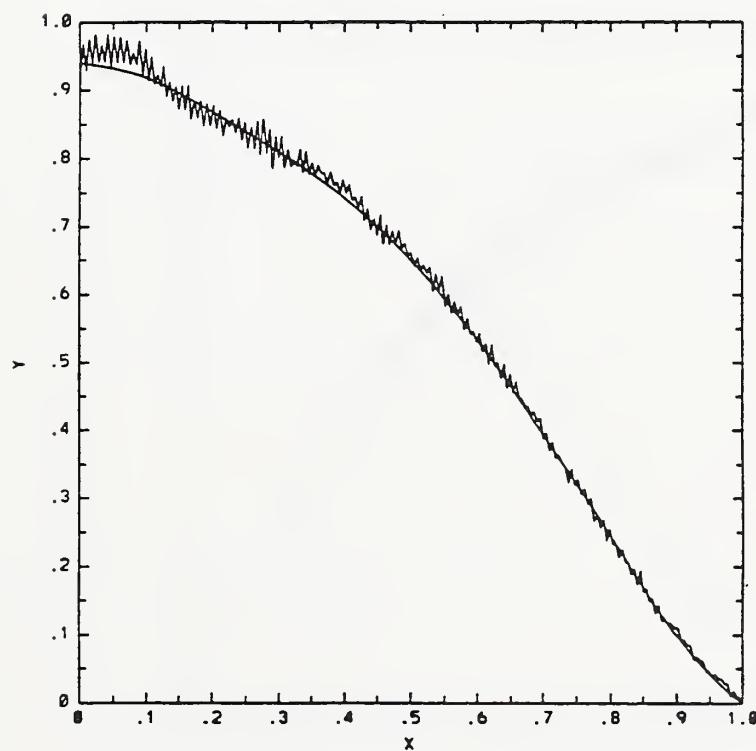
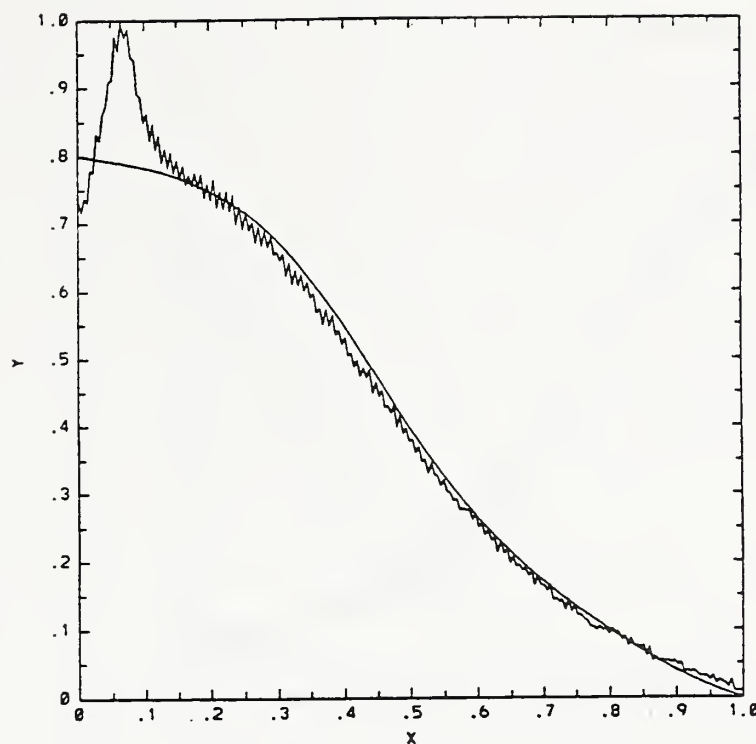


Figure 5.9. Curve fitting results of splice SP2 for (a) central excitation, and (b) overfilled excitation.

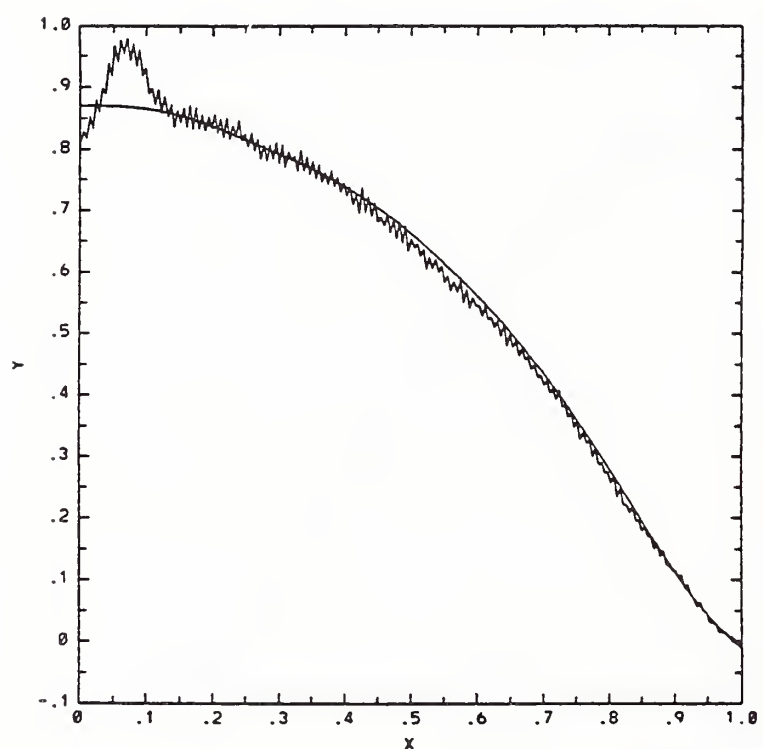
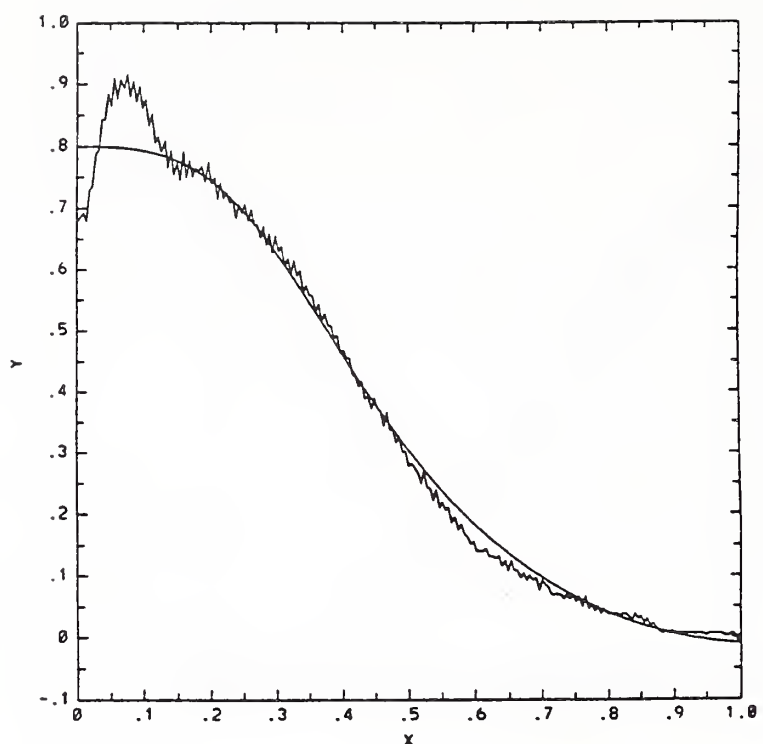


Figure 5.10. Curve fitting results of splice SP3 for (a) central excitation, and (b) overfilled excitation.

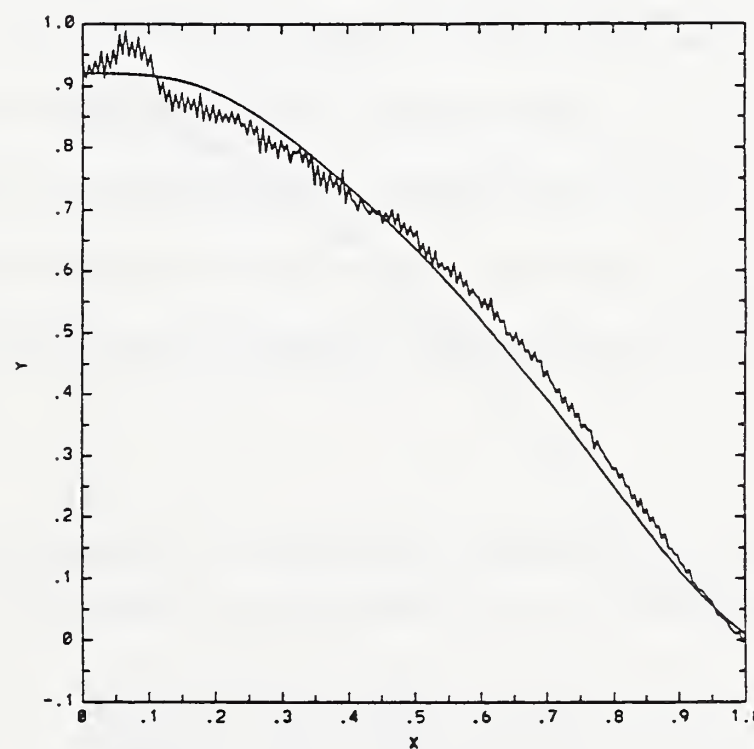
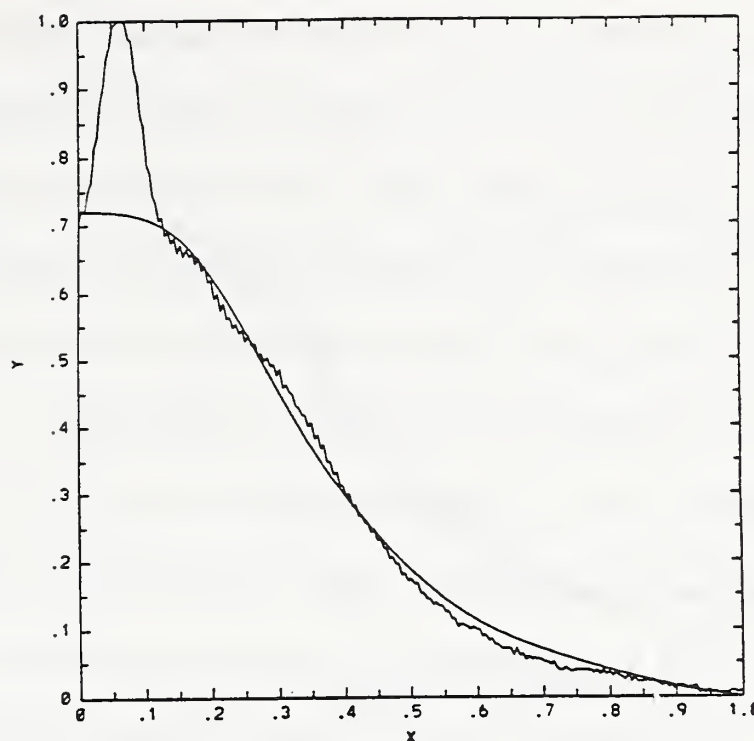


Figure 5.11. Curve fitting results of splice SP4 for (a) central excitation, and (b) overfilled excitation.

this resultant matrix on the input modal power vector calculated from the input modal power distribution. The concatenation of the individual transfer functions are performed using Equation (5.1) and the resulting nearfield fits well with the measured nearfield for both launch conditions as shown in Figure 5.12. The concatenated matrix and loss can be obtained at the same time, although the concatenated matrix is not necessary in this case.

Table 5.10 shows clearly that the transfer function method can predict the concatenated loss better than the other two methods. The result of the transfer matrix method is unexpectedly poor and is worse than most previous work reported in the literature [18, 19]. This is probably because in our experiment the launch condition is not strictly controlled, as is manifested in the variation of the values of  $k_1$  and  $k_2$  listed in Table 5.11. The values of  $k_2$  for overfilled launch are reasonably uniform because overfilled launch has a better repeatability. Previous experiments by other laboratories may have had better control of the launch condition. However, this once more reveals the important disadvantage of the transfer matrix method: its dependence on launch conditions.

Table 5.11. A list of  $k_1$  and  $k_2$  defined in Equation 3.37, which shows how the launch conditions are different for the measurement of each splice and their concatenation.

	sp1	sp2	sp3	sp4	sp14
$k_1$	19.127	2.434	7.762	3.814	5.262
$k_2$	0.776	0.774	1.059	0.815	0.860

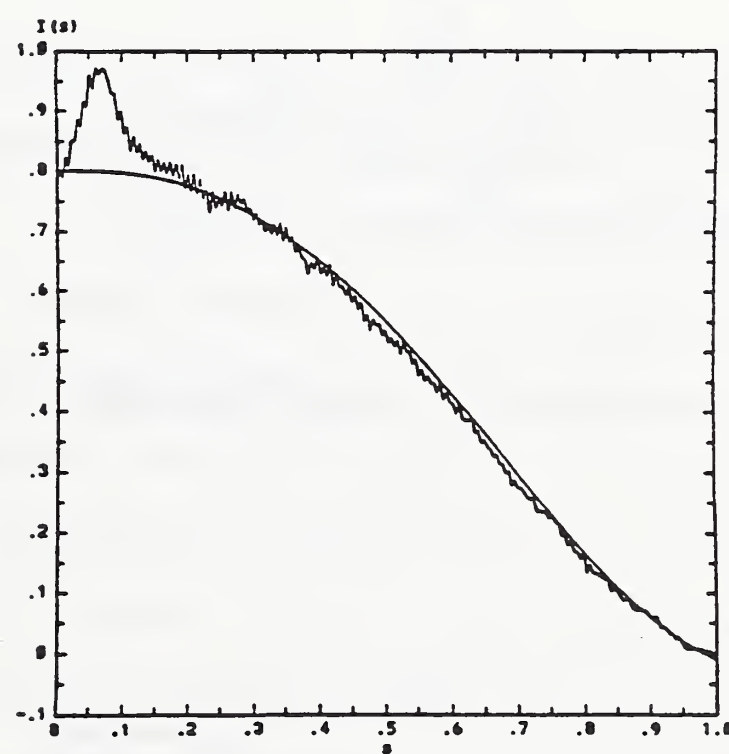
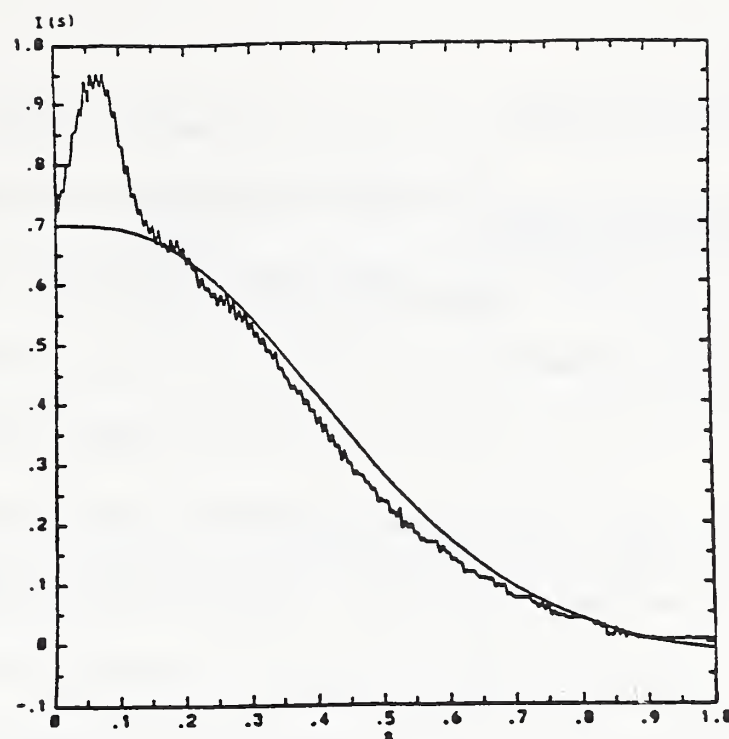


Figure 5.12. Nearfield pattern predicted from the transfer functions of individual splices and the measured nearfield pattern for concatenated splices for (a) central excitation, and (b) overfilled excitation.

## 5.4 Power Splitters

A fiber-optic power splitter belongs to a broader category of devices called fiber-optic couplers [72, 73], which are divided into two groups: power splitters and wavelength division multiplexers (WDMs). Power splitters can also be divided into 3-port couplers and star couplers, which are multiport couplers. Power splitters are used in local area networks (LANs). 3-port couplers are used for fiber-optic signal tapping and distribution, and star couplers for optical bus systems and multiport application. Light entering a coupler is split out to two or more output ports. The splitting ratio depends on the structure for the device and the fabrication process. There are three different structures of 3-port couplers:

1. The offset structure is shown in Figure 5.13. This is evidently an overlap coupling device, and the splitting ratio is mode dependent. This structure has a high insertion loss.
2. The semi-transparent mirror is illustrated in Figure 5.14. The two output ports collect the transmitted and the reflected light separately. The splitting ratio is determined by the thickness of the semi-transparent mirror. The splitting ratio is independent of mode order and wavelength.
3. The fused biconical taper [74], shown in Figure 5.15, is the most common 3-port coupler. Two pieces of fiber are twisted around each other and then heated in the middle until they fuse together. It has low insertion loss, but the splitting ratio is mode dependent. Fused biconical tapered power splitters have found wide application in optical fiber distribution networks because of their versatility, high performance, relatively low cost, and ease of fabrication.

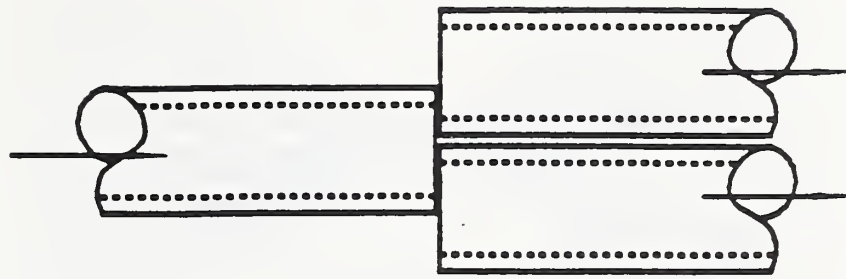


Figure 5.13: Schematic diagram of a coupler of the offset structure.

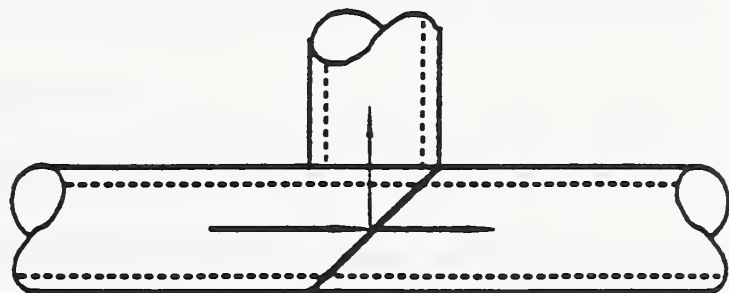


Figure 5.14. Schematic diagram of the semi-transparent mirror structure of couplers.

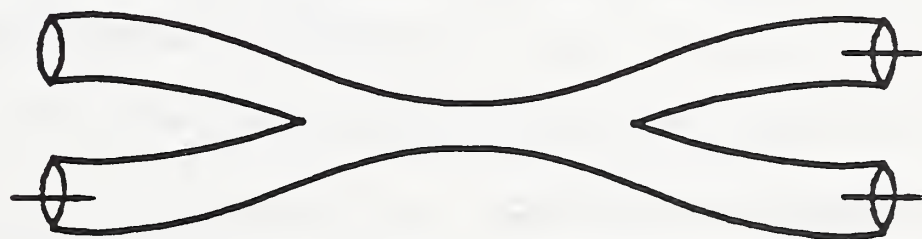


Figure 5.15. Schematic diagram of fused biconical taper structure of couplers.

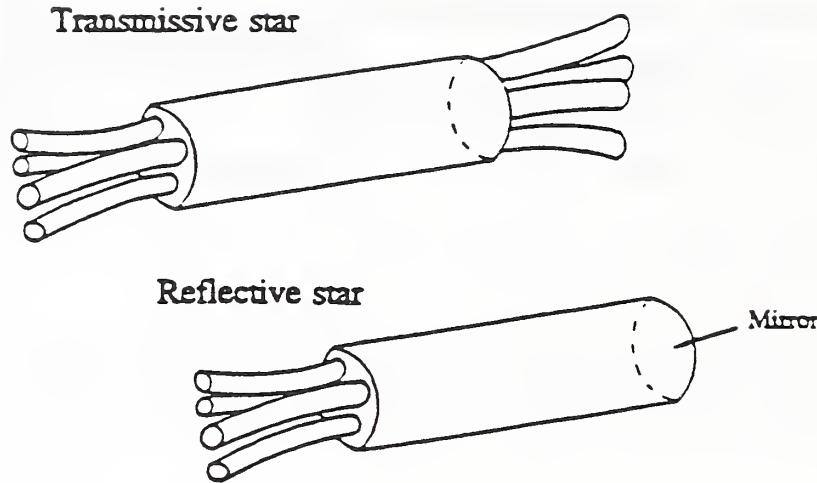


Figure 5.16: Structure of mixed-rod star couplers.

Star couplers have two different kinds of structures:

1. The mixer-rod structure, illustrated in Figure 5.16, has a thin platelet of quartz glass in the middle with several pieces of fiber attached to both ends. The platelet is embedded in a layer of adhesive of lower refractive index and thus becomes a waveguide. The light coupled into the mixer platelet from any of the input fibers will achieve a uniform spatial distribution and produce almost the same power in all the output ports. This structure is similar to the offset structure and also has a high insertion loss.

2. The fused biconical taper structure [75] is shown in Figure 5.17. This is the multi-port version of the 3-port fused biconical coupler. The splitting ratio is mode dependent and the port-to-port output variation is relatively wide. The insertion loss is low.

WDM couplers are essentially not power splitters. We will not discuss them in this technical note.

Couplers with offset structure are overlap coupling devices; therefore,

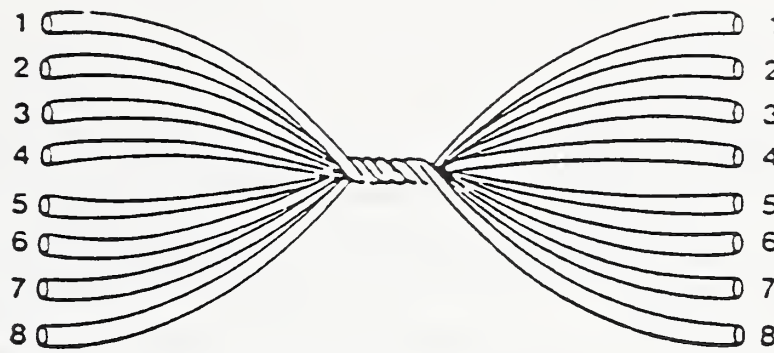


Figure 5.17: Structure of fused biconical tapered star couplers.

their transfer functions are exactly the overlap transfer function. Because the assembly may also affect the sections of fibers close to the coupling endface, a scattering-overlap-scattering model similar to that of connectors and splices may be employed.

Couplers of the semi-transparent structure are simpler devices regarding the power transfer process. The splitting ratio, which is independent of mode parameter, describes the power transfer properties of these devices.

Power coupling in power splitters of the fused biconical taper structure is much more complicated. The next sections are dedicated to the derivation of the transfer function of 3-port power splitters with this structure. Experimental results are presented in the section following the derivation. Multi-port power splitters of the same structure can, in principle, be derived in the same way, though it is even more complicated.

**5.4.1 A model of 3-port fused biconical taper power splitters** The structure of a 3-port fused biconical tapered power splitter can be portrayed as in Figure 5.18. The twisting of the fibers is not drawn in the

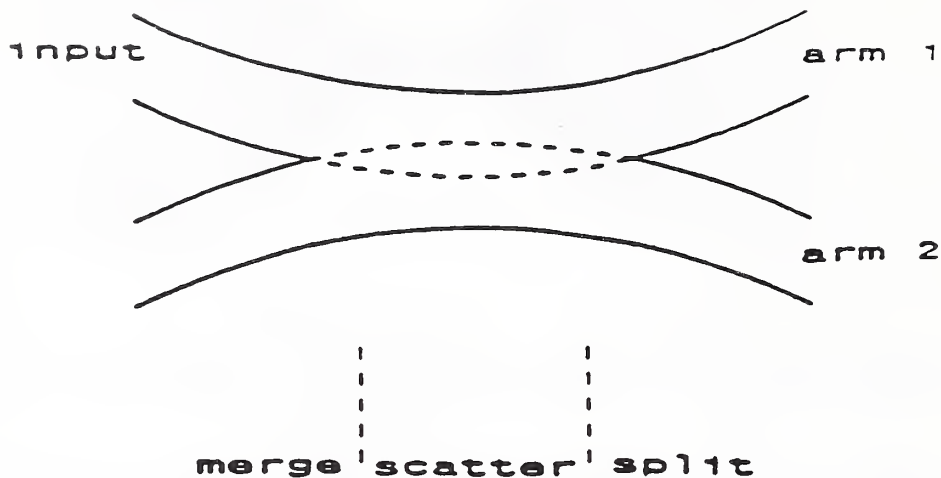


Figure 5.18. Schematic diagram of the structure of a 3-port fused biconical taper power splitter.

figure because the effect of the twisting will be built into the values of the fitting parameters. The two output ports are often called the straight port and the coupled port. The straight port and the input port are the two ends of one of the two fibers. In the experimental results we shall call the straight port, port 1, and the coupled port, port 2. The structure can be roughly divided into three sections according to different physical processes and coupling mechanisms: the merging, scattering, and splitting sections. The transfer functions for these sections will be derived separately in the following.

(i) Merging: Modal power coupling in the merging section is very similar to that in butt coupling; that is, power is coupled from one piece of fiber to the other due to geometrical overlap. The major difference in the two cases is that power is completely transferred from the first fiber to the second in butt coupling, while in the merging region, the two fibers coexist in the overlapping section and power is shared by the two pieces of fiber. However,



Figure 5.19. Idealized index profile and mode composition before and after merging

the modal power coupled to the second fiber as well as that remaining in the first fiber are still proportional to what the overlap coupling transfer function would predict.

At the completion of merging, the two pieces of fiber become one entity. Its idealized geometry and index contours are depicted in the cross sectional diagram of Figure 5.19. The curves in the diagram are also boundaries of different modes as in the simple case of a undeformed circular fiber waveguide. Since the middle parts of the two fibers do not merge, the lower-order modes in these unmerged regions are unaffected by the process. Higher-order modes which had the same mode parameter in the two original fibers will be shared by the two fibers and become joint modes. The modal power transfer relations can be derived from these assertions as follows.

For  $R < l/2$  (separate lower-order modes)

$$P_{1m}(R) = \int_0^1 [1 - \frac{1}{2} \int_0^\infty T_{ol}(R'', R') dR''] P_{1m}(R') \delta(R - R') dR', \quad (5.8)$$

$$P_{2m}(R) = \frac{1}{2} \int_0^1 T_{ol}(R, R') P_{1m}(R') dR'. \quad (5.9)$$

For  $R > l/2$  (joint higher-order modes)

$$\begin{aligned}
 P_{1m}(R) &= P_{2m}(R) \\
 &= \frac{1}{2} \int_0^1 [1 - \frac{1}{2} \int_0^\infty T_{ol}(R'', R') dR''] P_{1m}(R') \delta(R - R') dR' \\
 &\quad + \frac{1}{4} \int_0^1 T_{ol}(R, R') P_{1m}(R') dR'.
 \end{aligned} \tag{5.10}$$

Notice that the kernel function of both these relations is still the overlap coupling transfer function  $T_{ol}$ .

(ii) Scattering: Scattering coupling in a power splitter is basically the same as in a simple piece of optical fiber. The difference is the mode composition. In power splitters, the mode composition is characterized by joint higher-order modes and separate lower-order modes as stated above. Thus power in higher-order modes is shared by the two fibers throughout the entire middle merged section of the power splitter. However, power is still coupled between different modes of the same fiber. Since the fabrication of the power splitter involves twisting and fusing of the fibers, scattering coupling is very strong compared to that in a normal unstressed piece of fiber; this is manifested in a large value of  $\alpha z$  in the experimental results in spite of the very small value of the length  $z$  of the device.

(iii) Splitting: Splitting is the reverse of merging. The mode structure experiences a transition as shown in Figure 5.20. The modal power coupling is still characterized by overlapping and sharing of power by overlapping modes. The power transfer relations are expressed as

$$\begin{aligned}
 P_{1m}(R) &= \int_0^1 [1 - \frac{1}{2} \int_0^\infty T_{ol}(R'', R') dR''] P_{1m}(R') \delta(R - R') dR' \\
 &\quad + \frac{1}{2} \int_0^1 T_{ol}(R, R') P_{2m}(R') dR'
 \end{aligned} \tag{5.11}$$



Figure 5.20. Idealized index profile and mode composition before and after splitting.

$$\begin{aligned} P_{2m}(R) = & \int_0^1 [1 - \frac{1}{2} \int_0^\infty T_{ol}(R'', R') dR''] P_{2m}(R') \delta(R - R') dR' \\ & + \frac{1}{2} \int_0^1 T_{ol}(R, R') P_{1m}(R') dR'. \end{aligned} \quad (5.12)$$

The parameter  $l$ , the normalized lateral shift, is the same in merging as in splitting.

**5.4.2 Experimental results** The results of one power splitter psg are presented here. The fitting results are shown in Figures 5.21-5.26. The main transfer function parameters are listed in Tables 5.12 and 5.13. Similarly to the experimental results of connector ccml, the parameters  $\tau$  and  $\alpha z$  show more dependence on launch condition than the parameter  $d$ . Transfer matrices are calculated from these transfer functions and are listed in Tables 5.14 - 5.15. Comparing the standard deviations for participant P1 and those for the three participants for the corresponding matrices also show a certain dependence on the launch condition of the transfer function. However, the standard deviations in Table 5.15, as opposed to their counterparts in Table 3.8, indicate that the transfer function is less dependent on the launch condition than the transfer matrix.

Table 5.12. Main parameters of the transfer function of power splitter psg determined from five measurements made by participant P1 using the same launch condition.

psg	$\tau$	$\alpha z$	$d$
P1-1	0.13	8.0	0.16
P1-2	0.13	7.8	0.22
P1-3	0.13	7.5	0.18
P1-4	0.13	7.6	0.18
P1-5	0.13	7.4	0.19
Average	0.13	7.7	0.19
Standard Deviation	0.00	0.2	0.02

Table 5.13. Main parameters of the transfer function of power splitter psg determined from measurements made by three participants using different launch conditions. Data for P1 are the average values in Table 5.12.

psg	$\tau$	$\alpha z$	$d$
P1	0.13	7.7	0.19
P2	0.15	8.5	0.25
P4	0.20	7.0	0.19
Average	0.16	7.7	0.21
Standard Deviation	0.04	0.7	0.03

Table 5.14. Transfer matrices of power splitter psg calculated from transfer functions measured by participant P1 using the same launch condition.

port 1	$t_{11}$	$t_{12}$	$t_{21}$	$t_{22}$
P1-1	0.5011	-0.0047	-0.0186	0.3809
P1-2	0.5026	0.0010	-0.0511	0.3553
P1-3	0.5043	-0.0031	-0.0368	0.3623
P1-4	0.5043	-0.0031	-0.0366	0.3612
P1-5	0.5041	-0.0020	-0.0410	0.3627
Average	0.5033	-0.0024	-0.0368	0.3645
Standard Deviation	0.0014	0.0021	0.0118	0.0096
port 2	$t_{11}$	$t_{12}$	$t_{21}$	$t_{22}$
P1-1	0.4918	0.0030	-0.0100	0.3737
P1-2	0.4896	0.0085	-0.0392	0.3485
P1-3	0.4935	0.0043	-0.0268	0.3555
P1-4	0.4934	0.0044	-0.0265	0.3543
P1-5	0.4927	0.0056	-0.0304	0.3558
Average	0.4922	0.0052	-0.0266	0.3576
Standard Deviation	0.0016	0.0021	0.0106	0.0095

Table 5.15. Transfer matrices of power splitter psg calculated from transfer functions measured by three participants using different launch conditions. Data for P1 are the average values in Table 5.14.

port 1	$t_{11}$	$t_{12}$	$t_{21}$	$t_{22}$
P1	0.5033	-0.0024	-0.0368	0.3645
P2	0.4871	0.0103	-0.0207	0.3575
P4	0.4757	0.0207	-0.0179	0.2689
Average	0.4887	0.0095	-0.0251	0.3303
Standard Deviation	0.0139	0.0116	0.0102	0.0533
port 2	$t_{11}$	$t_{12}$	$t_{21}$	$t_{22}$
P1	0.4922	0.0052	-0.0266	0.3576
P2	0.4737	0.0190	-0.0085	0.3496
P4	0.4621	0.0292	-0.0056	0.2612
Average	0.4760	0.0178	-0.0136	0.3228
Standard Deviation	0.0152	0.0120	0.0114	0.0535

Table 5.16. Main parameters of the transfer function of power splitter psg, dp1, and dp2. dp1 and dp2 were made by the same manufacturer while psg was made by a different manufacturer.

	$\tau$	$\alpha z$	$d$
psg	0.16	7.7	0.21
dp1	0.11	22.0	1.07
dp2	0.14	23.0	0.97

Two power splitters, dp1 and dp2, which are not round-robin test artifacts, were measured before the round-robin measurement. These two power splitters were fabricated by the same manufacturer, while the round-robin power splitter was made by a different manufacturer. The transfer function parameters for all three power splitters are listed in Table 5.16, where the values for psg are the average values in Table 5.13. The values of  $\alpha z$  and  $d$  for dp1 and dp2 are close to each other while significantly different from those for psg. This fact implies that the transfer function parameters have physical significance and may be used for the analysis of the structure or the fabrication process of the devices in addition to the characterization of the components.

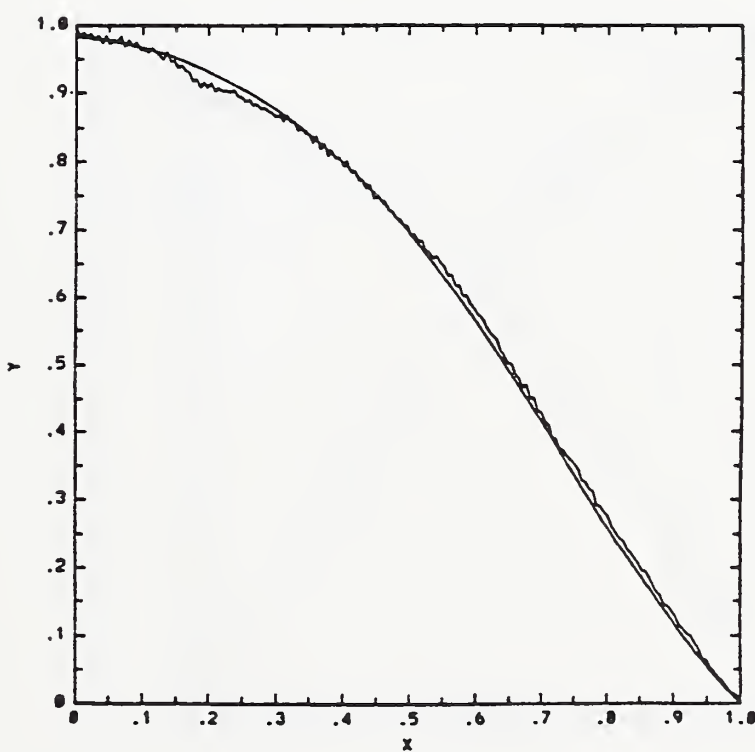
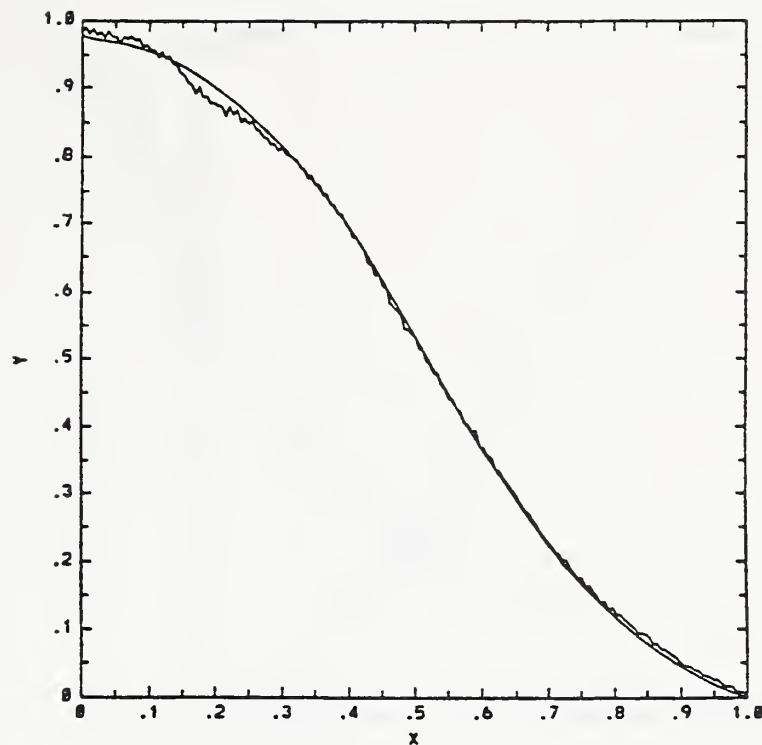


Figure 5.21. Curve fitting results of port 1 of power splitter psg measured by P1 for (a) central launch and (b) overfilled launch.

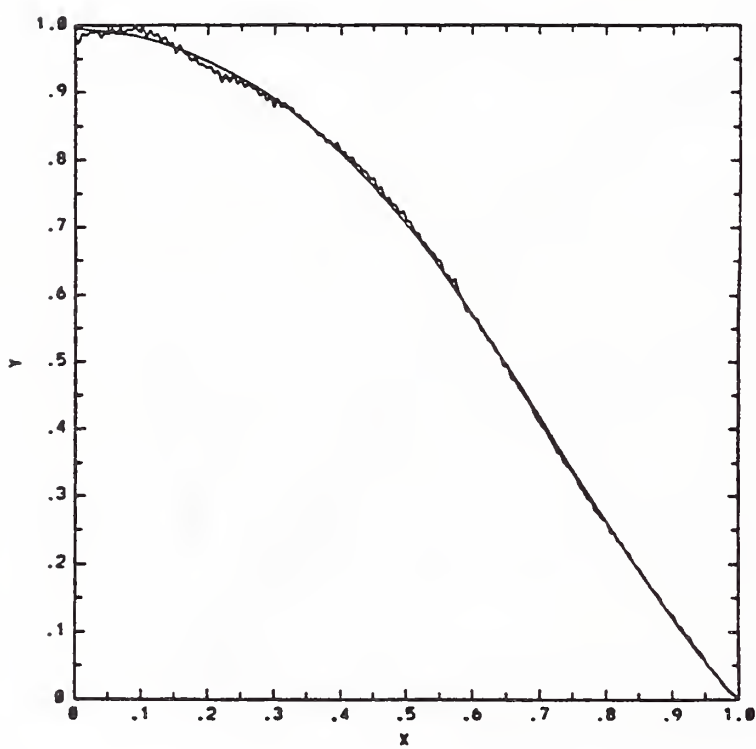
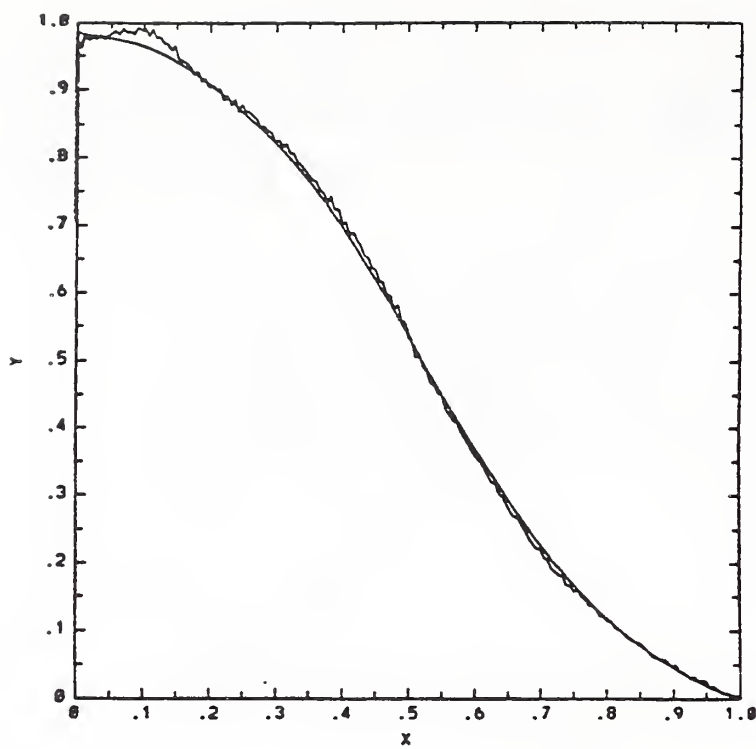


Figure 5.22. Curve fitting results of port 2 of power splitter psg measured by P1 for (a) central launch and (b) overfilled launch.

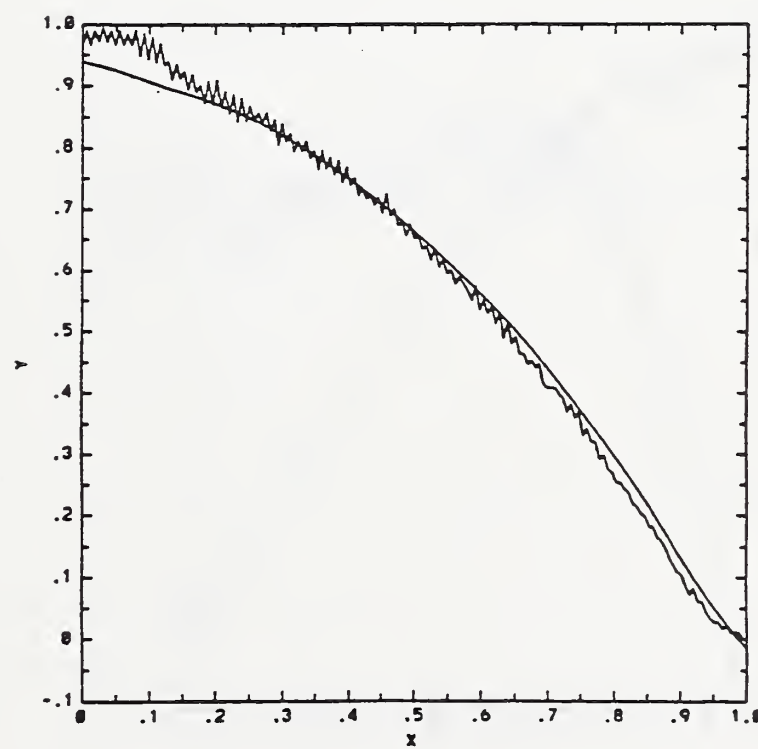
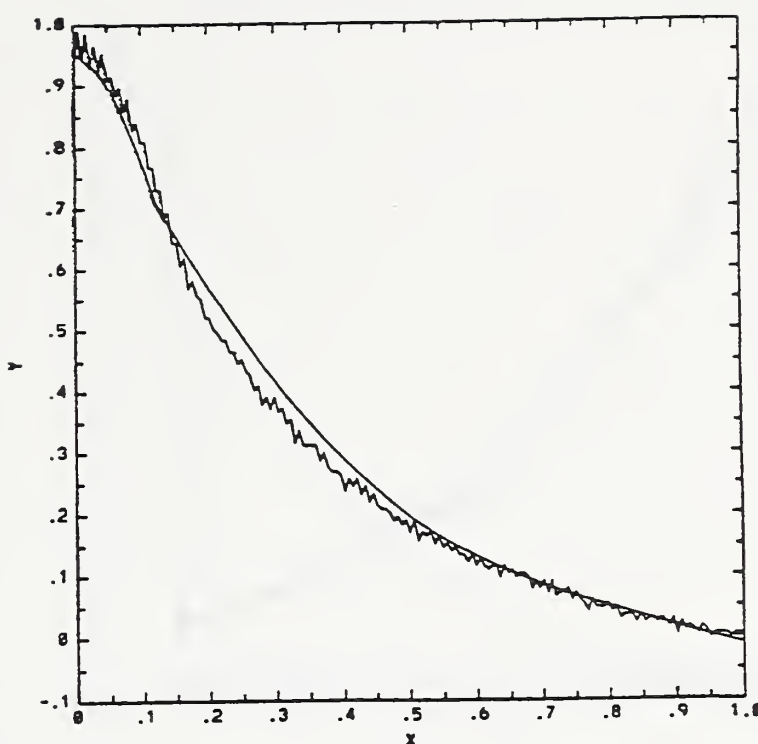


Figure 5.23. Curve fitting results of port 1 of power splitter psg measured by P2 for (a) central launch and (b) overfilled launch.

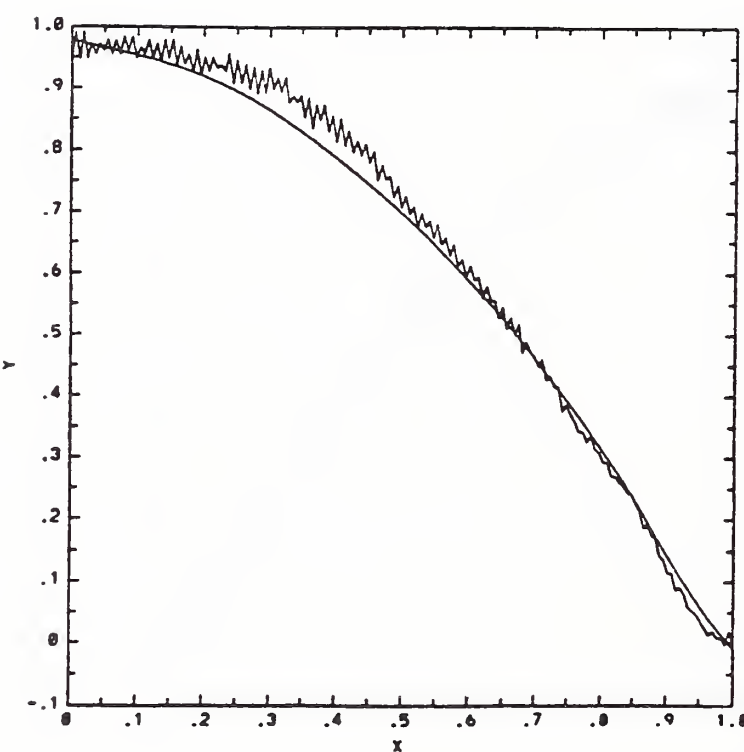
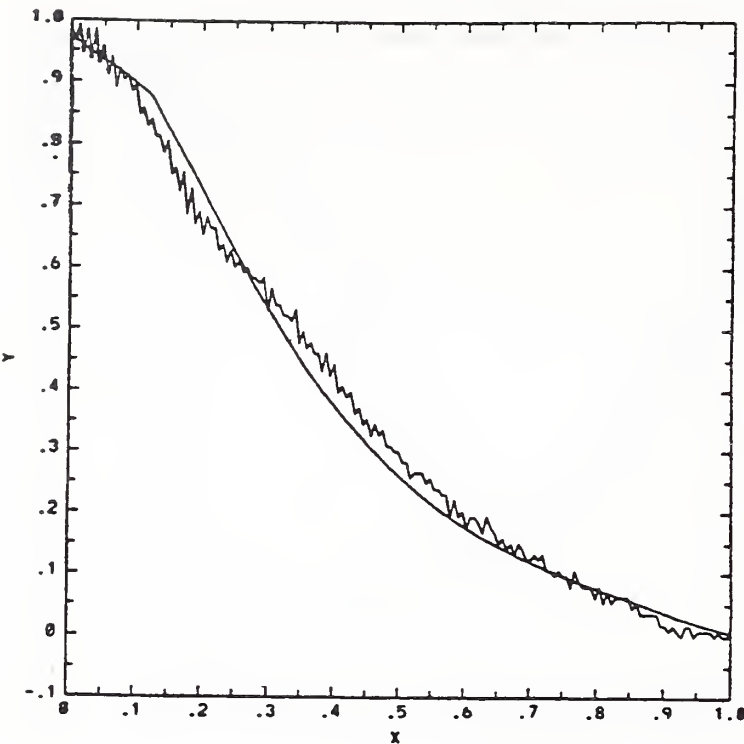


Figure 5.24. Curve fitting results of port 2 of power splitter psg measured by P2 for (a) central launch and (b) overfilled launch.

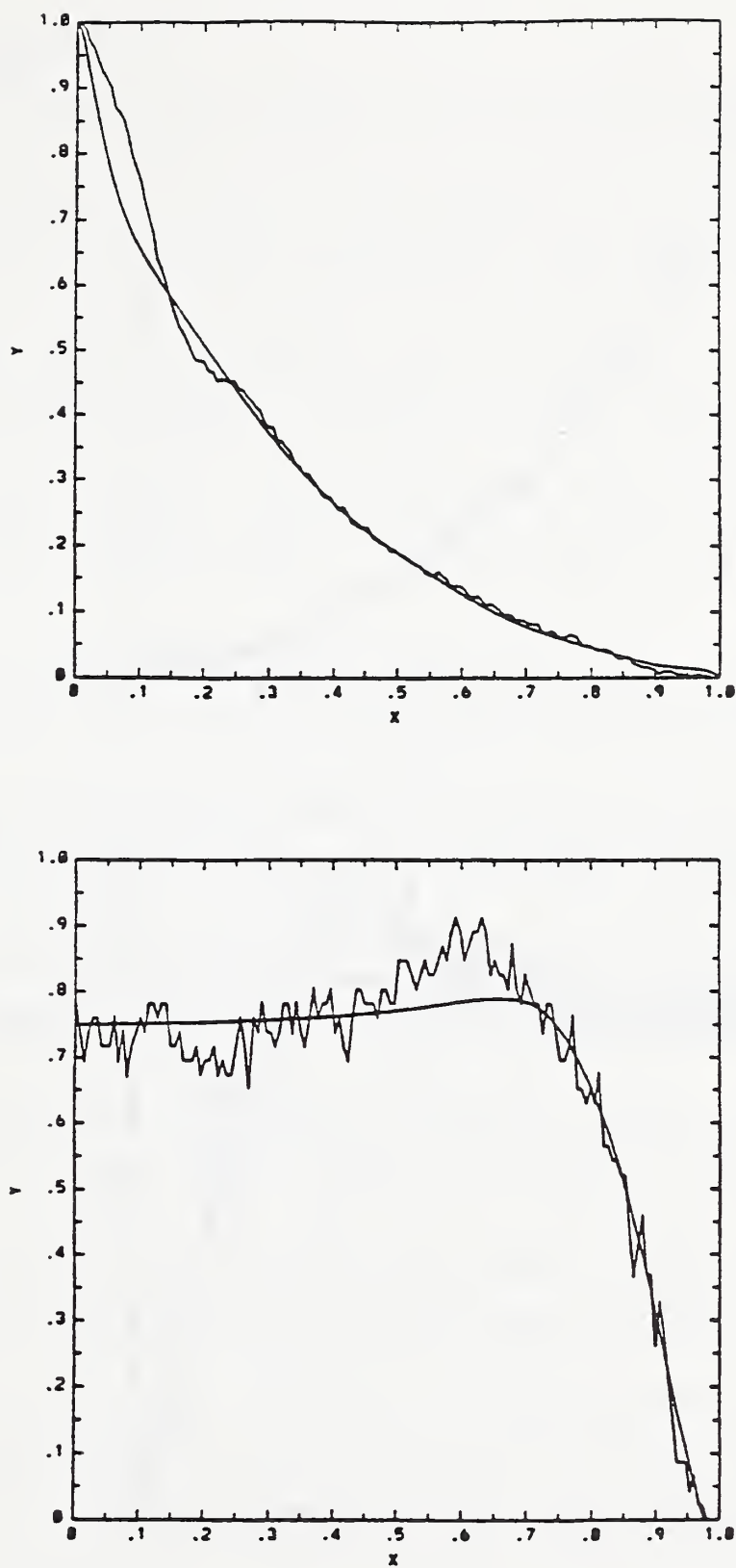


Figure 5.25. Curve fitting results of port 1 of power splitter psg measured by P4 for (a) low-order mode excitation and (b) high-order mode excitation.

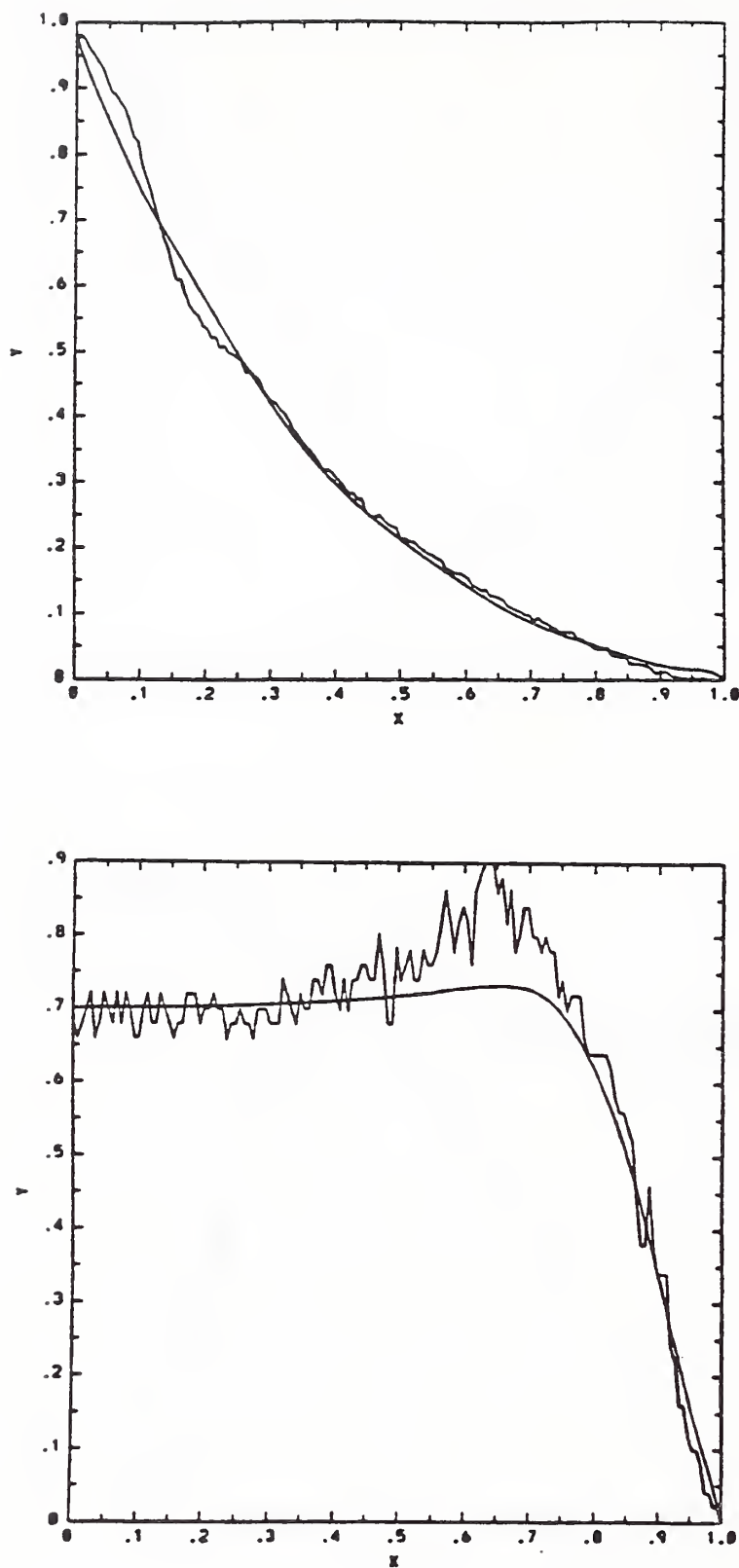


Figure 5.26. Curve fitting results of port 2 of power splitter psg measured by P4 for (a) low-order mode excitation and (b) high-order mode excitation.

## 5.5 Conclusions

I have demonstrated the measurement results and the statistics of one sample of each kind of the round-robin component and compared, for each of them, the results of using the transfer matrix method and the transfer function method. It is time now to make an overall comparison of the accuracy of the two methods with more data. Table 5.17 lists the standard deviation of the transfer matrix elements of seven round-robin components measured by one participant of the round-robin test, listed as SD-P1, and those measured by three or four different participants, listed as SD-All.

Table 5.18 is a list of the standard deviation of the transfer matrix elements calculated from the transfer functions determined from the same sets of data measured by P1 and by all the participants. Let us first compare the data in the last two lines of the two tables. For both methods, the standard deviation of different participants is greater than that of one participant, a fact which indicates that both methods depend on launch conditions. However, comparing the magnitude of this difference of the two methods shows that the transfer function method is much less dependent on launch conditions than the transfer matrix method. This is demonstrated in Table 5.19 where the differences are listed for the two methods. The improvement is significant. What is more important is that the cause of dependence on launch conditions of the measured results of the two methods is fundamentally different. The cause of the dependence of the transfer matrix method on launch conditions lies in the method per se, as was analyzed in Chapter 3; whereas the dependence of the experimental results on launch conditions for the transfer function method is due to the fact that the theoretical model for the transfer functions of various

devices can not always be perfect. One cause might be that the parameters  $\tau$  and  $\alpha z$  in the scattering transfer function are different for different scattering mechanisms. Since different scattering mechanisms could have different effects at different radial positions in the fiber, the values of  $\tau$  and  $\alpha z$  could be a function of  $R$ . The values of the two parameters determined in the present model represent some average effect of these mechanisms. To make these parameters vary with  $R$  will introduce more parameters and greatly complicate the curve fitting process. We have to make a compromise between convenience and accuracy.

Further, the standard deviation of  $t_{22}$  calculated for P1 by using the transfer function method is greater than that by using the transfer matrix method. Similarly, the net improvement of  $t_{22}$  of the transfer function method over the transfer matrix method, that is, the difference between the values of  $t_{22}$  in the last line of Tables 5.17 and 5.18, is not large. One possible reason is that the transfer function method uses the details of the input modal power distribution and output nearfield pattern. Errors in the measurement or in data processing may influence the result of the transfer function method more than that of the transfer matrix method. The nearfield pattern is always affected at the edge of the core by the diffraction limit and by leaky modes. This will in turn result in errors in the modal power distribution, mainly the higher-order modes. Most participants did not take any special precautions to reduce this error. That is why  $t_{22}$  has the largest error in the transfer function method. However, the overall accuracy of  $t_{22}$  for the transfer function method is still notably better than that for the transfer matrix method. By standardizing the correction technique regarding those effects, we can anticipate that the

Table 5.17. Comparison of standard deviations of measured matrices by participant P1 using the same launch condition and by different participants using different launch conditions.

Component		$t_{11}$	$t_{12}$	$t_{21}$	$t_{22}$
ccm1	SD-P1	0.0192	0.0305	0.0124	0.0240
	SD-All	0.1636	0.0778	0.0305	0.1404
cpm1	SD-P1	0.0071	0.0409	0.0094	0.0159
	SD-All	0.1082	0.1039	0.0196	0.1337
ccl	SD-P1	0.0275	0.0261	0.0132	0.0542
	SD-All	0.0941	0.0492	0.0509	0.0896
caec	SD-P1	0.0037	0.0471	0.0140	0.0078
	SD-All	0.1176	0.0665	0.1172	0.1551
canc	SD-P1	0.0212	0.0253	0.0193	0.0225
	SD-All	0.1404	0.1857	0.0611	0.0616
psg port 1	SD-P1	0.0120	0.0147	0.0042	0.0236
	SD-All	0.1088	0.0768	0.0461	0.0282
psg port 2	SD-P1	0.0138	0.0147	0.0075	0.0234
	SD-All	0.0757	0.0434	0.0443	0.0374
Average	SD-P1	0.0149	0.0285	0.0114	0.0245
	SD-All	0.1155	0.0861	0.0528	0.0922

Table 5.18. Comparison of standard deviations of matrices calculated from transfer functions measured by participant P1 using the same launch condition and by different participants using different launch conditions.

Component		$t_{11}$	$t_{12}$	$t_{21}$	$t_{22}$
ccm1	SD-P1	0.0280	0.0070	0.0140	0.0735
	SD-All	0.0632	0.0105	0.0230	0.0581
cpml	SD-P1	0.0544	0.0276	0.0126	0.0370
	SD-All	0.0414	0.0210	0.0189	0.0346
ccl	SD-P1	0.0070	0.0025	0.0103	0.1326
	SD-All	0.0302	0.0188	0.0051	0.0376
caec	SD-P1	0.0048	0.0201	0.0003	0.0343
	SD-All	0.0906	0.0166	0.0311	0.1300
canc	SD-P1	0.0077	0.0018	0.0035	0.0196
	SD-All	0.0402	0.0144	0.0164	0.0919
psg port 1	SD-P1	0.0013	0.0021	0.0118	0.0096
	SD-All	0.0139	0.0116	0.0102	0.0533
psg port 2	SD-P1	0.0016	0.0021	0.0106	0.0095
	SD-All	0.0152	0.0120	0.0114	0.0535
Average	SD-P1	0.0150	0.0090	0.0090	0.0451
	SD-All	0.0421	0.0150	0.0166	0.0656

Table 5.19. Difference of standard deviations for the MTF and MTM methods between statistical results of measurements made by P1 and of measurements made by different participants.

	$t_{11}$	$t_{12}$	$t_{21}$	$t_{22}$
MTF	0.0271	0.0060	0.0076	0.0205
MTM	0.1006	0.0577	0.0414	0.0678

accuracy of the transfer function method will further be improved.

In addition to the improvement in the accuracy and precision in predicting the loss of optical fiber devices and systems, the transfer function also has the potential to improve the prediction of bandwidth of such systems because it gives details of mode coupling, which has a big impact on the pulse broadening of an optical fiber system. The transfer function may also be used to analyze the structure of the devices and the effect of assembly on the devices.

#### ACKNOWLEDGEMENTS

I wish to thank Professor Alan R. Mickelson for his guidance in this research. My thanks also goes to Dr. Robert L. Gallawa, whose encouragement and support made it possible to start and complete this research project. I would also thank Dr. Matt Young, who made valuable comments and corrections on the original manuscript.

The discussion about the accuracy of mode transfer matrix using the expansion of mode transfer function is mainly Dr. Dag R. Hjelme's contribution, which is very much appreciated. I would also thank him and Dr. Michael Yadlowsky for many valuable discussions.

My thanks were also given to Igor P. Vayshenker, who built the original measurement setup, and to Indra P. Januar and Chon Howe Oon, who did some of the measurements and data processing.

## BIBLIOGRAPHY

- [1] K.C. Kao and G.A. Hockham, "Dielectric-fiber surface waveguides for optical frequencies," **Proc. IEEE** (London), vol. 113, pp. 1151-1158, 1966
- [2] F.P. Kapron, D.B. Keck, and R.D. Maurer, "Radiation loss in glass optical waveguide," **Appl. Phys. Lett.**, vol. 17, pp. 423-425, 1970
- [3] W.G. French, J.B. McChesney et al., "Optical waveguides with very low losses," **Bell Syst. Tech. J.**, vol. 53, no. 5, pp. 951-954, 1974
- [4] E.E. Basch, R.A. Beaudette, and H.A. Carnes, "Optical transmission for interoffice trunks," **IEEE Trans. Commun.**, vol. COM-26, pp. 1007-1014, July 1978
- [5] M.I. Schwartz, W.A. Reenstra, J.H. Mullins, and J.S. Cook, "Chicago lightwave communications project," **Bell Syst. Tech. J.**, vol. 57, pp. 1881-1888, July-August 1978
- [6] G.E. Keiser, **Local Area Networks**, McGraw-Hill, New York, 1989
- [7] D.B. Keck, "Spatial and temporal power transfer measurements on a low-loss optical waveguide," **Appl. Opt.**, vol. 15, p. 1882, 1974
- [8] R. Olshansky and S.M. Oaks, "Differential mode attenuation measurements in graded-index fibers," **Appl. Opt.**, vol. 17, p. 1830, 1978
- [9] R. Olshansky, M.G. Blankenship, and D.B. Keck, "Launch-dependent attenuation measurements in graded-index fibers," **Second European Conference on Optical Fiber Communication**, Paris, 1976
- [10] A.H. Cherin, E.D. Head, C.R. Lovelace, and W.B. Gardner, "Selection of mandrel wrap mode filters for optical fiber loss measurement," **Fiber and Integrated Optics**, vol. 4, p. 49, 1982
- [11] A.K. Agarwal, H. Karstensen, and U. Unrau, "Modal behavior of various mode mixers and mode filters for optical fiber measurements," **Nat. Bur. Stand. (U.S.) Spec. Publ. 641**, 1982
- [12] P.R. Reitz, "Measuring optical waveguide attenuation: The LPS method,"

**Bell Syst. Tech. J.**, vol. 52, no. 9, pp. 1563-1578, November 1973

- [25] G. Arfken, **Mathematical Methods for Physicists**, Academic Press, New York, third edition, 1985
- [26] S. Kawakami and J. Nishizawa, "An optical waveguide with the optimum distribution of the refraction index with reference to waveform distortion," **IEEE Trans. Microwave Theory Tech.**, vol. MTT-16, no. 10, pp.814-818, 1968
- [27] Y. Daido, E. Miyauchi, T. Iwama, and T. Otsuka, "Determination of modal power distribution in graded-index optical waveguides from near-field patterns and its application to differential mode attenuation measurement." **Appl. Opt.**, vol. 18, no. 13, pp. 2207-2213, July 1979
- [28] D. Gloge and E.A.J. Marcatili, "Impulse response of fibers with ring-shaped parabolic index distribution," **Bell Syst. Tech. J.**, vol. 52, no. 7, pp. 1161-1168, 1973
- [29] D. Gloge, "Offset and tilt loss in optical fiber splices," **Bell Syst. Tech. J.**, vol. 55, no. 7, September 1976
- [30] M. Bohn and E. Wolf, **Principles of Optics**, sixth edition, Pergamon Press, 1980
- [31] A.R. Mickelson and M. Eriksrud, "Mode-continuum approximation in optical fibers," **Opt. Lett.**, vol. 7, no. 11, pp. 572-574, November 1982
- [32] K. Petermann, "Nonlinear distortions and noise in optical communication systems due to fiber connectors," **IEEE J. Quantum Electron.**, vol. QE-16, pp. 761-770, July 1980
- [33] A.R. Mickelson and A. Weierholt, "Modal-noise limited signal-to-noise ratios in multimode optical fibers," **Appl. Opt.**, vol. 22, pp. 3084-3089, October, 1983
- [34] T. Kanada, "Evaluation of modal noise in multimode fiber-optic systems," **J. Lightwave Tech.**, vol. LT-2, pp. 11-18, February 1984
- [35] N.K. Cheung, "Reflection and modal noise associated with connectors in single-mode fibers," **SPIE Proc. on Fiber Optic Couplers, Connectors, and Splice Technology**, vol. 479, pp. 56-63, May 1984
- [36] S. Pizzola and G. De Marchis, "Analytical relations between modal power

**Opt. Spectra**, vol. 48, August 1981

- [13] A.H. Cherin and E.D. Head, "A fiber concatenation experiment using a standardized loss measurement method," **Technical Digest, Symposium on Optical Fiber Measurements Nat. Bur. Stand. (U.S.) Spec. Publ. 597**, 1980
- [14] G.T. Holmes and R.M. Hawk, "Limited phase-space attenuation measurements of low-loss optical waveguides," **Optics Letters**, vol. 6, p. 55, February 1981
- [15] R.L. Gallawa, G.E. Chamberlain, G.W. Day, D.L. Franzen, and M. Young, "Measurement of multimode optical fiber attenuation," **Nat. Bur. Stand. (U.S.) Spec. Publ. 637**, vol. 2, 1983
- [16] D.L. Franzen, G.W. Day, B.L. Danielson, G.E. Chamberlain, and E.M. Kim, "Interlaboratory measurement comparison to determine the attenuation and bandwidth of graded-index optical fibers," **Appl. Opt.**, vol. 20, p. 2412, 1981
- [17] G.T. Holmes, "Estimation of concatenated system response based on measured transfer function for low and high order modes," **Proc. 7th Europ. Conf. Opt. Comm.**, Copenhagen, paper 3.4, 1981
- [18] G. Evers, A. Kober and U. Unrau, "Measurement of mode transition matrices of quasi-step-index optical fiber components," **SPIE vol. 500 Fiber Optics**, pp. 94-99, 1984
- [19] J.M. Maisonneuve, P. Churoux, and R.L. Gallawa, "Use of mode transfer matrices in L.A.N. loss evaluation," **SPIE vol. 559 Fiber Optics**, pp. 182-185, 1985
- [20] D. Marcuse, **Theory of Dielectric Optical Waveguide**, Academic Press, New York, 1974
- [21] T. Okoshi, **Optical Fibers**, Academic Press, New York, 1982
- [22] A.W. Snyder and J.D. Love, **Optical Waveguide Theory**, Chapman and Hill, London, 1983
- [23] D. Gloge, "Weakly guiding fibers," **Appl. Opt.**, vol. 10, no. 10, pp. 2252-2258, 1971
- [24] D. Gloge and E.A.J. Marcatili, "Multimode theory of graded-core fibers,"

- distribution and near-field intensity in graded-index fibers," **Electron. Lett.**, vol. 15, pp. 721-722, 1979
- [37] O.G. Leminger and G.K. Grau, "Near-field intensity and modal power distribution in multimode graded-index optical fibers," **Electron. Lett.**, vol. 16, pp. 678-679, 1980
  - [38] G.K. Grau and O.G. Leminger, "Relations between near-field and far-field intensities, radiance, and modal distribution of multimode graded-index fibers," **Appl. Opt.**, vol. 20, pp. 457-459, 1981
  - [39] A. Walther, "Radiometry and coherence," **J. Opt. Soc. Am.**, vol. 58, pp. 1256-1259, September 1968
  - [40] A. Walther, "Radiometry and coherence," **J. Opt. Soc. Am.**, vol. 63, no. 12, pp. 1622-1623, December 1973
  - [41] E.W. Marchand and E. Wolf, "Radiometry with sources of any state of coherence," **J. Opt. Soc. Am.**, vol. 64, no. 9, pp. 1219-1226, September 1974
  - [42] E.W. Marchand and E. Wolf, "Walther's definition of generalized radiance," **J. Opt. Soc. Am.**, vol. 64, no. 9, pp. 1273-1274, September 1974
  - [43] A.R. Mickelson, E. Eriksrud, S. Aamlid, and N. Ryan, "Role of the fusion splice in the concatenation problem," **IEEE/OSA J. Lightwave Tech.**, vol. LT-2, pp. 126-138, 1984
  - [44] A.R. Mickelson, O. Klevhus, and M. Eriksrud, "Backscatter readout from serial microbending sensors," **J. Lightwave Tech.**, vol. LT-2, no. 5, pp. 700-709, 1984
  - [45] G. Evers, "Mode transmission matrices for fiber-optic connectors," **Electron. Lett.**, vol. 21, pp. 401-402, 1985
  - [46] G. Evers and U. Unrau, "Assessment of modal effects in local area networks," **Electron. Lett.**, vol 22, pp. 859-861, 1986
  - [47] I.P. Vayshenker, D.R. Hjelme, and A.R. Mickelson, "Multimode fiber systems characterization," **Symposium on Optical Fiber Measurements, Nat. Bur. Stand. (U.S.) Spec. Publ. 720**, September 1986
  - [48] G. Evers, "Calculation and measurement of mode transition matrices for differential mode attenuation and differential mode delay characterization

- of optical fibers," **Opt. Eng.**, vol. 27, pp. 179-186, 1988
- [49] S. Yang, I.P. Vayshenker, D.R. Hjelme, and A.R. Mickelson, "Transfer function analysis of measured transfer matrices," **Appl. Opt.**, vol. 28, pp. 3148-3157, 1989
- [50] A.K. Agarwal, G. Evers, and U. Umrau, "Concatenation effect calculation for fiber optic components from measured 3X3 mode transition matrices," **Proc. 4th Europ. Conf. Opt. Comm.**, Geneva, pp. 255-258, 1983
- [51] A.K. Agarwal, G. Evers, and U. Urau, "New and simple method for selective mode group excitation in graded-index optical fibers," **Electron. Lett.**, vol. 19, pp. 694-695, 1983
- [52] M. Kerker, **The Scattering of Light and Other Electromagnetic Radiation**, Academic Press, Inc., New York, 1969
- [53] R.D. Maurer, "Glass fibers for optical communications," **Proc. IEEE**, vol. 61, no. 4, pp. 451-462, 1973
- [54] D. Marcuse, "Power distribution and radiation losses in multimode dielectric slab waveguides," **Bell Syst. Tech. J.** 51, pp. 1819-1836, 1972
- [55] R. Olshanski, "Mode coupling effects in graded index optical fibers," **Appl. Opt.**, vol. 14, no. 4, pp. 935-945, 1975
- [56] D. Marcuse, "Derivation of coupled power equations," **Bell Syst. Tech. J.**, vol. 51, no. 1, pp. 229-237, 1972
- [57] P. DiVita and U. Rossi, "Theory of power coupling between multimode optical fibers," **Opt. Quant. Electron.**, vol. 10, pp. 107-117, 1978
- [58] D. Gloge, "Impulse response of clad optical multimode fibers," **Bell Syst. Tech. J.**, vol. 52, no. 6, pp. 801-815, 1973
- [59] D. Gloge, "Optical power flow in multimode fibers," **Bell Syst. Tech. J.**, vol. 51, no. 8, pp. 1767-1783, 1972
- [60] J. B. Jeunhomme, **Single-Mode Fiber Optics**, Marcel Dekker, Inc., New York, 1983
- [61] S. Yang, D.R. Hjelme, I.P. Januar, I.P. Vayshenker, and A.R. Mickelson, "Transfer function approach to the experimental determination of mode transfer matrices," **Appl. Opt.**, vol. 29, no. 21, pp. 3166-3175, July 1990

- [62] W.B. Jones, Jr., **Introduction to Optical Fiber Communication Systems**, Holt, Rinehart and Winston, Inc., New York, 1987
- [63] M.J. Yadlowsky and A.R. Mickelson, "Time-dependent radiative transfer in inhomogeneous and dispersive media: application to multimode fibers," **J. Opt. Soc. Am. A**, vol. 8, no. 6, pp. 967-975, June 1991
- [64] D.B. Keck, A.J. Morrow, D.A. Nolan, and D.A. Thompson, "Passive components in the subscriber loop," **J. Lightwave Tech.**, vol. 7, pp. 1682-1688, Nov. 1989
- [65] R.A. Wey, "Connectors: Trends," **Laser Focus/E-O**, vol. 23, pp.130-146, June 1987
- [66] R. Mack, "Fiber optic connectors," **Laser Focus/E-O**, vol. 23, pp. 148-156, June 1987
- [67] W.C. Young and D.R. Frey, "Fiber connectors," in **Optical Fiber Telecommunications II**, S.E. Miller and I.P. Kaminow, eds., Academic, New York, 1988
- [68] D.L. Bisbee, "Splicing silica fibers with an electric arc," **Appl. Opt.**, vol. 15, pp.796-798, Mar. 1976
- [69] J.T. Krause, C.R. Kyrkjian, and U.C. Pack, "Strength of fusion splices for fiber lightguides," **Electron. Lett.**, vol. 17, pp. 232-233, March 1981
- [70] M. Fujise, Y. Iwamoto, and S. Takei, "Self core-alignment arc-fusion splicer based on a single local monitoring method," **J. Lightwave Tech.**, vol. LT-4, pp. 1211-1218, Aug. 1986
- [71] S.C. Mettler and C.M. Miller, "Optical Fiber splicing," in S.E. Miller and I.P. Kaminow, eds., **Optical Fiber Telecommunications II**, Academic, New York, 1988
- [72] S. van Doorn, "Fiber optic couplers," **SPIE vol. 574 Fiber Optic Couplers, Connectors, and Splice Technology II**, 1985
- [73] P.A. Dem'yanenko, V.D. Nazarov, and A.G. Tereshchenko, "Optical couplers for fiber-optic systems," **Sov. J. Opt. Technol.**, vol. 53, no. 10, pp. 620-627, Oct. 1986
- [74] A.K. Agarwal and U. Unrau, "Tapered and spliced fiber-optic components," **SPIE vol. 500 Fiber Optics**, 1984

- [75] E.G. Rawson and M.D. Bailey, "Fused conically tapered fiber-optical power divider," *Electron. Lett.*, vol. 18, no. 11, pp. 447-448, May 1982



